Interactions between the hydrological cycle and atmospheric chemistry

Dissertation
zur Erlangung des Grades
"Doktor der Naturwissenschaften"
im Promotionsfach Geologie/Paläontologie

am Fachbereich Chemie, Pharmazie und Geowissenschaften
der Johannes Gutenberg-Universität Mainz

Meryem Tanarhte

geb. in Rabat

Mainz, 2008

Abstract

The land-atmosphere exchange of atmospheric trace gases is sensitive to meteorological conditions and climate change. It contributes in turn to the atmospheric radiative forcing through its effects on tropospheric chemistry. The interactions between the hydrological cycle and atmospheric processes are intricate and often involve different levels of feedbacks. The Earth system model EMAC is used in this thesis to assess the direct role of the land surface components of the terrestrial hydrological cycle in the emissions, deposition and transport of key trace gases that control tropospheric chemistry. It is also used to examine its indirect role in changing the tropospheric chemical composition through the feedbacks between the atmospheric and the terrestrial branches of the hydrological cycle. Selected features of the hydrological cycle in EMAC are evaluated using observations from different data sources. The interactions between precipitation and the water vapor column, from the atmospheric branch of the hydrological cycle, and evapotranspiration, from its terrestrial branch, are assessed specially for tropical regions. The impacts of changes in the land surface hydrology on surface exchanges and the oxidizing chemistry of the atmosphere are assessed through two sensitivity simulations. In the first, a new parametrization for rainfall interception in the densely vegetated areas in the tropics is implemented, and its effects are assessed. The second study involves the application of a soil moisture forcing that replaces the model calculated soil moisture. Both experiments have a large impact on the local hydrological cycle, dry deposition of soluble and insoluble gases, emissions of isoprene through changes in surface temperature and the Planetary Boundary Layer height. Additionally the soil moisture forcing causes changes in local vertical transport and large-scale circulation. The changes in trace gas exchanges affect the oxidation capacity of the atmosphere through changes in OH, O_3, NO_x concentrations.

Zusammenfassung

Der Boden-Atmosphären-Austausch von atmosphärischen Spurengasen reagiert empfindlich auf meteorologische Bedingungen und den Klimawandel. Durch seine Auswirkungen auf die Troposphärenchemie trägt er zur atmosphärischen Strahlungsstrke bei. Die Interaktionen zwischen Wasserkreislauf und atmosphärischen Prozessen sind komplex und umfassen häufig verschiedene Resonanzebenen. Im Rahmen dieser Dissertation wird das Erdsystemmodell EMAC zur Untersuchung der direkten Rolle der Bodenoberflächen-Komponenten des terrestrischen Wasserkreislaufs bei Emissionen, Ablagerungen und Transport der wichtigsten Spurengase, die die Troposphärenchemie kontrollieren, angewandt. Des Weiteren wird es eingesetzt, um deren indirekte Rolle bei der Vernderung der chemischen Zusammensetzung der Troposphäre durch die Rückkopplung zwischen atmosphärischem und terrestrischem Teil des Wasserkreislaufs zu erforschen. Ausgewählte Funktionen des Wasserkreislaufs in EMAC werden durch die Verwendung von Beobachtungen verschiedener Datenquellen evaluiert. Die Interaktionen zwischen Ausfällung und der Wasserdampfsäule des atmosphärischen Teils des Wasserkreislaufs, und der Evapotranspiration des terrestrischen Teils werden speziell fr die Tropenregion untersucht. Die Auswirkungen der Veränderungen in der Oberflächenhydrologie auf den Oberflächenaustausch und die Oxidationschemie der Atmosphäre werden mit Hilfe von zwei Sensitivitätssimulationen erforscht. Bei der ersten Untersuchung wird eine neue Parametrisierung der Niederschlagskontrolle in den dicht bewachsenen Gebieten der Tropen eingebunden und deren Auswirkungen untersucht. Die zweite Studie beinhaltet die Anwendung einer Konstante der Bodenfeuchte, die die vom Modell berechnete Bodenfeuchte ersetzt. Beide Experimente haben einen groen Einfluss auf den lokalen Wasserkreislauf, die Trockenablagerung von löslichen und unlöslichen Gasen und die Isoprenemissionen, die durch Schwankungen der Oberflächentemperatur und der PBL-Höhe verursacht werden. Zustzlich ruft die Bodenfeuchtenstrke Veränderungen im lokalen Vertikaltransport und in der groskaligen Zirkulation hervor. Die Veränderungen des Spurengasaustauschs beeinflussen die Oxidationskapazitt der Atmosphäre durch Konzentrationsschwankungen von OH, O_3und NO_x.

Contents

List of Tables

List of Figures

Chapter 1

Introduction

The Earth's climate is determined by a number of complex interconnected physical, chemical and biological processes occurring in the atmosphere, pedosphere and hydrosphere. The atmosphere controls the Earth's climate via the radiative properties of its chemical components and their abundance. These components include long lived greenhouse gases such as carbon dioxide (CO_2), methane (CH_4) and nitrous oxide (N_2O), as well as other radiatively active constituents such as ozone and different types of aerosol particles (IPCC, 2007a). The chemical composition of the atmosphere is controlled by natural and anthropogenic biophysical processes that determine the emission and the uptake of these chemical constituents from and by continental surfaces. The land-atmosphere exchange processes of atmospheric substances are tightly coupled, highly sensitive to meteorological conditions and climate change, and in turn contribute to climate forcing through the effects on tropospheric chemistry and radiative flux. The accurate knowledge of the hydrological cycle, as a pivotal component of the climate system, is crucial for the understanding of a variety of biological, physical and chemical processes that occur between the land and the atmosphere. The development of Earth system models over the last decade enabled studies of the interactions between the major components of the Earth System, i.e. the atmosphere, the hydrosphere, the biosphere, the cryosphere and the chemosphere (atmospheric, biospheric and marine) (Giorgi, 1994). The identification and the quantification of the feedback mechanisms related to these interactions is one of the major challenges in Earth system modelling.

The interactions between the hydrological cycle, and atmospheric physical and chemical processes are intricate, often involving different levels of feedbacks, and a detailed level of understanding is needed. This PhD thesis aims to identify some of the key interactions between the hydrological cycle and the atmospheric chemical composition in order to obtain a better understanding of the land-atmosphere exchange processes involving energy-, water- and reactive trace gas exchanges. The Earth system model EMAC is used to assess the direct role of the land surface components of the terrestrial hydrological cycle in emissions, deposition and

transport of key trace gases that control tropospheric chemistry, but also its indirect role in changing the tropospheric chemical composition through the feedbacks between the atmospheric and the terrestrial branches of the hydrological cycle. Here I focus on gas exchange processes whereas the role of aerosol particles in the hydrological cycle involves interactions with clouds and precipitation, being considered in separate projects.

1.1 The hydrological cycle

Water is key to our existence on this planet and it is involved in nearly all biological, geological, and chemical processes. Life on Earth depends very much on the remarkable properties of water. The water cycle, also known as the hydrologic and hydrological cycle, refers to the continuous movement of water between the Earth and the atmosphere. Water can be stored in any of the following major reservoirs: the atmosphere, the oceans, lakes, rivers, soils, glaciers, snow, and groundwater. Water moves from one reservoir to another by way of processes like evaporation, condensation, precipitation, deposition, runoff, infiltration, sublimation, transpiration, melting, and groundwater flow. The global hydrological cycle can be conceptually described as evaporation of water vapor from the ocean, transport of water vapor by atmospheric winds to land regions, condensation, and precipitation of atmospheric water back to the surface, and subsequent transport, by streams, of this water back to the oceans. The transport and transformations of water in the global water cycle are of fundamental importance for understanding terrestrial ecosystems, the land surface hydrology that supports them, and the management of water resources for humans. The water cycle is also critical for weather prediction and influences the climate system in a variety of ways.
The hydrological cycle consists of an atmospheric branch, which transports water vapor and cloud water (liquid and ice) in the atmosphere, and a terrestrial branch with a soil water regime including surface and subsurface flow and runoff in the river network. This branch includes the biologically-mediated components of the hydrological cycle related to the interplay between water resources and ecosystems. Evapotranspiration and precipitation link these two branches together at the Earth surface (e.g., pedosphere).

1.1.1 Estimation of the global hydrological cycle

Figure 1 shows the main reservoirs and fluxes of water according to Oki and Kanae (2006) based on up to date observational data. Oceans are the dominant reservoir in the global hydrological cycle with more than 92% of the world's water, whereas the atmosphere contains only about 0.001% of the available water. The remaining water is stored as groundwater, glaciers, permafrost, lakes, rivers and soil moisture. Despite its small amount, the atmosphere's horizontal and vertical distribution of water plays a key role in the global hydrological cycle and the Earth's climate. The atmosphere has direct connections to most of the other reservoirs and steers the redistribution of water between them. Evaporation over the oceans exceeds

precipitation and the difference (45,500 km^3/year) is the water vapor transport flux contributing to precipitation over land. Over land, the total terrestrial evapotranspiration only accounts for less than 60% of the precipitation reaching the ground. The difference between precipitation and evaporation over land is the amount that returns to the oceans as surface and subsurface runoff, which is the annual discharge (45,500 km^3/year) flowing mainly through rivers from continents to the sea and equals the net water vapor transport flux. Additionally, the speed of water circulation or mean residence time is crucial for climate studies. As Fig. 1 indicates, the mean residence time in the atmosphere is 9.3 days over the oceans and 9.8 days over land.

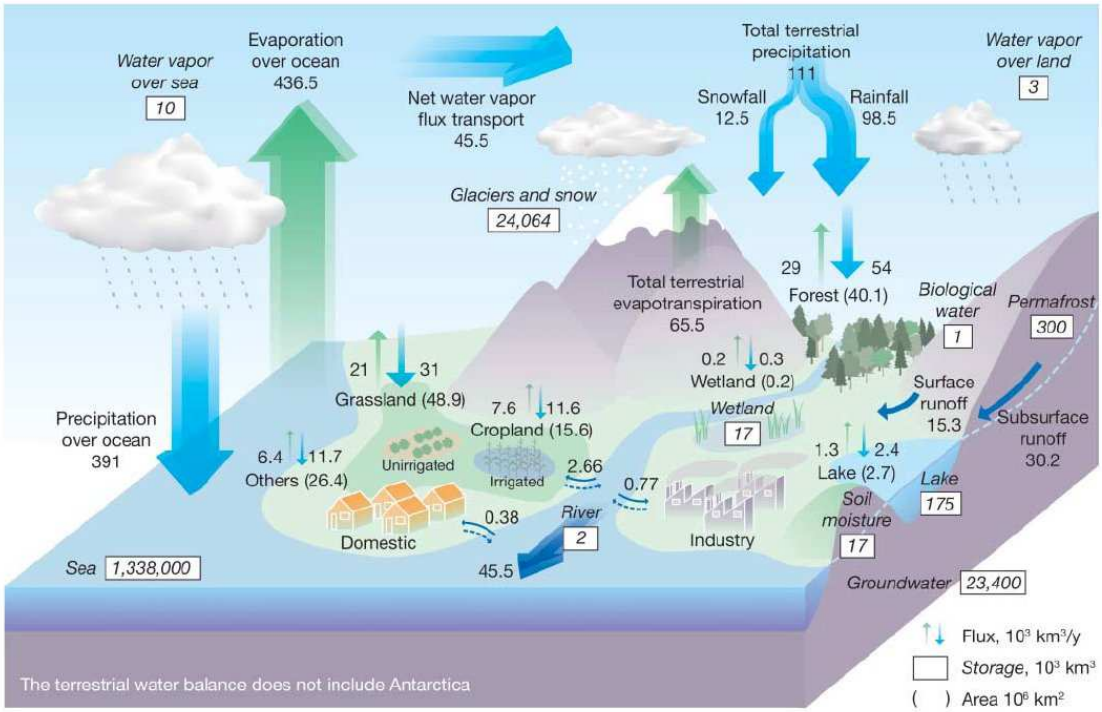

Figure 1.1: Schematic of the hydrological cycle (from Oki and Kanae, 2006)

1.1.2 The atmospheric and terrestrial branches of the hydrological cycle

The hydrological cycle has two main branches: the terrestrial and the atmospheric one. The terrestrial branch consists of inflow, outflow and storage of water in land and in oceans, while the atmospheric branch consists of transport of water mostly in its vapor phase.

The atmospheric branch of the global cycle may be expressed as:

$$\left[\frac{dw}{dt}\right] = [C] + [E] - [P] \tag{1.1}$$

The square brackets indicate spatial averaging over the control region of interest. w is the total water vapor column, also known as precipitable water, [C] is the net convergence of atmospheric water vapor flux over the control region, [P] is precipitation and [E] evapotranspiration. The change in precipitable water [dw/dt] is usually neglected for averages over a month or more (Peixoto and Oort, 1992; Marengo, 2005)). The land water balance can be represented by the equation:

$$\left[\frac{dS}{dt}\right] = [P] - [E] - [R] \tag{1.2}$$

S is the terrestrial water storage, which includes soil moisture, groundwater, snow and land ice; R is usually taken as river discharge at the basin's outlet, as subsurface flows across basin boundaries are relatively negligible. If an average of the water budget is taken over several years, the net change in terrestrial water storage is expected to be small, as seasonal and interannual variations cancel out.
Equations 1 and 2 may be combined to yield the total water balance equation:

$$\left[\frac{dw}{dt}\right] - [C] = -\left[\frac{dS}{dt}\right] - [R] \tag{1.3}$$

For averages over several years, changes in water storage on land and in the atmosphere can be neglected, and the equation relates the convergence of atmospheric moisture flux to surface and subsurface runoff out of the control region.

1.1.3 The hydrological cycle and climate change

The expected consequences of the observed enhanced greenhouse effect are increases in global average air and ocean temperatures, widespread melting of snow and ice, and rising global average sea level (IPCC, 2007a). During the 20th century the evidence for increases in both severe droughts and heavy rains in many regions of the world makes it likely that hydrologic conditions have become more intense (Trenberth, 1999). Due to the increasing global temperatures there is also a likelihood that evaporation and precipitation will increase, leading to an intensification of the hydrological cycle (Trenberth, 1999; Huntington, 2006; IPCC, 2007b). The coupling between climatic responses and global temperature is related to changes in precipitation, evaporation and water vapor.
Water vapor is the most significant greenhouse gas in the atmosphere. In most models, a warming of the troposphere due to anthropogenic greenhouse gases results in an increase in the atmospheric water vapor content which approximately doubles the warming that would

be obtained for fixed water vapor (Held and Soden, 2000; Stocker, 2001). It is then expected to further enhance the greenhouse effect. This process is known as the water vapor feedback, being a major factor in increasing the climate response to radiative forcings.

1.2 Rainfall interception

Before reaching the land surface, a part of the precipitation may be intercepted by vegetation and/or other types of surface cover. A portion of intercepted rainfall evaporates and an other portion may flow from vegetation canopies. Within vegetated systems, precipitation can be

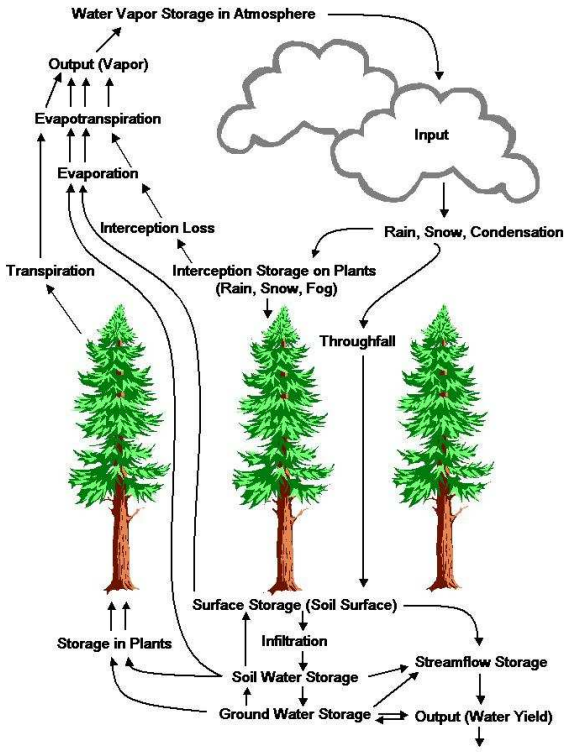

Figure 1.2: Schematic of the terrestrial hydrological cycle over vegetated regions (from Bonan (2008))

intercepted and lost to evaporation. The loss of precipitation due to evaporation of intercepted water is called interception loss. In vegetated systems, some precipitation may reach the ground by stemflow (Figure 1.2), but most often reaches the soil by a process called throughfall. Precipitation that reaches the soil surface can then infiltrate and recharge soil waters. From there it can percolate through the soil to deeper soil layers or groundwater supplies. The rate of

evaporation from soils, vegetation cover or surface waters (including oceans) can be influenced by several factors including radiation, temperature, relative humidity, and wind. Transpiration from plants takes place via water loss from the stomata, the gas exchange organs of the leaves of plants. The stomata also act as an important cooling mechanism for plants by means of latent heat absorbed and transferred from the plants through evaporation/transpiration processes. This process is also that which supplies the tensional forces necessary to help draw water into roots from the surrounding soil. Transpiration is often lumped with evaporation and is called evapotranspiration. Over vegetated areas, rainfall interception by the vegetation canopy is the first of a sequence of land surface hydrological processes, and it is a significant component of the surface water balance. The water balance of a vegetated area may be expressed by the equation:

$$[P] = [T] + [E_v] + \left[\frac{dS_v}{dt}\right] \tag{1.4}$$

where S_v is the moisture stored on the surface of vegetation, P the precipitation, T the water drainage from the leaves or throughfall and E_v the evaporation from vegetative surface. The interception is then:

$$[I] = [E] + \left[\frac{dS}{dt}\right] \tag{1.5}$$

The interception loss varies with vegetation types, canopy density, and meteorological conditions and accounts for 10-48 % of the total precipitation (Hormann et al., 1996). The capacity of vegetated surfaces to intercept and store water is of great practical importance. To hydrologists, the most important aspect of interception relates to its effect on site and catchment water balances. It is well-documented that the rate of evaporation from a wet canopy is higher than that under dry canopy conditions (Rutter et al., 1971). As such, rainfall interception and its subsequent evaporation constitute a net loss to the terrestrial ecosystem which may assume considerable values under certain conditions. In meteorology and climatology, in which the water and energy balance on regional, continental and global scales are computed, canopy interception plays an important role in land-atmosphere interactions. The representation of canopy interception impacts the partitioning of precipitation between evapotranspiration and runoff, and could cause the hydrological regime to shift from an evaporation-dominated regime to a runoff-dominated one (Pitman, 1990). It also affects the partitioning between wet surface evaporation and dry vegetation transpiration, as well as the partitioning of the net radiation between latent and sensible heat fluxes (Wang and Eltahir, 2000).

Knowledge about the interception process is formalized in models. Most current models are based on simulating the water balance during and after individual rainstorms. In the classical model of Rutter et al. (1971), the canopy was considered to be a single compartment that was filled by rain, and emptied by evaporation and drainage. This model was used for the characterization of canopy hydrological processes at a point scale. Gash (1979) and Gash et al.

(1995) derived an analytical model of interception loss based on the Rutter model. The performance of the Gash model and the more detailed Rutter model have regularly been compared in different areas for which the computed interception losses are in reasonable agreements with observations. However, neglecting the subgrid variability in convective rainfall and its interception in the tropics has been recognized to be a serious source of error in the parametrization of interception in GCMs (Shuttleworth, 1988; Dolman and Gregory, 1992; Eltahir and Bras, 1993a).

1.3 Land surface models and linkages between the water balance and the energy balance

Within a climate model, the component that simulates the effect of the Earth's surface is the land surface model (LSM). The LSM is a representation of the way the Earth's surface interacts with the atmosphere and the ways that this interaction changes as a result of both human and natural activity. Additionally, the LSM represent the impact of these changes on surface-atmosphere interactions.
There are several equations representing the role played by the surface in climate. The two key equations represent the surface energy balance and the surface water balance.

1.3.1 The surface energy balance

The net balance of the incoming and reflected shortwave radiation, and the incoming and emitted longwave radiation at the Earth's surface is called net radiation R_{net}:

$$R_{net} = (1 - \alpha_s)R_{sd} + \epsilon R_{ld} - \epsilon\sigma T_s^4 \tag{1.6}$$

where α_s is the surface albedo, R_{sd} the downwelling solar radiation, R_{ld} the downwelling longwave radiation, ϵ the surface emissivity, and σ the Stefan-Boltzmann constant. Of 100 units of energy entering the global climate system, on average 31 are exchanged as sensible and latent heat fluxes (Rosen, 1999). The land surface influences the way these 31 units of energy are partitioned between sensible H and latent heat λE fluxes (λ is the latent heat of vaporization or sublimation of water, respectively). R_{net} must be balanced by H, λE fluxes and the soil heat flux G:

$$R_{net} = H + \lambda E + G \tag{1.7}$$

Changes in the surface albedo affect R_{net}, and thus H and λE. Local albedo depends on the solar zenith angle, the surface type (vegetation cover and soil moisture, snow cover, ice cover) and cloud cover. The partitioning between (H) and (λE) is crucial for climate modeling, since lower λE produces less water vapor to the atmosphere, causing less cloudiness and precipitation,

whereas decreases in H tend to cool the planetary boundary layer and reduce convection (Betts, 1996). Other complex feedbacks exist due to changes in clouds or precipitation, which may offset the initial feedbacks.

1.3.2 The surface water balance

A basic role of the LSM is to partition available water (precipitation or snow melt) between evaporation E and runoff, which is split into a fast component (surface runoff) and a slow component (drainage). The balance between water fluxes at different interfaces (e.g., canopy surface, ground surface) is called surface water balance and has been described above in equations 1.4.
Changes in the properties of the land surface affect the surface water balance. A change in the nature of vegetation (e.g rainforest or savannah) affects interception and transpiration. A change in the distribution of vegetation modifies the balance between fluxes originating from the soils and those derived through canopy processes. Furthermore, changes in transpiration, interception loss, soil evaporation affect runoff and soil moisture, thus affecting the partitioning between latent and sensible fluxes, and in turn water vapor in the atmosphere, the cloud cover and ultimately precipitation.

1.4 Direct linkage of the terrestrial hydrological cycle to atmospheric chemistry

The soil plays a central role in the terrestrial water cycle controlling the partitioning of precipitation between interception, transpiration and runoff. Soil moisture dynamics directly controls plant conditions, soil biogeochemistry and the exchange of nutrients and contaminants between the land, composed of soil and vegetation, and the atmosphere (Eagleson, 1978; Eltahir, 1996; Porporato et al., 2003a). A large variety of gases is exchanged. The most abundant compounds are carbon dioxide (CO_2), methane (CH_4), volatile organic compounds (VOCs), reactive nitrogen compounds (NOx=NO+NO_2), and water vapor (H_2O). Other compounds of importance are nitrous oxide (N_2O), ammonia (NH_3) and various sulphur and halogen compounds. Soil moisture is of critical importance to the processes governing biogeochemical processes like dry deposition and the global soil nitrogen cycle (Scholes et al., 2003).

1.4.1 Dry deposition processes and the terrestrial hydrological cycle

Dry deposition, which is the direct removal of gases and aerosols at the Earth's surface (not via precipitation processes) is an important sink for many trace gases. It is controlled by turbulent transport and diffusion to substrates in the canopy such as the leaf or needle surface and the subsequent uptake by stomata, mesophyllic tissue and the cuticle (Erisman et al., 1994; Ganzeveld and Lelieveld, 1995). The dry deposition flux of gases from the atmosphere to a

receptor surface is governed by the concentration of the gas at a specific height and the dry deposition velocity which depends on the turbulent transport processes in the boundary layer through the aerodynamic resistance, and by the efficiency of the surface to capture and absorb gases through the surface resistance. The removal of gases like O_3 and SO_2 by vegetation is largely controlled by stomatal uptake (Baldocchi et al., 1987; Wesely and Hicks, 2000a), which can be greatly affected by changes in surface wetness due to rainfall interception, which is the water covering the leaf or needle surface and changes in the soil moisture. The source of this surface water is dewfall or rainwater intercepted by the vegetation canopy, which subsequently evaporates (interception loss). An issue under debate is the uptake of ozone O_3 by wet vegetation: some measurements indicate an inhibition while others indicate enhancement of O_3 removal (Fuentes et al., 1992; Grantz, 1995). Soil moisture also affects deposition of O_3 and other substances through its modulation of the canopy stomatal resistance (Wesely et al., 2001).

1.4.2 Biogenic emissions and the terrestrial hydrological cycle

Nitrogen-compounds emissions

Soils are an important source of atmospheric reactive nitrogen mainly due to microbial production of NO, N_2O (and N_2) in the nitrification and denitrification process, whereas NH_3 production in the soil is mainly controlled by soil pH, where NH_3 is released at high pH (although NH_4^+ is produced in all soils). The NO_x and N_2O fluxes are controlled by soil parameters such as temperature, moisture, fertility, vegetation cover and fire (Conrad, 1996). Soil emission fluxes are also linked to land use management through the application of fertilizers. The actual flux of NO_x into the atmosphere over vegetation depends on the interactions between turbulent transport, chemistry and the subsequent uptake of the reaction products within the canopy (Ganzeveld et al., 2002a). Estimates of the soil NO sources range between 9.7 TgN/yr (Potter et al., 1996) and 21 TgN/yr (Davidson and Kingerlee, 1997) whereas estimates for the emissions from the vegetation including the role of canopy deposition, are about 50% smaller (Yienger and Levy, 1995; Ganzeveld et al., 2002b).
While N_2O emissions are known to increase at higher soil water contents through larger losses from denitrification, NO emissions are expected to have a maximum at low to medium soil water content (Pilegaard, 2006). However, soil and vegetation type play an important role in regional emissions. In the last decades, models used to predict soil NO and N_2O emissions have evolved from simple empirical schemes to process-oriented models that incorporate more mechanistic process descriptions. The Yienger and Levy (1995) empirical model of soil NO emissions, a statistical model derived from observations, accounts for soil temperature and precipitation effects and the application of fertilizers. It also accounts for the effect of pulsing. Other more comprehensive models are more process-oriented and describe the nitrogen cycle in more detail. As an example of process-oriented model is the DAYCENT plant-soil ecosystem model (Parton et al., 2001).

Isoprene emissions

Among the biogenic volatile organic compounds (BVOCs), isoprene is the most strongly emitted compound, with global emissions of about 600 TgC/year (Guenther et al., 1995, 2006). The driving factors controlling isoprene emissions include temperature and solar radiation. Additionally, the soil moisture stress and the age of the leaves have been identified to have strong impacts on the emissions, although their quantitative influence remains uncertain. Using MEGAN (Model of Emissions of Gases and Aerosols from Nature), the impact of soil moisture stress has been found to reduce annual global isoprene emissions by 7% but can reduce regional emissions to zero for days to months (Guenther et al., 2006) . In a recent publication, Müller et al. (2008) calculate an annual global isoprene emission of 20% less than the standard MEGAN estimate mainly due to the impact of the soil moisture stress factor. The greatest impact is found in arid regions. However, reductions can also be found in tropical regions in the dry season. Soil moisture also influences emissions through the stomatal resistance and surface temperature though the coupling between the water balance and the energy balance as indicated above.

1.5 Indirect linkage of the terrestrial hydrological cycle to atmospheric chemistry

1.5.1 The hydrological cycle and boundary layer processes

The land-atmosphere feedbacks play a key role in determining the nature of the Planetary Boundary Layer (PBL). For example, the soil moisture-evaporation-precipitation feedback illustrates the mutual interaction of the soil and the PBL states. Evaporation changes the thermodynamics of the vertical water column, favoring future precipitation. Higher evaporation (associated with wetter soils) reduces both the albedo and the Bowen ratio (Bastiaanssen, 1995; Brutsaert, 1982). This results in higher net radiation over the surface, and higher total heat energy input to the atmosphere, which leads to a larger moist static energy of the boundary layer. Moist static energy plays an important role in the dynamics of local convective storms, and it strengthens the large-scale monsoon circulation (Schär et al., 1999; Eltahir, 1998).

1.5.2 The hydrological cycle and the oxidizing capacity of the atmosphere

Vast amounts of reactive chemical compounds are emitted into the atmosphere, the largest share being carbon monoxide, methane and other hydrocarbons from biogenic sources. These compounds are being constantly removed from the atmosphere through oxidation into water-soluble compounds including CO_2, and the subsequent uptake by liquid water, snow or ice and removal by precipitation and surface dry deposition. The oxidizing power or cleansing power of the atmosphere is determined by the oxidizing species O_3, radical species (the hydroxyl radical (OH) and hydroperoxyl radical (HO_2) and NO_x. These species react with the reduced

organic gases emitted by ecosystems. The most important initial step of the chemical removal mechanisms is the reaction with OH radical, the atmospheric "detergent" (Crutzen, 1995). The most important OH source is the photodissociation of ozone to produce the excited state oxygen atom, $O(^1D)$, which reacts with water vapor to produce two OH molecules (Levy, 1971). The first-order dependence of OH formation on the humidity of the atmosphere provides the basis for a connection between chemistry and hydrology (Monson and Holland, 2001). Seinfeld (1999) determined that at 50% relative humidity and an air temperature of 20°C, 9.1% of the $O(^1D)$ that is formed at surface pressure conditions reacts with H_2O to form OH. A reduction in surface evapotranspiration, or the entrainment of dry air from above the planetary boundary layer, e. g. resulting in a 50% reduction in humidity, would cause a 50% reduction in the rate of primary OH formation (Monson and Holland, 2001).
Because of the high-levels of UV-radiation and water vapor in the tropics, OH concentrations are highest in the tropics. In these regions, the hydrological cycle strongly affects the dynamics of physical transport, especially through the regulation of soil moisture. Land-use and land-cover changes and the resulting perturbation of the soil moisture dynamics are thus expected to perturb the oxidant cycle over the tropical regions (Ganzeveld and Lelieveld, 2004).

1.5.3 Thesis structure

The overall objective of this PhD thesis is to improve the understanding of the role of the hydrological cycle in the land-atmosphere exchanges and the atmospheric chemistry. The thesis is divided into two parts. The first is an evaluation of the main features of the hydrological cycle and an attempt to understand the interactions between the atmospheric branch and the terrestrial branch of the hydrological cycle through the comparisons of the model results with satellite data, a radiosondes dataset and a multimodel land surface variables dataset. Emphasis will be put on seasonal precipitation, evapotranspiration, specific humidity and relative humidity. The second part consists of sensitivity simulations in which the impact of changes in the land surface model on surface exchanges and the oxidative chemistry of the atmosphere is assessed. The thesis is structured as follows: the second chapter is a description of the Atmospheric Chemistry General Circulation Model EMAC, the model used in our study. The third chapter is an evaluation of the hydrological cycle of two resolutions of the model through comparisons with observations. A first sensitivity study using a new parametrization for rainfall interception is addressed in Chapter 4. In Chapter 5, a second sensitivity simulation is conducted using a soil moisture forcing. The effects on the meteorology and atmospheric chemistry are analyzed, while final considerations and conclusions are presented in Chapter 6.

Chapter 2

Model description

2.1 ECHAM5

The fifth-generation atmospheric general circulation model (ECHAM5) (Roeckner et al., 2003, 2006) developed at the Max Planck Institute for Meteorology (MPIM) is the most recent version in a series of ECHAM models that have evolved originally from the spectral weather prediction model of the European Centre for Medium Range Weather Forecasts (ECMWF) and later transformed into a climate model. ECHAM5 simulates the dynamics and thermodynamics of the atmosphere, solving the basic equations of atmospheric dynamics. The solutions of the basic equations are obtained with the spectral transform method using grid and spectral representations. The model resolution depends on the (triangular) truncation of the waves in spectral space. In the vertical, a flexible coordinate is used, enabling the model to use either the usual terrain following sigma coordinates, or hybrid coordinates for which upper-level model surfaces flatten over steep terrain, becoming surfaces of constant pressure in the stratosphere. In the standard configuration the vertical dimension reaches up to 10 hPa (middle of the uppermost layer), with 19 or 31 levels, whereas in the middle atmosphere (MA) configuration, the model describes the atmosphere up to 0.01 hPa (middle of the uppermost layer), with 39 or 90 vertical layers. The horizontal and vertical resolution also defines the maximum time step applicable. The standard resolutions for tropospheric studies are summarized in Table 2.1. A flux form semi-Lagrangian scheme is employed for passive tracer transport (Lin and Rood, 1996). Prognostic variables calculated with the set of primitive equations for a moist atmosphere are temperature, divergence and vorticity, the logarithm of the surface pressure, and specific humidity, cloud water and cloud ice. Emphasis will be put on describing surface processes because they are of special importance for this work.

Table 2.1: The standard resolutions of the ECHAM5 model for tropospheric studies

Resolution	lon x lat	approx. box width (deg)	Time step (s)
T21L19	64 x 32	5.6 x 5.6	2400
T31L19	96 x 48	4.2 x 4.2	1800
T42L31	128 x 64	2.8 x 2.8	1200
T63L31	192 x 96	2.1 x 2.1	720
T85L31	256 x 128	1.4 x 1.4	480
T106L31	320 x 160	1.1 x 1.1	360
T159L31	480 x 240	0.7 x 0.7	180

2.1.1 Surface fluxes

Surface turbulent eddy fluxes of momentum, dry static energy (sensible heat), cloud water, and moisture are simulated as stability-dependent bulk formulae, following Monin-Obukhov similarity theory. The required near-surface values of wind, temperature, cloud water, and humidity are taken to be those at the lowest atmospheric level. Surface fluxes of radiation, sensible heat, moisture and momentum are calculated for three surface types in each grid-cell, i.e. land, open water (sea, lake) and ice. Over land each grid square is divided into four fractions: 1/ snow, 2/ skin reservoir which is soil or vegetation covered by water, 3/ bare soil and 4/ dry vegetation. The surface moisture flux depends on the surface specific humidity; over ocean, snow, ice, and wet vegetation fractions of each grid box, this is taken as the saturated humidity at the surface temperature and pressure (i.e., potential evaporation is assumed).

The moisture flux over sea J_q:

$$J_q = \rho \cdot C_h \cdot |v_h| \cdot (q - q_s(T_s, p_s)) \tag{2.1}$$

where ρ is the air density, C_h is the transfer coefficient for heat at the lowest model level, $|v_h|$ the absolute value of the horizontal velocity, at the lowest model level, q the specific humidity at the lowest model level. q_s is the saturation specific humidity at surface temperature T_s and pressure p_s.
Over land, each grid square is divided into 4 fractions:

- fraction C_{sn} covered with snow
- fraction $(1 - C_{sn}) \cdot C_l$ covered with water in skin reservoir (wet skin fraction)
- fraction $(1 - C_{sn}) \cdot (1 - C_l) \cdot C_v$ covered with vegetation

- fraction $(1 - C_{sn}) \cdot (1 - C_l) \cdot (1 - C_v)$ covered with bare soil

The wet skin fraction C_l is derived from the skin reservoir water content:

$$W_{lmx} = W_{lmax} \cdot (1 + LAI) \tag{2.2}$$

W_l is the prognostic variable for the skin reservoir content, W_{lmx} is the maximum skin reservoir content, LAI is the leaf area index, and W_{lmax} is the maximum amount of water that can be held on one layer of leaf or bare ground. It is taken to be 2. 10^{-4} m.

The grid fraction C_v occupied by vegetation is equal to the climatological field "vegetation ratio" values from the land surface dataset (Hagemann, 2002).

Evaporation from snow and the skin reservoir J_{qs} takes place at the potential rate:

$$J_{qs} = \rho \cdot C_h \cdot |v_h| \cdot (q - q_s(T_s, p_s)) \tag{2.3}$$

For the evaporation from bare soil (no water in skin reservoir) J_{qw} it is assumed that the relative humidity h at the surface is related to the water content W_s of the soil:

$$J_{qw} = \rho \cdot C_h \cdot |v_h| \cdot (q - hq_s(T_s, p_s)) \tag{2.4}$$

$$h = max\left(0.5 \cdot (1 - cos\frac{\pi \cdot W_s}{W_{Smax}}), min(1, \frac{q}{q_s(T_s, p_s)})\right) \tag{2.5}$$

W_s represents the total amount of water available in the root zone (the so-called soil moisture) and W_{Smax} is the field capacity derived from the land surface dataset (see below).
The evaporation from dry (no water in skin reservoir) vegetated areas J_{qdv} is proportional to the evaporation efficiency E:

$$J_{qdv} = \rho \cdot C_h \cdot |v_h| \cdot (q - Eq_s(T_s, p_s)) \tag{2.6}$$

Based on (Sellers et al., 1986), E is expressed as:

$$E = \left(1 + \frac{C_h \cdot |v_h| \cdot R_{co}(PAR)}{F(W_s)}\right)^{-1} \tag{2.7}$$

where $R_{co}/F(W_s)$ is the stomatal resistance of the canopy, with a minimum value R_{co} dependent on the Photosynthetically Active Radiation (PAR), and an empirical function of the available water in the root zone $F(W_s)$.

$$\frac{1}{R_{co}} = \frac{1}{k \cdot c}\left(\frac{1}{d \cdot PAR} \cdot ln(\frac{d \cdot e^{k \cdot LAI} + 1}{d + 1}) - ln(\frac{d + e^{-k \cdot LAI}}{d + 1})\right) \tag{2.8}$$

where $d = \frac{(a+b) \cdot c}{c \cdot PAR}$, $k = 0.9$, $a = 5000\ Jm^{-3}$, $b = 10\ Wm^{-2}$, $c = 100\ sm^{-1}$, and PAR is 55 % of the net shortwave radiation at the surface. In the case of dew deposition ($q > q_s$): $E = h = 1$

The water stress factor $F(W_s)$ is

$$F(W_s) = \begin{cases} 1 & if\ W_s \geq W_{cr} \\ \frac{W_s - W_{pwp}}{W_{cr} - W_{pwp}} & if\ W_{pwp} < W_s < W_{cr} \\ 0 & if\ W_s \leq W_{pwp} \end{cases} \tag{2.9}$$

W_{cr} is a critical value taken as 75 % of the field capacity W_{Smax}, while W_{pwp} is the permanent wilting point taken as 35 % of W_{Smax}.

The total evaporation in a grid square combines the four fractions.

2.1.2 Soil hydrology

The parametrization of soil hydrology in ECHAM5 comprises budget equations for four water reservoirs (Roeckner et al., 2003):

- Snow S_{nc} (water equivalent) intercepted by the canopy

- Snow S_n (water equivalent) at the surface
- Rain water W_l intercepted by the canopy
- Soil water W_s

For the two first reservoirs we refer to Roeckner et al. (2003), and here we focus on the two latter reservoirs that are of most interest for this work.

Rainfall interception by the canopy

A fraction $c_v P$ (where $c_v = 0.25$ is an interception parameter) of the incoming rain P is intercepted in the canopy with an upper limit defined by the capacity of the interception reservoir,W_{lmx}

$$\rho_w \frac{\partial W_l}{\partial t} = c_v P + J_{qs} + \rho_w S_{nc} \tag{2.10}$$

where $J_{qs} < 0$ is the evaporation (interception loss) and $J_{qs} > 0$ the dew deposition. Melting of S_{nc} contributes to W_l unless the capacity of the interception reservoir is exceeded. In that case, the excess water would contribute to the soil water budget through the term M_{snc}.

Soil water

Changes in soil water W_s due to rainfall, evaporation, snow melt, surface runoff and drainage are calculated for a single "bucket" with geographically varying maximum field capacity taken from the land surface dataset.

$$\rho_w \frac{\partial W_s}{\partial t} = (1 - c_v)P + E_t + M_{sn} + M_{snc} - R_s - D \tag{2.11}$$

where $E_t < 0$ includes the effects of bare-soil evaporation and evapotranspiration, and $E_t > 0$ the dew deposition. M_{sn} is the snow melt at the surface, M_{snc} the excess snow melt in the canopy, R_s the surface runoff and D the drainage. Runoff and drainage are calculated from a scheme which takes into account the heterogeneous distribution of field capacities within a grid-cell (Dümenil and Todini, 1992). The storage capacity of the soil is not represented by a unique value, as in the traditional bucket scheme, but by a set of values with a probability density function.

Surface temperature

The surface energy balance for the interface between the land surface and the atmosphere can then be written as

$$C_L \frac{\partial T_s}{\partial t} = R_{net} + \lambda E + H + G \tag{2.12}$$

where C_L is the heat capacity of the layer $[Jm^2K^{-1}]$, H is the sensible heat flux, λE the latent heat flux (λ is the latent heat of vaporization or sublimation of water), G is the ground heat flux and R_{net} the net radiation.
The land surface temperature is obtained from the surface energy balance equation using an implicit coupling scheme that allows the synchronous calculation of the prognostic variables and surface fluxes. The surface temperature is used as a boundary condition to determine the vertical profile within the five-layer soil model assuming vanishing heat flux at the bottom of the lowest layer.
The temperature profile within the soil is calculated from the thermal diffusion equation. The upper 10 m of the soil are divided into 5 unevenly spaced layers with thicknesses, from top to bottom, of 0.065, 0.254, 0.913, 2.902, and 5.700 m.

2.2 EMAC

The version 5.3.01 of ECHAM5 is coupled to the Modular Earth Submodel System MESSy (Jöckel et al., 2005) developed at the Max Planck Institute for chemistry (MPIC). MESSy (see the website http://www.messy-interface.org) is designed as an interface to couple several processes called submodels to a general circulation model (GCM). The resulting EMAC (ECHAM/MESSy Atmospheric Chemistry) model is a fully coupled atmospheric chemistry-GCM that provides possibilities to study chemistry-climate interactions. EMAC has been extensively evaluated in Jöckel et al. (2006). The version 1.2 has been used in the evaluation simulation (Chap. 3) and version 1.4 in the simulations performed for Chap. 4 and 5.
In Table 2.2 only the selected submodels for our simulations are presented.

Table 2.2: List of selected MESSy submodels currently available in MESSy-version 1.4 and used for our simulations.

Submodel	Function
CLOUD	ECHAM5 Cloud routines modularized
CONVECT	CONVECTion processes
CVTRANS	ConVective tracer TRANSport
DRYDEP	DRY DEPosition of gases and aerosols
JVAL	calculates J-VALues
MECCA	calculation of gas phase chemistry
OFFLEM	OFFLine EMissions
ONLEM	ONLine EMissions (gas and aerosol)
RAD4ALL	Passive TRACer (diagnostics)
SCAV	SCAVenging and wet deposition of gases and aerosols
TROPOP	diagnostic of TROPOPause and boundary layer height

A detailed description of the submodels used in this study is given in the following sections.

2.2.1 Cloud and convection processes

Some processes included in ECHAM5 have been substituted and extended by MESSy submodels in ECHAM5/MESSy.

CLOUD integrates a number of routines available in ECHAM5 recoded, according to the MESSy standards. This submodel provides an interface for selectable cloud microphysical schemes. It calculates the cloud droplet number concentrations, the large-scale cloud cover, condensation, and precipitation formation and evaporation. Water vapor, cloud water and cloud ice are prognostic variables in the ECHAM5 model and their changes due to the processes mentioned above result in a tendency that is applied in the ECHAM5 integration scheme. At present only the original cloud and cloud cover calculating parameterizations from the ECHAM5 model are implemented. These are described in detail by Roeckner et al. (2003), based on work by Lohmann and Roeckner (1996). The prognostic cloud cover scheme is derived from Tompkins (2002). The scheme provides the liquid/ice water content and the precipitation formation and evaporation rates, precipitation flux from each model level and cloud cover.

CONVECT deals with the effects of moist deep convection, and enables the implementation of several convection parameterizations schemes. It contains the original ECHAM5 convection routines based on Tiedtke scheme (Tiedtke, 1989; Nordeng, 1994) used as the default convection scheme. Other convection parameterizations are also available. These schemes are all fully coupled to the other physical processes of the model, using input parameters from the GCM, and returning their output to the GCM (Tost et al., 2006b).

CVTRANS is an online transport submodel for vertical transport in convective columns, using the bulk approach, based on Lawrence and Rasch (2005), and described further in Tost (2006).

2.2.2 Emissions

Emissions in MESSy are calculated by the submodels ONLEM and OFFLEM. The latter deals with prescribed emissions fluxes or mixing ratios, whereas the first calculates interactive emissions depending on meteorological or surface parameters calculated by others submodels. In OFFLEM an emission flux can be applied directly by adding a tendency to the tracers mixing ratio in the respective grid box, or by converting it into a lower boundary condition which is processed by the calculations for boundary layer meteorology and vertical diffusion. Offline emissions are used for CO, HCHO, HCOOH, CH_3OH, higher hydrocarbons (i.e., C_2H_4, C_2H_6, C_3H_6, C_3H_8, C_4H_{10}, CH_3CHO, CH_3COOH, CH_3COCH_3, $CH_3COC_2H_5$), SO_2, NH_3 and anthropogenic NO_x. Most of the data is taken from the EDGAR-database (Emission Database for Global Atmospheric Research, http://arch.rivm.nl/env/int/coredata/edgar). NH_3 emission data are taken from the GEIA inventory emission according to (Bouwman et al., 1995). Additionally, NO_x emissions from aircraft are based on Schmitt and Brunner (1997).
The online emissions are calculated based on computed parameters. Soil biogenic NO emissions are based on the Yienger and Levy algorithm (1995). They use an empirical model that calculates emissions as a function of ecosystem-specific emission factors based on 72 ecosystems defined by Olson (Olson, 1992) in combination with a Normalized Difference Vegetation Index (NDVI) satellite dataset, soil moisture and temperature, and the cultivation intensity. It also accounts for the effect of "pulsing", which represents enhanced emissions of NO_x after a rainfall event, preceded by a period of drought. The temperature effect is calculated using the modeled soil temperature at the top layer. The ECHAM5 calculated soil moisture is used to distinguish between dry and wet soils. Moreover, the soil emission flux is a function of a cultivation index, representing the intensity of the agricultural activity, and the application of fertilizers. The effect of pulsing is considered using a 2-week history record of the ECHAM5 calculated precipitation to determine the dry period.
Emissions of biogenic NMVOC (non-methane volatile organic compounds) are calculated according to Guenther et al. (1995) as a function of ecosystem specific emission factors, the foliar density and leaf area index, surface radiation and temperature.

2.2.3 The chemical mechanism and photolysis

The gas phase chemistry in MESSy is calculated with MECCA (Module Efficiently Calculating the Chemistry of the Atmosphere) (Sander et al., 2005). Its role is the numerical solution of the set of differential equations determined by the selected species and reactions using the Kinetic PreProcessor (KPP) (Damian et al., 2002; Sandu and Sander, 2006). The species and reactions to be considered have to be selected prior to the simulation. The user can choose from a wide

range of chemical compounds and their reactions. The MECCA chemical mechanism includes stratospheric chemistry following Steil et al. (1998) and tropospheric chemistry including non-methane hydrocarbon (NMHC) species following von Kuhlmann et al. (2003). Additionally, sulphur and halogen chemistry from von Glasow et al. (2002) is included. The calculation of the chemical reactions in the model requires the knowledge of the rate coefficients of the reactions. These reaction rates are dependent on meteorological and chemical parameters such as temperature, pressure and the tracer concentration. In case of photolysis reactions, the required photolysis reaction rates are imported from JVAL.
In our simulations we use a minimum chemistry mechanism of 42 reactions and 30 species described in detail in Appendix A. Additional artificial tracers are added.
As mentioned above the photolysis rates for the chemical integration scheme are provided by the submodel JVAL. The physical core of JVAL is based on the 8 wavelength band parameterization of Landgraf and Crutzen (1998).

2.2.4 Scavenging and wet deposition

Scavenging by cloud and rain droplets as well as wet deposition are important loss processes for trace gases. The SCAV submodel (Tost et al., 2006a) simulates large scale and convective scavenging in rain, snow and ice, accounting for nucleation and impaction scavenging. It is based on the exchange between the gas phase and the droplets as well as the chemistry within the droplets which are calculated with KPP.

2.2.5 Radiation

The RAD4ALL submodel contains the original radiative transfer routines of ECHAM5 recoded according to the MESSy standards. Additionally, it allows for the interactive coupling with trace gases. For aerosols, the original ECHAM5 aerosol climatology has been applied (Tanre et al., 1984).

2.2.6 Dry deposition

The submodel DRYDEP calculates the loss of trace gases and aerosol particles from the atmosphere to the earth's surface in absence of precipitation. The process of the trace gas and aerosol removal is implemented in EMAC according to Ganzeveld and Lelieveld (1995). This mechanism is implemented only for a few gases, O_3, NO, NO_2, HNO_3, SO_2. The dry deposition velocities of other trace gases, that are expected to have an important sink due to the dry deposition process are interpolated according to their solubility and reactivity between the dry deposition velocities of SO_2 and O_3. The uptake resistances of the individual gases are interpolated based on their Henrys law coefficient and an estimated reactivity coefficient, where SO_2 is taken as reference for soluble non-reactive trace gases and O_3 for non-soluble reactive trace gases.

Dry deposition of trace gases is based on the Big-Leaf approach (Ganzeveld et al., 1998) where the dry deposition velocity for a trace gas X (v_d) is calculated using a multi-resistance approach:

$$v_d(X) = \frac{1}{R_a + R_b(X) + R_{surf}(X)} \tag{2.13}$$

where R_a is the aerodynamic resistance, which is a function of the turbulence in the surface layer, R_b is the quasi-laminar boundary-layer resistance, partially controlled by molecular diffusion, and R_{surf} is the combined resistance of all transfer pathways which play a role in the uptake of trace gases by the surface. R_b is neglected because it is much smaller than R_a and R_{surf}. R_s depend on the surface type. Over the ocean, the model distinguishes between sea ice and open ocean. Over land, the grid box in ECHAM5 is divided into 4 fractions (see above): snow/ice, wet skin fraction, bare soil and dry vegetation. R_{surf} is defined by

$$R_{surf} = R_{surfacetype} \tag{2.14}$$

and over dry vegetation

$$R_{surf} = \frac{1}{\frac{LAI}{R_{leaf}} + \frac{1}{R_{soil}}} \tag{2.15}$$

where LAI is the leaf area index, R_{leaf} is the leaf/needle resistance which is the resultant resistance of the mesophyll, stomatal resistance and the cuticular resistance. The stomatal resistance is provided by the base model ECHAM5 (see above).
The deposition flux F_c is expressed by multiplying the dry deposition velocity with the surface layer concentration of a gas X:

$$F_c(X) = c_z(X) v_d(X) \tag{2.16}$$

where F_c is the deposition flux of the trace gas X (molec m^{-2} s^{-1}), c_z is the concentration of X (molec m^{-3}) at a reference height z and v_d is the deposition velocity.

Chapter 3

Evaluation of the hydrological cycle of EMAC

3.1 Introduction

An accurate knowledge of the hydrological cycle, as a pivotal component of the climate system, is essential for the understanding of a variety of biological, physical and chemical processes that occur between the land and the atmosphere. The hydrological cycle affects the energy cycle in a variety of ways. In the form of vapor, water acts as the strongest greenhouse gas (Raval and Ramanathan, 1989). Clouds influence the thermal structure of the atmosphere and the partitioning of energy between land and atmosphere. Soil moisture influences the surface temperature and the surface energy budget.

Some of the most important climate change manifestations are related to the global water cycle. This includes climate feedbacks of water vapor, clouds, sea-ice and snow-albedo, or an intensification of the water cycle (Huntington, 2006) characterized by an increase in precipitation, evaporation and river discharge.

There are few attempts to characterize and quantify the global water cycle (Chahine, 1992; Oki, 1999; Oki and Kanae, 2006; Trenberth et al., 2007). These studies provide estimates of the various components of the global water cycle and their variability. Other studies focus on regional or basin-scale analysis of the water budget. There have been numerous studies examining the representation of various components of the hydrological cycle in general circulation models (GCMs). This includes studies of precipitation, atmospheric water vapor and its transport, clouds, snow, sea-ice and soil moisture. The state-of-art GCMs have been extensively evaluated against observations in the framework of the Atmospheric Model Intercomparison Project (AMIP II) including precipitation and evaporation (Lau et al., 1995), water vapor (Gaffen et al., 1997), cloudiness (Weare and Mokhov, 1995) and soil moisture (Robock et al., 1998). Recent versions of some of these models have been used in the Fourth Assessment Report

(AR4) by the Intergovernmental Panel on Climate Change (IPCC), and also evaluated against observations with respect to the water cycle (Waliser et al., 2007; Li et al., 2007). In other studies hydrologic products from model reanalyses have been assessed (Trenberth and Guillemot, 1998). PILPS (Project for the Intercomparison of Land-surface Parameterization Schemes), as a project of the Global Land Atmosphere System Study (GLASS), was designed to improve the parameterization of the continental surface, especially hydrological and energy exchanges with the atmosphere. Since the early 1990s and until now, PILPS (e.g. Henderson-Sellers et al. (1993)) has evaluated the state-of-art parameterization schemes employed in coupled climate, atmospheric and Earth system models. In its phase 2b an intensive investigation of soil moisture simulation in land-surface schemes (Shao and Henderson-Sellers, 1996) was conducted and compared to observations.

Because of the importance of water vapor in the climate system and in climate models, a number of assessments of simulations of humidity by general circulation models (GCMs) have been performed. Gaffen and Barnett (1992) compared interannual variations of specific humidity from radiosondes observations with simulations from ECHAM3, Chen et al. (1996) compared ECHAM4 with satellite-derived estimates of precipitable water and upper-tropospheric relative humidity. Soden and Bretherton (1994) compared the ECMWF and NCAR GCMs precipitable water and upper-tropospheric humidity fields with operational analyses and with satellite observations. More recently, Iacono et al. (2003) used High-Resolution Infrared Radiation Sounder (HIRS) radiances to evaluate the upper tropospheric water vapor in the NCAR Community Climate Model (CCM3). Allan et al. (2003) compared the clear-sky radiances, sensitive to upper-tropospheric relative humidity, of Hadley Centre climate model (HadAM3) with the same satellite data. A comparison of total precipitable water between NCEP (National Center for Enviornmental Prediction), ERA40 (the ECMWF Reanalysis) Reanalyses and NVAP (The NASA Water Vapor Project) has been performed by Sudradjat et al. (2005). Pierce et al. (2006) compared three-dimensional distributions of specific humidity in state-of-the-art fully coupled global ocean-atmosphere GCMs (including ECHAM5) to measurements from the AIRS (Atmospheric Infrared Sounder) satellite system.

Hagemann et al. (2006) has evaluated ECHAM5 simulations against observational data of precipitation and river runoff in a number of catchments representing the major river systems around the globe. Emphasis has been put on the influence of the vertical and horizontal resolution on the simulated parameters. Using the same versions of this model, Arpe et al. (2005) investigated the ability of ECHAM5 to simulate precipitation and runoff in several river catchments in the Arctic and Northern Europe.

The focus of this study is the comparison between modeled and observed climatologies of precipitation, evapotranspiration and the total water vapor column. New observation data sets are used to show the ability of EMAC in simulating the primary features of the hydrological cycle. Emphasis will be placed on the validation of the water vapor climatology and related variables (relative humidity and temperature) from the atmospheric branch of the hydrological cycle in relationship to its terrestrial branch through the evapotranspiration.

3.2 Model setup

Two runs at the two resolutions T42L31 and T63L31 have been performed in this study using the submodels CLOUD and CONVECT (using the default Tiedtke scheme). These two resolutions are the two resolutions that are likely to be used in EMAC for tropospheric studies. Twelve years of AMIP-style runs starting from the year 1991 have been performed with the first 2 years considered as spinup time. The period considered here is 1993-2002 which includes the availability period of the GOME satellite instrument (1995-2002, see the next section).

3.3 Observational data

3.3.1 Precipitation

The processes of the hydrological cycle operate on a wide range of time and space scales, and are very difficult to quantify observationally. The most reliable observations of the hydrological cycle are limited to relatively long time and large spatial scale. There are a large number of observational datasets related to the Earth's hydrological cycle. An intercomparison study of global precipitation products (Adler et al., 2001) has shown that the merged data products (such as GPCP and CMAP) provide the overall "best" results. The Global Precipitation Climatology Project (GPCP) version-2 Monthly Precipitation Analysis (Adler et al., 2003) is a globally complete precipitation analysis that is produced by merging low-orbit microwave and infrared satellite retrievals with surface gauge observations. The data are projected on a 2.5 X 2.5 grid and span the years 1979 to the present. Another global merged data set, the Climate Prediction Center (CPC) Merged Analysis of Precipitation (CMAP) also covers the period from 1979 to the present (Xie and Arkin, 1997). While there is good large-scale agreement between the two data sets, considerable regional differences exist, such as an artificial trend in the tropics in the CMAP data set, a result of atoll data sampling deficiencies and the way they are used in the merging procedure (Yin et al., 2005).

3.3.2 Water vapor column

Global water vapor concentrations are estimated from satellite based measurements in the infrared as for example High-resolution Infrared Radiation Sounder (HIRS) as part of the TIROS-N Operational Vertical Sounder (TOVS) instrument suite; whereas the microwave sensors, for example with the Special Sensor Microwave Imager (SSM/I),are predominantly sensitive to the lower troposphere and over oceans only, infrared radiometers peak higher in the troposphere especially over land (Engelen and Stephens, 1999). In contrast to visible and infrared sensors, microwave instruments are insensitive to clouds. Instruments measuring in the visible or near-infrared part of the spectrum provide the advantage of being sensitive to the lower part of the troposphere containing the bulk of water vapor for both land and ocean surfaces. In order

to combine all advantages of the different measurement techniques, NVAP (NASA Pathfinder water vapor project) has been compiled taking advantage of the radiosonde measurements combined with TOVS and SSM/I (Randel et al., 1996). In this study we choose to take advantage of global information on water vapor derived from a single instrument the Global Ozone Monitoring Experiment (GOME). The GOME spectrometer on the European Space Agency's satellite measures backscattered solar radiation continuously between 240 and 790 nm with a spectral resolution of an average 0.22 nm in the visible and infrared regions. The instrument measures on a spatial resolution of 40 by 310 km. Various algorithms have been developed to derive total water vapor column (TWVC) from GOME instrument (e.g., Noel et al., 1999; Wagner et al., 2006; Lang et al., 2003). GOME provides global coverage of TWVC for both land and ocean surfaces, however only in cloud-free situations. TWVC from GOME has been applied for model evaluation and climate change studies in a number of publications (Lang and Lawrence, 2005a,b). A climatology of GOME has been evaluated against radiosondes and other satellite products and made available for climate studies (Lang et al., 2007).

For additional model comparison we employ vertical distributions of specific humidity, relative humidity and temperature from the WMO operational radiosonde network comprised in MCOS (Max Planck Institute for Chemistry Operational Sonde data set) (Lang and Lawrence, 2005b; Lang et al., 2007), which comprises more than 1000 stations distributed over the globe, with very good spatial coverage in the industrialized regions and little coverage in developing countries, remote regions and the oceans. Due to systematic biases of radiosonde sensors in the upper-troposphere and stratosphere, MCOS delivers meaningful results only up to 8km altitude (John and Buehler, 2005). Extremes or unphysical outliers in the original sonde data, together with the problematic upper part of the profiles have been omitted in the integration of the TWVC, justified because its contribution to the total column is negligible (Lang and Lawrence, 2005b; Lang et al., 2007).

3.3.3 Evapotranspiration and soil moisture

The Global Energy and Water Cycle Experiment (GEWEX) Global Soil Wetness Project Phase 2 (GSWP2; Dirmeyer et al. (2006)) provides a complete multimodel set of land surface state variables and fluxes by using current state-of-art land surface models (LSM) driven with 10-year period of data provided by the International Satellite Land Surface Climatology Project Initiative II (ISLSCPII) data set. All models that participated in GSWP-2 experiments were driven by hybrid meteorological forcing (precipitation, temperature, radiation) from global reanalysis, rescaled by gridded observations and satellite products where available. For precipitation, NCEP-Department of Energy (DOE) is used as reanalysis data combined to GPCP satellite data. Common global data sets of vegetation and soil properties were provided as parameter sets for the GSWP-2 LSMs.

3.4 Evaluation

3.4.1 Precipitation

Zonal distribution

The comparison of the seasonally and annually averaged zonal means of precipitation in Fig 3.1 shows a larger ITCZ year-round for both resolutions . The peak is shifted five degrees south in both data sets in DJF (December-January-February). The amplitude of the tropical precipitation is generally well-captured, although exaggerated, most notably during DJF in comparison to GPCP, and generally more strongly in T63l31 resolution than T42L31

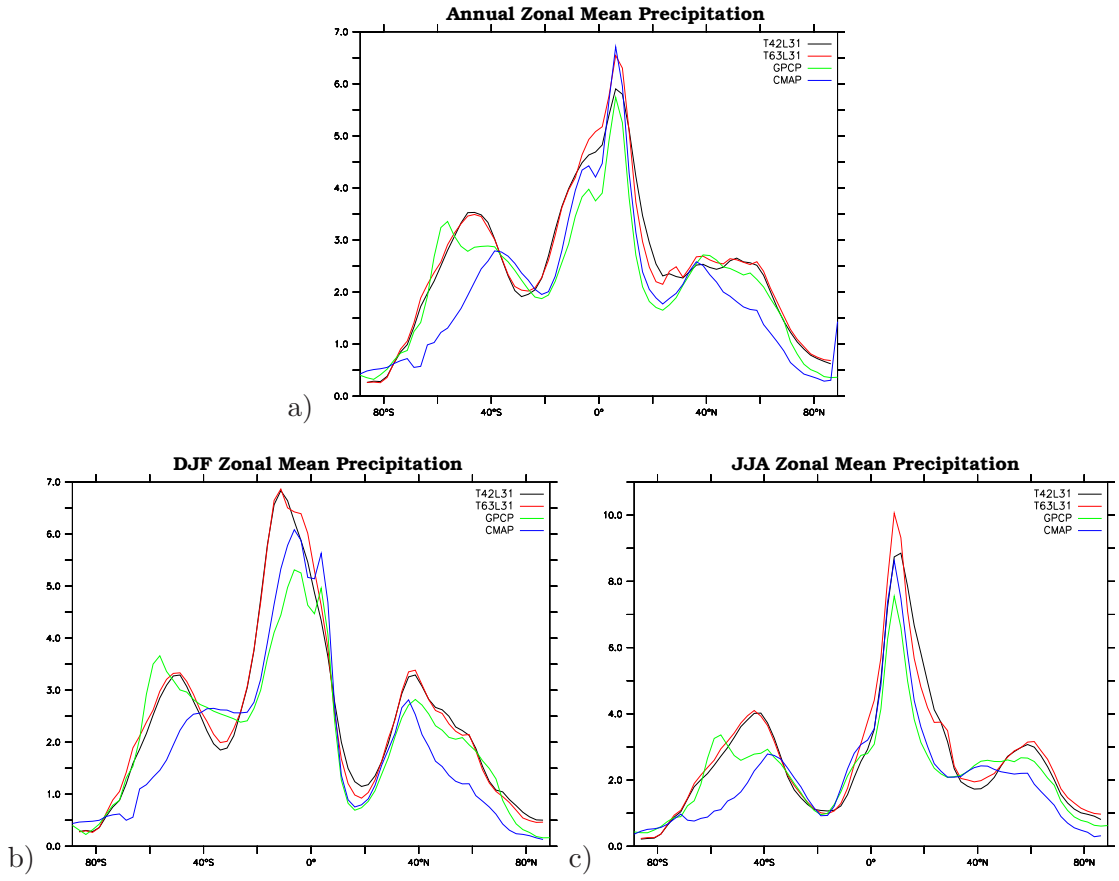

Figure 3.1: Zonally averaged annual precipitation (a), DJF precipitation (b) and JJA precipitation (c) in mm/day for the EMAC model at T42L31 resolution, T63L31 resolution, GPCP and CMAP

during JJA. The differences between GPCP and CMAP especially in tropical regions (CMAP is higher than GPCP), may be due to the atoll adjustment that is applied to the CMAP data in the western Pacific Ocean and to differences in satellite-based precipitation estimates that are used over the oceans. Yin et al. (2004) find that the GPCP data are more accurate in their diagnostics of marine precipitation. On the high latitude storm tracks, GPCP is wetter than CMAP due to the use of TOVS data in GPCP. The model is closer to GPCP in both hemispheres although the distribution is better captured in the northern hemisphere. In the southern hemisphere, the peak around 50S is unrealistic in most seasons.
To achieve a more objective view of the performance of the EMAC model in its T42L31 and T63L31 resolutions in comparison with both datasets GPCP and CMAP, a statistical analysis is performed in Table 3.1, calculating the mean values, the bias, the normalized root mean square error (NRMSE) and the correlation compared to the observations. The mean value of the observations is 2.62 mm/day for GPCP and 2.56 mm/day for CMAP respectively. Both model resolutions overestimate this value, with lower biases against GPCP than against CMAP, but slightly lower NRMSE for CMAP. High correlations are found for both comparisons.

Table 3.1: Statistics of the precipitation analysis from the model simulations compared with the GPCP and CMAP satellite data.

	Comparison with GPCP			
	Mean (mm/day)	Bias (%)	NRMSE (-)	Correlation r^2
GPCP	2.62	-	-	-
T42L31	3.01	13.3	0.66	0.86
T63L31	3.07	15.1	0.67	0.86
	Comparison with CMAP			
CMAP	2.56	-	-	-
T42L31	3.01	22.7	0.60	0.84
T63L31	3.07	24.5	0.63	0.84

Spatial distribution

The horizontal distribution of the 10-year average of T42L31 model precipitation is shown in Figs. 3.2 and 3.3 in comparison with precipitation estimates from GPCP and CMAP. The seasonal distribution is presented in Figure 3.3. EMAC captures many of the observed features in the global precipitation distribution. However, serious errors occur on regional scales over land in comparison to both CMAP and GPCP (only GPCP shown). Precipitation is excessive along steep mountain chains (Himalayas, Andes and Rocky Mountains), Alaska and in the Intertropical Convergence Zone (ITCZ) over land: central Africa, central America, Brazil and Indonesia. In boreal summer (JJA, June-July-August) high biases are also found over the

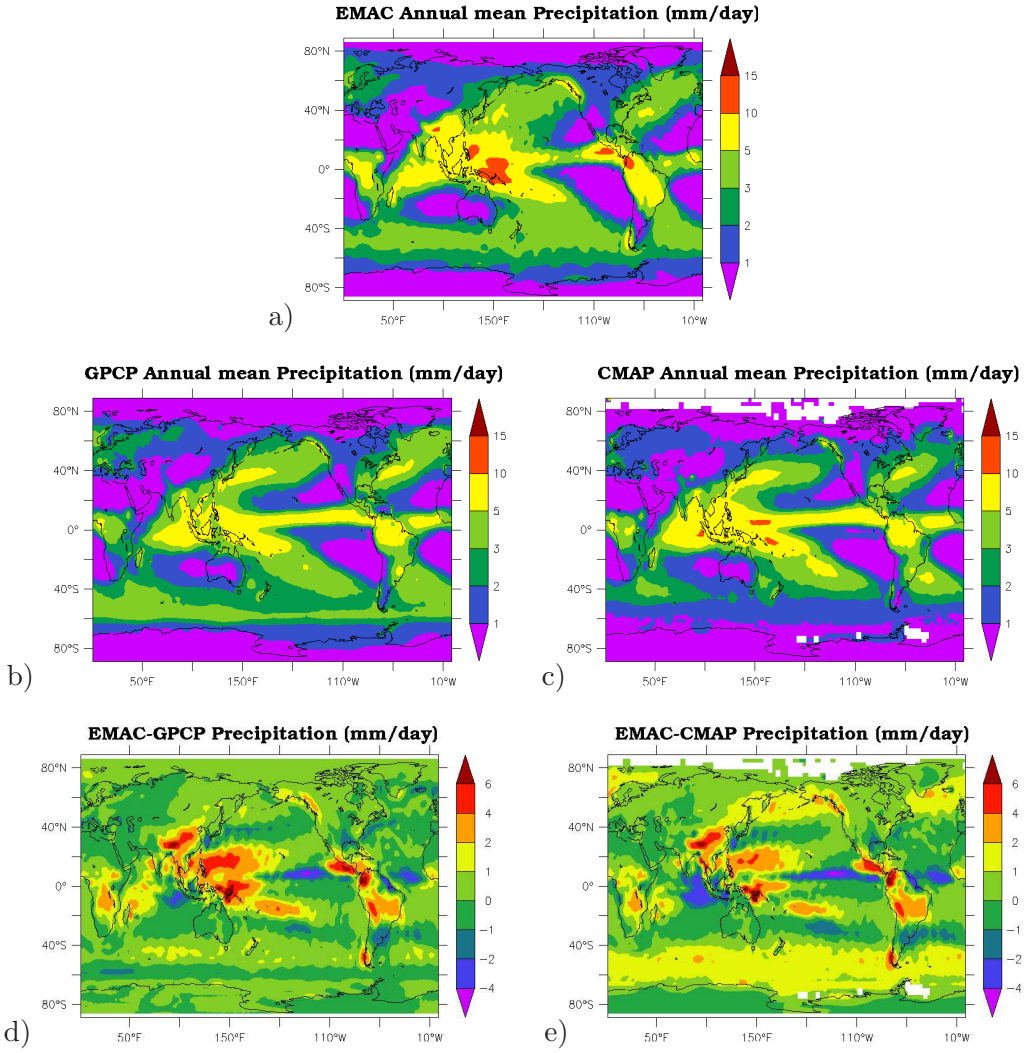

Figure 3.2: Spatial distribution of annual mean precipitation in mm/day for the EMAC model at T42L31 resolution (a), GPCP (b), CMAP (c) and the differences between EMAC and GPCP (d) and between EMAC and CMAP (e).

Indochina Peninsula, China and India and southeast of the United States . Over the ocean, precipitation is overestimated in the west Pacific warm pool and the Indian Ocean where the precipitation regime is displaced to the west extending from west Madagascar to west India. The model has difficulty in positioning the South Pacific Convergence Zone (SPCZ), which is too strong in amplitude and does not extend enough into the southern Pacific.

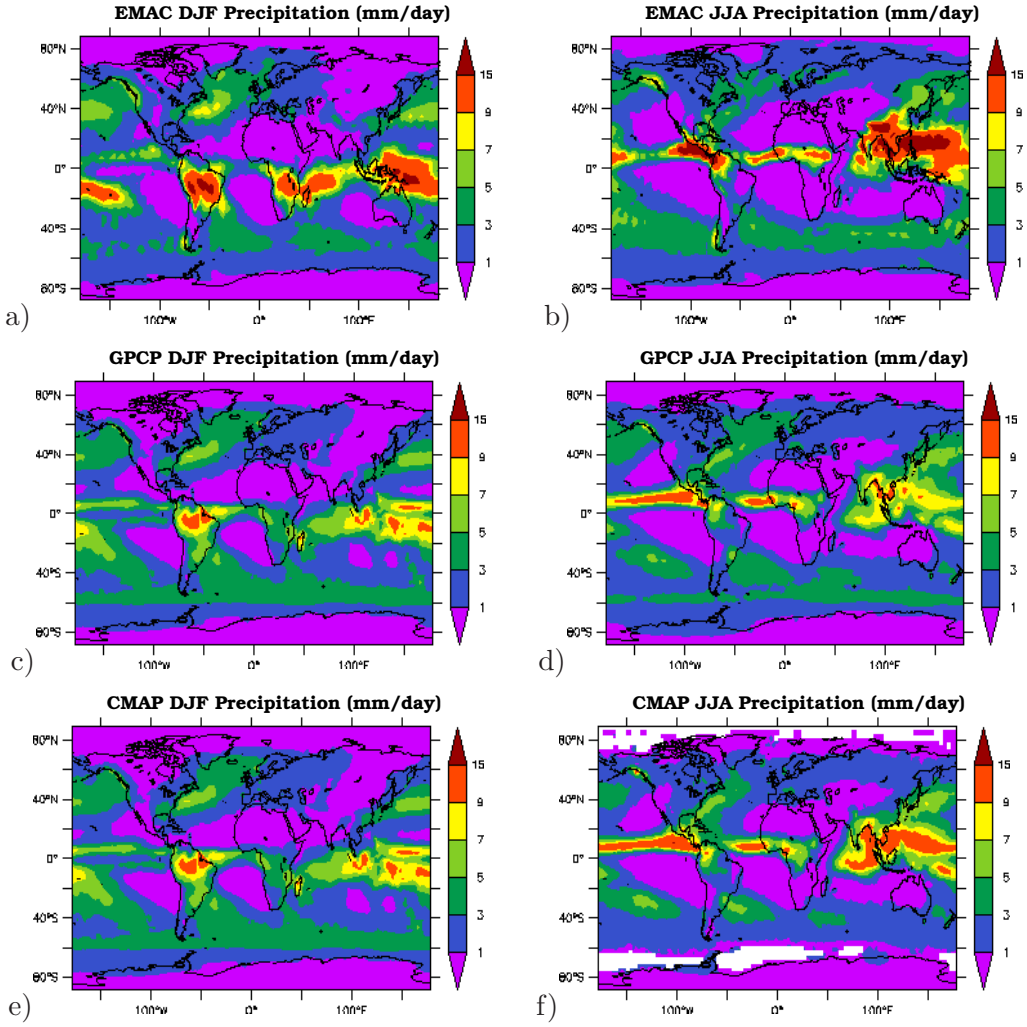

Figure 3.3: Spatial distribution of seasonal mean precipitation in mm/day : (a) EMAC at T42L32 resolution DJF mean precipitation, (b) EMAC at T42L32 resolution JJA mean precipitation, (c) GPCP DJF mean precipitation, (d) GPCP JJA mean precipitation, (e) CMAP DJF mean precipitation, (f) CMAP JJA mean precipitation and their differences: (g) between EMAC and GPCP DJF mean precipitations, (h) between EMAC and GPCP JJA mean precipitations, (i) between EMAC and CMAP DJF mean precipitations, (j) between EMAC and CMAP JJA mean precipitations.

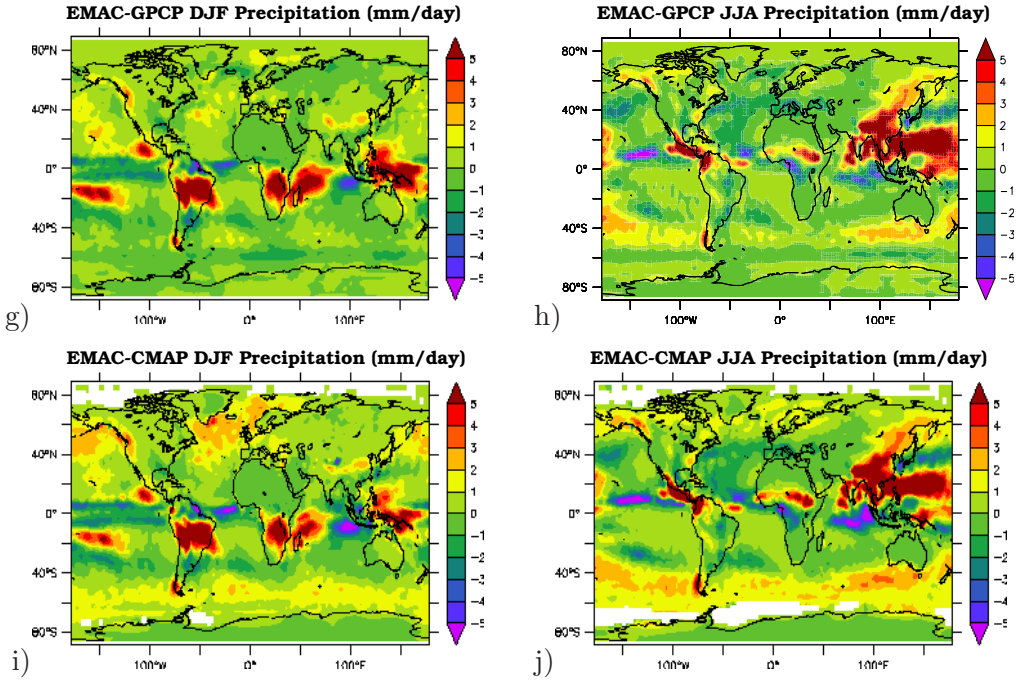

Figure 3.3: Continued.

Another model deficiency is the underestimation of the Atlantic ITCZ in all seasons except in JJA, when the western part of the ITCZ is shifted south towards French Guyana. There are also some deficiencies in the central tropical Pacific, where precipitation is underestimated and off the coast of Central America where it is shifted to the north in boreal winter and spring. The South Atlantic Convergence Zone (SACZ) is quite well depicted in amplitude but also shifted to the east which causes the precipitation to be underestimated over Eastern Argentina and Uruguay.

3.4.2 Evapotranspiration

The evapotranspiration fields are provided by the GSWP2 data set only over land without Antarctica in a resolution of 1° by 1°. For comparison, model evapotranspiration is regridded at the same resolution. In Fig. 3.4 the zonally averaged seasonal and annual distribution of evapotranspiration are shown. The amplitude of the tropical evapotranspiration is much too strong in the ITCZ in all seasons. Subtropical evapotranspiration is displaced too far poleward seasonally and annually. Too high evapotranspiration occurs also in the extratropical northern hemisphere in boreal winter, and T63L31 slightly exaggerates the peak around 45°N in JJA.

Figure 3.5 shows the horizontal distribution of evapotranspiration in both seasons DJF and JJA. As suggested by the zonal means, EMAC exhibits a clear evapotranspiration overestimation over the ITCZ year-around. Exceptions are found over Surinam and the Guyanas in DJF and central Brazil in JJA.

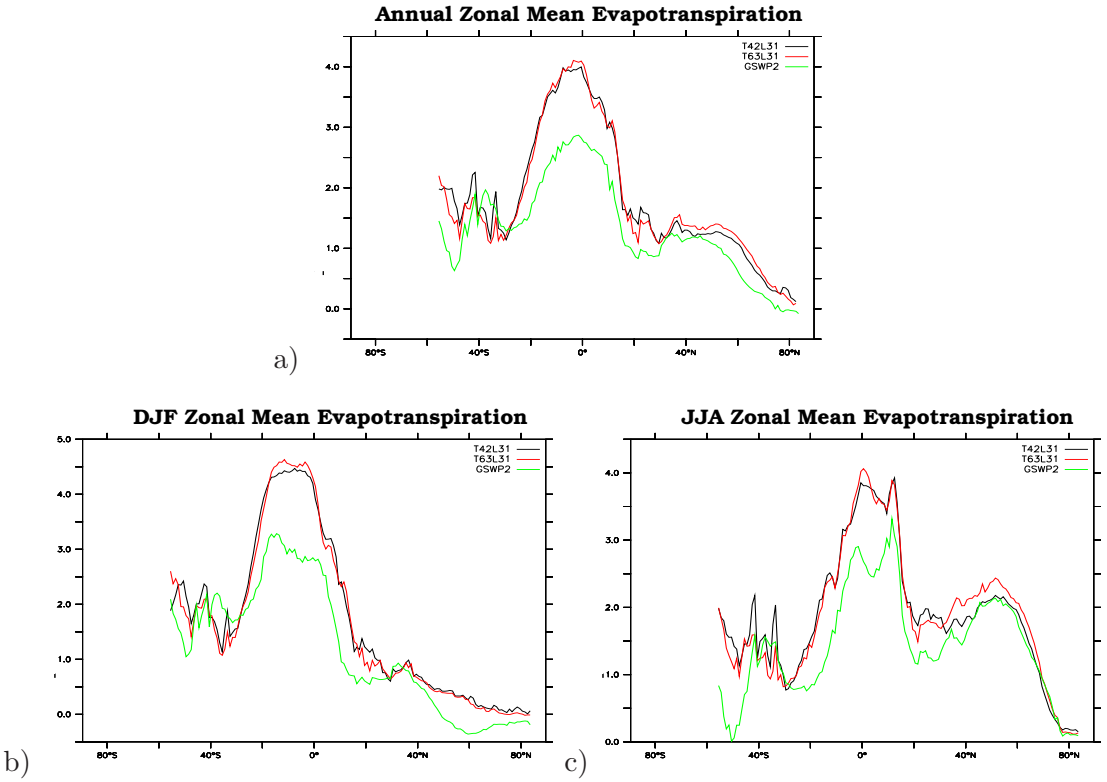

Figure 3.4: Zonally averaged annual Evapotranspiration (a), DJF Evapotranspiration (b) and JJA Evapotranspiration (c) in mm/day for EMAC T42L31 resolution, T63L31 resolution and GSWP-2. Only Evapotranspiration over land is considered.

Note that in regions with dense vegetation like the Amazon forest or the Congo Basin, direct evaporation from vegetation (interception loss) contribute largely to the total evapotranspiration. This will be treated in more detail in the following chapter. Evapotranspiration is also underestimated over parts of Argentina and Uruguay in boreal winter, while in North America the model is dry over Texas in the United States but rather wet over the Rocky Mountains and the eastern part of the country.
Correlations are found between precipitation and evapotranspiration in regions with high precipitation like the ITCZ. Too strong precipitation contributes to too large evaporation rates.

Likewise, too weak precipitation causes the interception loss to decrease and the transpiration to stop (Guyanas and Uruguay). This is particularly true in densely-vegetated regions in the tropics.

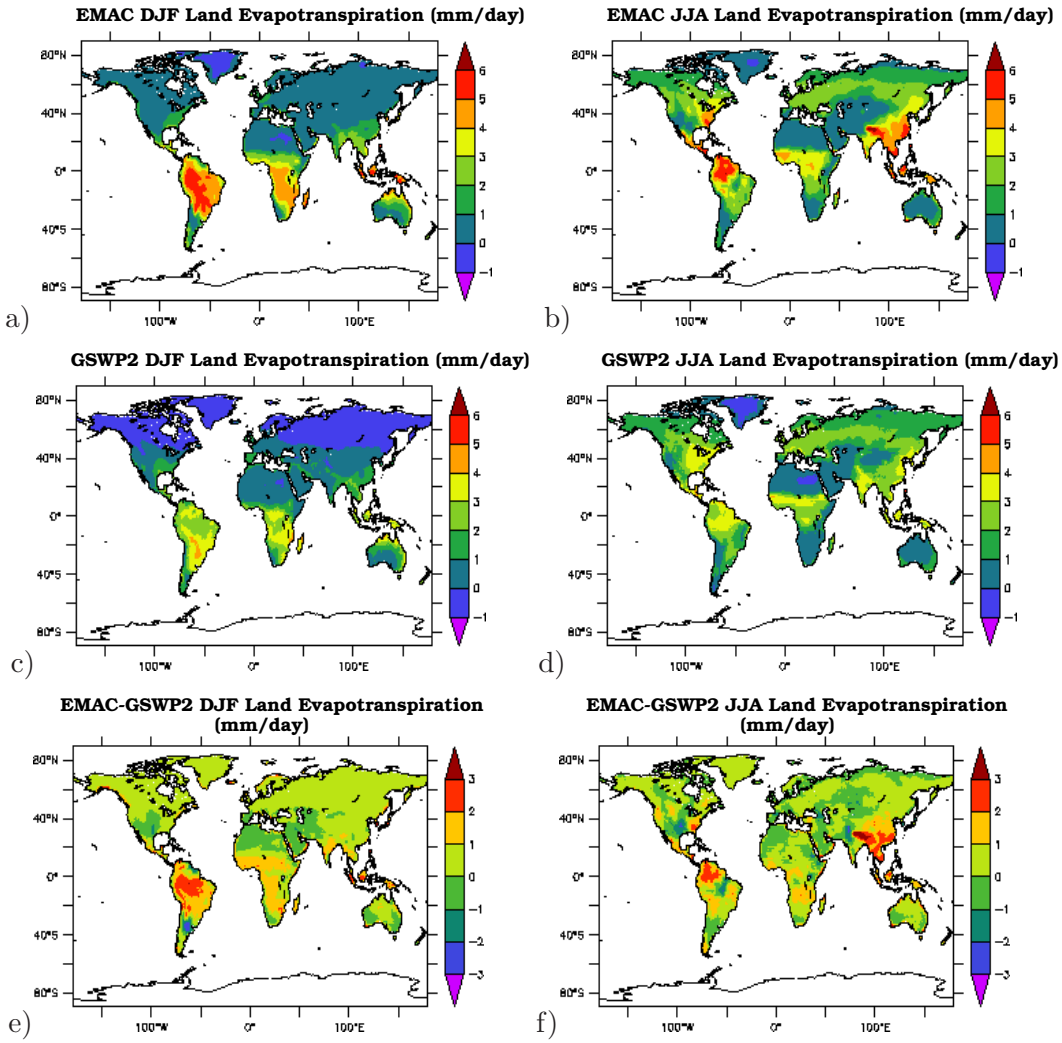

Figure 3.5: Spatial distribution of seasonal mean land evapotranspiration in mm/day for EMAC model at T42L31 resolution (a), GSWP2 land evapotranspiration (b) and the difference between EMAC and GSWP2 land evapotranspiration (c).

3.4.3 Moisture convergence P-E

The surface freshwater exchange is defined by the evaporation and precipitation fields. The seasonally averaged horizontal distribution of P-E is shown in Figure 3.6. A comparable observational dataset does not exist because global observational data for evaporation is not available. The GSWP2 precipitation and evaporation are only used for land comparison. The maxima in P and thus in P-E occur in the summer of each hemisphere in the tropics while the strongest

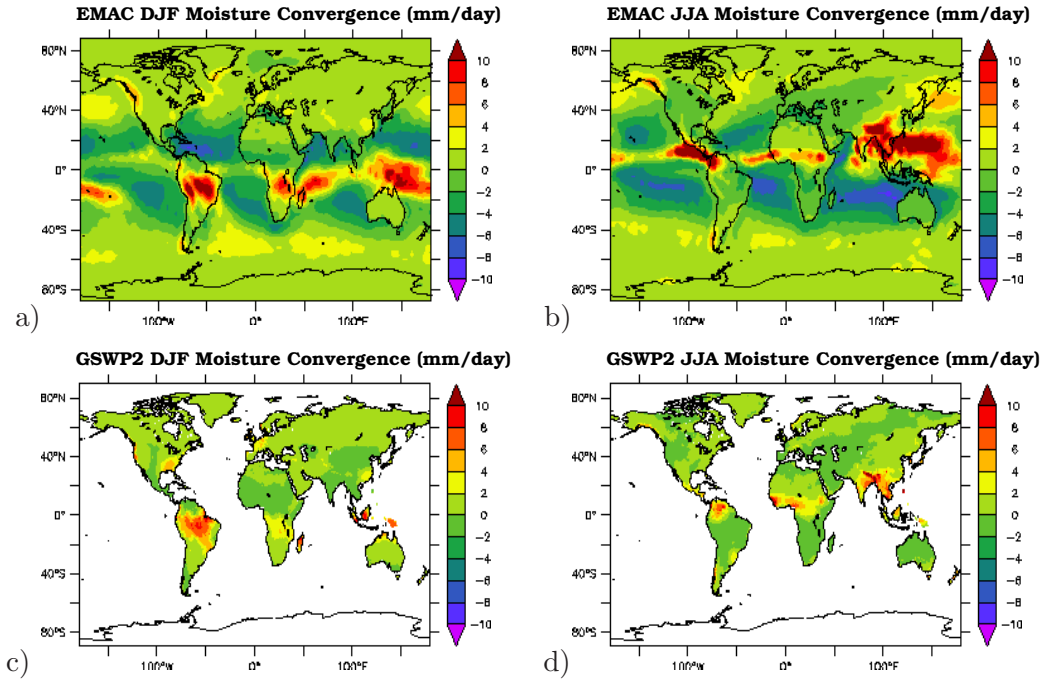

Figure 3.6: Spatial distribution of seasonal mean moisture convergence in mm/day for (a) EMAC at T42L31 resolution for DJF, (b) EMAC at T42L31 resolution for JJA, (c) GSWP2 for DJF, (d) GSWP2 for JJA.

evaporation (minima in P-E) occurs in the subtropics in winter. In the Northern Hemisphere there is a further maximum each winter north of 40N associated with the development of the storm tracks over the oceans and the associated maximum precipitation. The eastern Pacific and Indian Oceans are the principal sources of water for the atmosphere. Over land, a large seasonal cycle is observed over the ITCZ. The northern part of South America can be considered as water sink in DJF and a water source in JJA for both resolutions and for GSWP2, although the north east (Venezuela) lacks moisture in the model in DJF and acts as moisture sink all year round. Over Argentina, the JJA moisture convergence is underestimated in the T42L31

simulation but not in T63L31, even though both simulations underestimate precipitation in the SACZ. In the northern hemisphere, moisture convergence is underestimated in the southeastern US in comparison to GSWP2.

3.4.4 Water Vapor

Comparison with GOME/SSMI

The GOME water vapor climatology data set (GWC) consists of monthly mean global distributions of TWVC for cloud-free situations only. In case of missing data throughout the month and between about 70°S and 70°N and over ocean surfaces only SSM/I monthly means have been used to fill the gaps, especially in regions around the ITCZ. SSM/I data contributes to less than 5% to the merged data set.

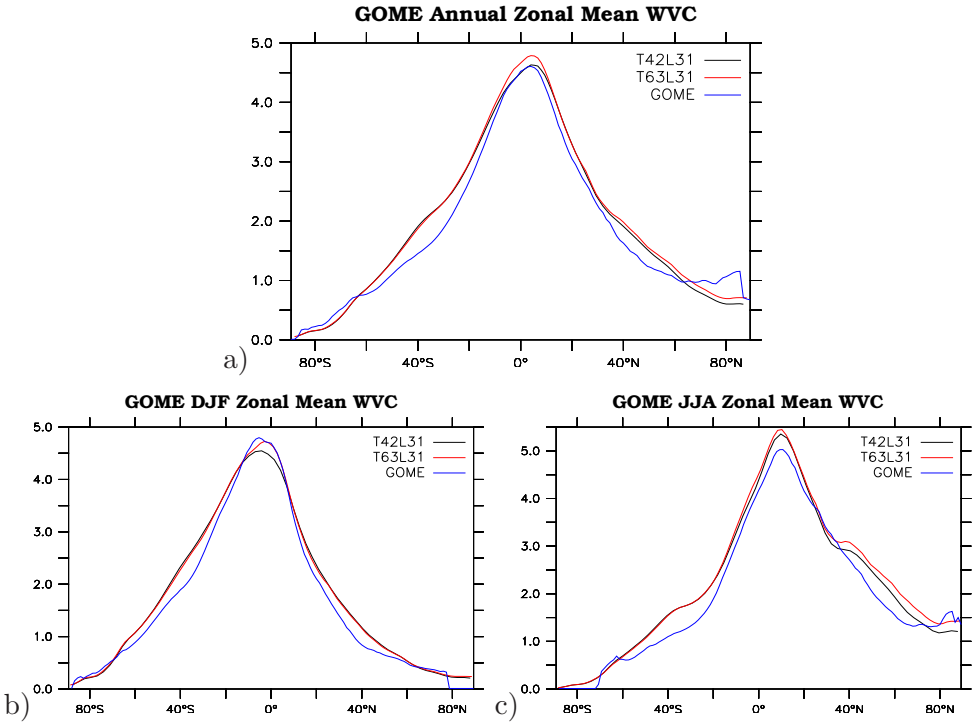

Figure 3.7: Zonally averaged annual total water vapor column (a), DJF total water vapor column (b) and JJA total water vapor column (c) in cm for EMAC T42L31, T63L31 and GOME.

The drawbacks of GWC over land have been discussed in detail in Lang and Lawrence (2005b) and Lang et al. (2007). This includes a moist bias around 15 north of the Equator over Africa, an underestimation of the TWVC over regions with a dense vegetation like tropical rainforest and large dry biases (up to 0.5 cm) due to the systematic effect of clouds in ITCZ regions with high WVC.

The zonal mean of EMAC is shown in Fig. 3.7 along with GOME-SSM/I. The model is in good agreement with observations. The largest biases are present all-year-long near 40°N and 40°S. The T63L31 resolution is found to show a higher peak around the Equator in comparison with GWC or T42L31. Along the ITCZ, the differences observed are due to compensation of errors in the longitudinal distribution.

Fig. 3.8 shows the horizonal distribution of seasonally-averaged TWVC and their differences from GWC. EMAC generally captures well the structure and magnitude of TWVC in the atmosphere. There are, however, large-scale biases despite the relatively good agreement in the zonal mean. EMAC is significantly moister over Northern Hemisphere oceans, and over the SPCZ, south-western Indian Ocean and SAZC in the Southern Hemisphere. TWVC is underestimated in DJF over the Atlantic ITCZ, the tropical eastern Pacific (off the coast of Peru) and the Indo-Pacific Warm Pool. Over land, the model is systematically moist in the Amazon, over Uruguay and Northern Argentina, Central America. The tropical African TWVC also shows large positive biases in the southwestern part of the continent in boreal winter, but the model is considerably dry over Angola in Summer. In general terms, the model is moist over Northern Hemisphere continental regions during JJA except in very dry areas like northern Africa and the Arabian Peninsula where the model is rather too dry. This might be attributed to the strong impact of dust aerosols on the GOME retrieval method in these regions in summer and may not be a real feature. In the southern hemisphere, the dryness can be observed off the coasts of Peru and Angola all through the year and off the coast of West Australia in winter. This is consistent with the underestimation of the shortwave cloud forcing off the coast of these regions and negative biases in both longwave cloud forcing and shortwave cloud forcing over the continent discussed by Wild and Roeckner (2006). The dry bias over the Andes and parts of the Himalaya mountains might also not be a real deficiency in the model but rather a problem for GWC. No large differences in the main features are found comparing T63L31 with GOME, except a stronger positive bias in eastern North America, Europe and over Russia in JJA.

The statistical analysis presented in Table 3.1 shows a systematic positive bias of less than 15%, with high correlation coefficients, being more than 0.8 globally and over all continents except Europe. The NRMSE is relatively small in general, with the lowest values found for Europe. This might be due to the low variability of the TWVC in time and in space over this continent in comparison with other continents. For T63L31 there are in general larger biases globally and regionally in comparison with T42L31.

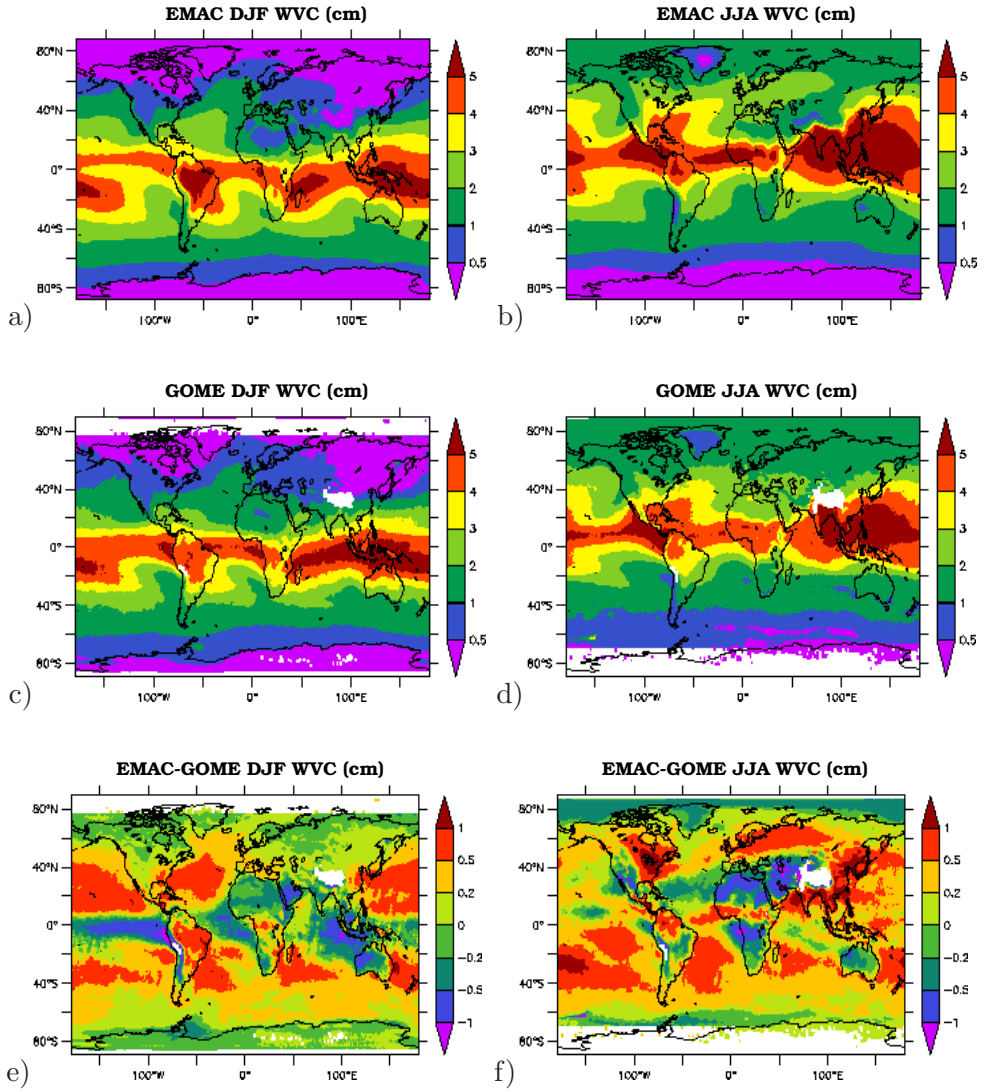

Figure 3.8: Spatial distribution of seasonal mean total water vapor column in cm: (a) EMAC T42L31 resolution in DJF, (b) EMAC T42L31 resolution in JJA, (c) GOME in DJF, (d) GOME in JJA, and the difference: (e) between EMAC and GOME in DJF, (f) between EMAC and GOME in JJA.

In locations where the TWVC is large, especially near the ITCZ, we find a high bias in model precipitation. Thus the high bias in TWVC in the tropics could be a factor in contributing to

larger model rainfall rates. This is not always true. High TWVC over the eastern USA and Canada and over Argentina and Uruguay in DJF are not correlated with high precipitation rates and have rather lower values. This implies a relatively long residence time of water vapor or the formation of non-precipitating clouds in these regions.

Comparison with MCOS

MCOS data set is provided at a resolution of 2° by 2° with monthly-means from 1980 to 2003. For comparison, model TWVC were regridded to the same 2° resolution as the observations. The observed and modeled monthly means were used to create 10-year mean values for each month.

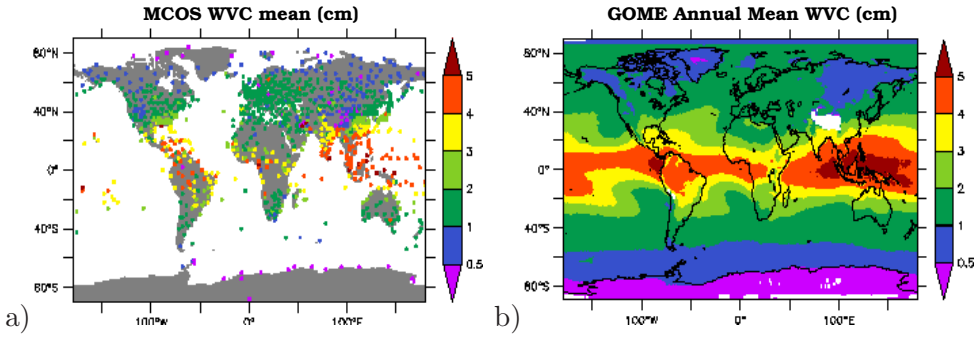

Figure 3.9: Global distribution of (a) annual mean T42L31 Total water vapor column and (b) the MCOS Total water vapor column (in cm).

The frequency distribution of TWVC for the model and MCOS are shown in Figure 3.10. The peak corresponds to low TWVC observed mainly in the subtropics and midlatitudes. Best agreements are found for values between 2 and 5 cm but a lack of variability is found above 5 cm and an overestimation at the low end of the distribution. The regional distribution of the 10-year average of EMAC T42L31 and MCOS shown in Figure 3.9 suggests a good comparison between the model and the data set over all the continents and over islands although the sondes are scarce in the Southern Hemisphere. Exceptions are found in very few sonde sites on the edge of high mountain chains like the Himalaya or the Zagros mountains. Correlation for all seasons is found to be higher than 0.8 with a slope of almost 1. Fig. 3.11 shows the comparison between the model and the data set. The scatter plot compares annually mean values for continents with a significant number of sonde stations (Africa and Australia are excluded). It shows an overestimation of the Model South American TWVC and a slight underestimation of the Asian and Indonesian columns in winter and an overall overestimation in summer. This is consistent with the comparisons of the model with GOME. The same overestimation observed in European

and North-American TWVC is also found in summer. The statistics of the comparison are summarized in Table 3.2. The comparison of the times series of 10-year EMAC with GOME and MCOS are presented in Figure 3.11 for the tropics, subtropics and midlatitudes. TWVC in both simulations are in general overestimated in boreal summer. In the tropics, the T63L31 resolution shows a stronger peak in summer 1998 corresponding to an ENSO signal.

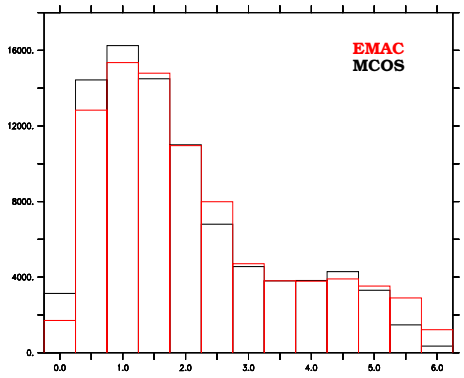

Figure 3.10: Frequency distribution of the total water vapor column for EMAC (red) and MCOS (black).

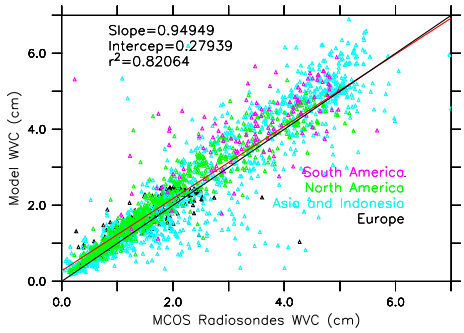

Figure 3.11: Scatter plot of EMAC and MCOS total water vapor column (in cm) for all seasons and for Europe, North America, South America, Asia and Indonesia.

The comparison of the times series of 10-year EMAC with GOME and MCOS are presented in Figure 3.11 for the tropics, subtropics and midlatitudes. TWVC in both simulations are in general overestimated in boreal summer. In the tropics, the T63L31 resolution shows a stronger peak in summer 1998 corresponding to an ENSO signal.

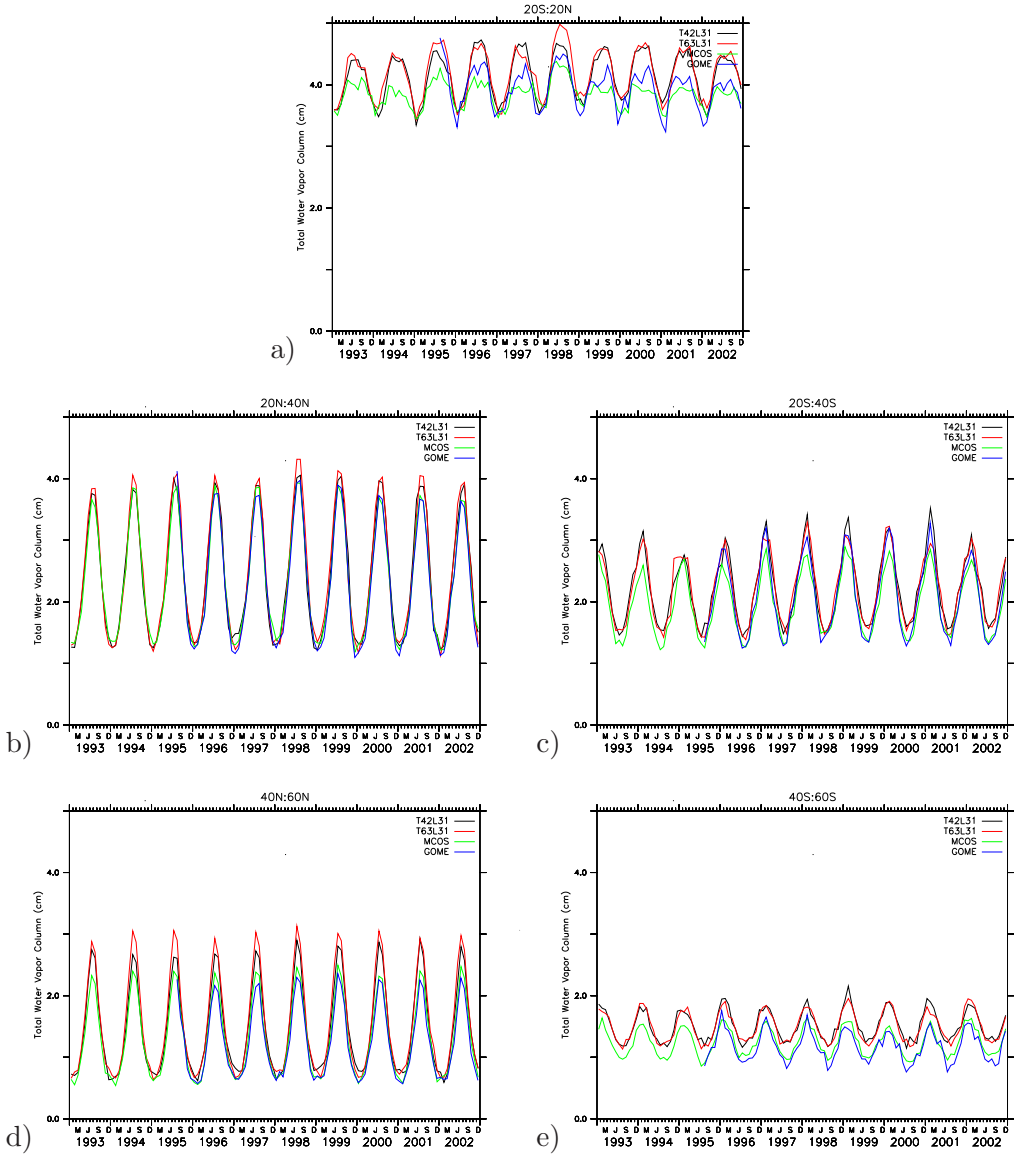

Figure 3.12: Comparison between EMAC, MCOS and GOME total water vapor column for the latitude ranges: (a) 20S:20N or the tropics, (b) 20N:40N latitude range, (c) 20S:40S latitude range, (d) 40N:60N latitude range and (e) 40S:60S latitude range.

Table 3.2: Statistics of the total water vapor column analysis from the EMAC model resolutions T42L31 and T63L31 compared with GOME for the globe and the latitude bands 20S:20N, 20N:40N, 20S:40S, 40N:60N and 40S:60S.

T42L31						
	Global	20S:20N	20N:40N	20S:40S	40N:60N	40S:60S
Model Mean (cm)	2.16	4.12	2.37	2.21	1.45	1.49
Obs. Mean (cm)	2.00	3.83	2.30	1.94	1.28	1.22
Model STD (cm)	1.52	1.21	1.53	0.95	0.85	0.37
Obs. STD (cm)	1.53	1.25	1.70	0.87	0.75	0.33
Bias (%)	8.22	7.73	3.32	13.49	13.22	21.85
Norm. RMSE	0.55	0.72	0.75	0.69	0.54	0.67
r	0.84	0.72	0.68	0.78	0.87	0.81
T63L31						
	Global	20S:20N	20N:40N	20S:40S	40N:60N	40S:60S
Model Mean (cm)	2.22	4.18	2.42	2.19	1.54	1.48
Obs. Mean (cm)	2.00	3.83	2.30	1.94	1.28	1.22
Model STD (cm)	1.54	1.25	1.55	0.96	0.92	0.35
Obs. STD (cm)	1.53	1.25	1.70	0.87	0.75	0.33
Bias (%)	11.14	9.07	5.43	12.84	19.55	20.79
Norm. RMSE	0.54	0.70	0.74	0.68	0.56	0.62
r	0.85	0.75	0.70	0.79	0.88	0.82

3.4.5 Humidity and temperature fields

The simulated humidity and temperature fields are compared with those derived from MCOS. We emphasize water vapor in the lower and middle troposphere because the primary interest in this thesis in the exchanges of water vapor between the surface and the lower part of the atmosphere. Moreover the quality of the humidity sensors of the radiosondes is questionable in the upper troposphere and their accuracy below -30°C is often poor (Miloshevich and Oltmans, 2004). Figure 3.13 summarizes the comparisons with observations in a Taylor diagram (Taylor, 2001) for the 120 months of the considered time period and for 3 vertical levels: the surface (pluses), the middle troposphere at 3km altitude (crosses) and the upper troposphere at 7km altitude (triangles). The model output (T42L31 and T63L31) has been interpolated to match the MCOS grid horizontally and vertically. The model-observations correlation is the highest for temperature for all altitudes with a correlation coefficient higher than 0.8 and a normalized standard deviation (NSTD) close to 1, suggesting a good seasonal variability and low model biases. Poorer agreement with observations is found for relative humidity, with a correlation around 0.5 for all altitudes and a normalized standard deviation higher than 1. A good agreement is also found for specific humidity, except at 7km altitude where the correlation is less than 0.4 and a very low NSTD of about 0.2. Both resolutions show similar results for all altitudes. The apparent inconsistency between the good correlation of specific humidity and temperature with observations and the less good correlation of the relative humidity is due to the extreme sensitivity of the relative humidity to changes in specific humidity and temperature. A more detailed analysis is given in the next paragraphs.

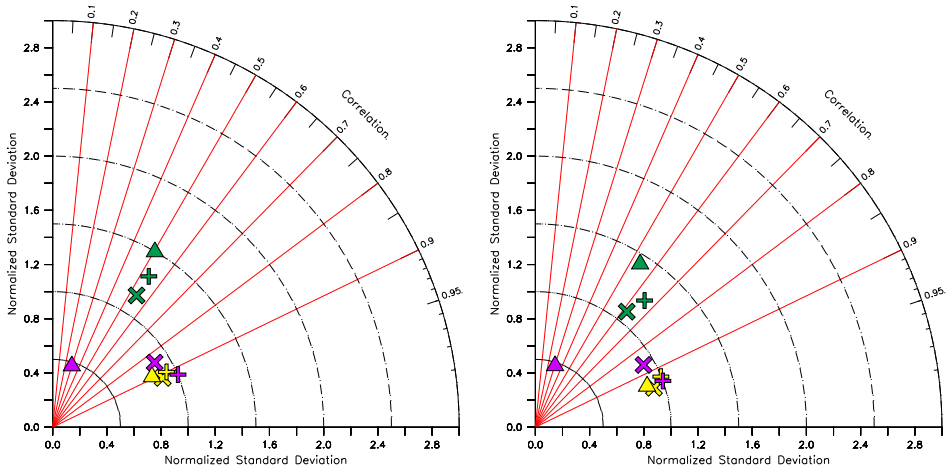

(a) T42L31 (b) T63L31

Figure 3.13: Taylor diagram for T42L31 (a) and T63L31 (b) specific humidity (purple), relative humidity (green) and temperature (yellow). The various altitudes are indicated by the the symbols: pluses (surface), crosses (3km) and triangles (7km)

Specific humidity

In the scatter plot displayed in Fig. 3.14, the comparison of simulated and observed Q shows a high correlation coefficient and a slope of 0.85. A wet bias can be seen for altitudes between surface and 3km and a dry bias at the higher altitudes.

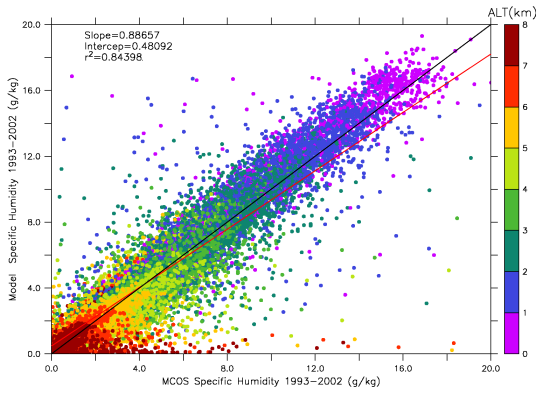

Figure 3.14: Scatter plot of the seasonal mean model specific humidity (in g/kg) with MCOS color-coded according to the altitude.

Additionally Table 3.3 accompanies vertical profile figures (Fig. 3.15) with a summary of statistics of the specific humidity from the T42L31 model simulation compared with MCOS. As mentioned above, the quality of the humidity sensors remains questionable in the upper troposphere, where the MCOS standard deviation is 1.33 g/kg, more than twice its mean and much higher than the simulated standard deviation for the same locations (0.83 g/kg). Moreover, a low correlation coefficient (r=0.33) is calculated at 7km altitude, whereas high correlation coefficients (r=0.9) are found for the surface and the middle troposphere. In Figure 3.15 we compare model calculated vertical profiles of Q from both simulations with MCOS averaged for different latitude ranges and for boreal winter and boreal summer.

Table 3.3: Statistics of the specific humidity analysis for the EMAC model resolution T42L31 compared with MCOS for the globe and the latitude ranges 20S:20N, 20N:40N, 20S:40S, 40N:60N and 40S:60S at the surface, 3km altitude and 7 km altitude.

	at the surface					
	Global	20S:20N	20N:40N	20S:40S	40N:60N	40S:60S
Model Mean (g/kg)	7.76	14.93	9.89	8.45	5.29	5.46
Obs. Mean (g/kg)	7.69	14.42	9.14	7.86	4.70	4.61
Model STD (g/kg)	6.10	2.98	4.68	2.91	3.17	1.43
Obs. STD (g/kg)	5.32	3.31	4.84	2.73	2.65	1.21
Bias (%)	0.84	3.58	8.29	7.45	12.67	18.57
Norm. RMSE	0.42	0.84	0.62	0.60	0.57	0.62
r	0.93	0.60	0.79	0.82	0.87	0.85
	at 3km					
Model Mean (g/kg)	2.71	5.60	3.92	3.09	2.35	1.97
Obs. Mean (g/kg)	3.13	5.97	3.77	2.89	1.98	1.43
Model STD (g/kg)	2.97	2.32	2.56	1.68	1.35	0.49
Obs. STD (g/kg)	2.44	2.32	2.56	1.74	1.25	0.46
Bias (%)	-13.55	-6.14	3.85	6.87	18.81	37.45
Norm. RMSE	0.606	0.88	0.63	0.65	0.62	0.82
r	0.90	0.60	0.80	0.77	0.82	0.67
	at 7km					
Model Mean (g/kg)	0.48	1.15	0.93	0.59	0.42	0.32
Obs. Mean (g/kg)	0.51	1.04	0.66	0.32	0.25	0.25
Model STD (g/kg)	0.83	0.71	0.79	0.36	0.32	1.03
Obs. STD (g/kg)	1.33	2.17	1.28	0.57	0.72	0.46
Bias (%)	-6.24	10.21	40.65	82.04	69.43	28.83
Norm. RMSE	0.98	1.01	0.96	1.02	1.02	1.007
r	0.33	0.12	0.37	0.26	0.17	0.01

The gridded data are averaged in latitude bands around the globe so that the sets can be easily compared for different regions. It must be noted that in many regions the radiosonde data may only include one or a few stations. This may be non-representative of the latitude range. This is particularly the case for African and South-American sondes present in the range 20S to

20N which shows the highest normalized root mean square error (NRMSE) among all latitude ranges and for all altitudes, and in the range 40°S to 60°S containing mainly few sondes in Argentina. The model shows a positive bias in general for all latitudes and for the 3 altitudes, but more pronounced at the surface in JJA, and relatively more significant at most locations in the upper troposphere all over the year. This is consistent with the overestimation of the TWVC in the same latitude ranges shown above (Fig. 3.12 and Table 3.2).

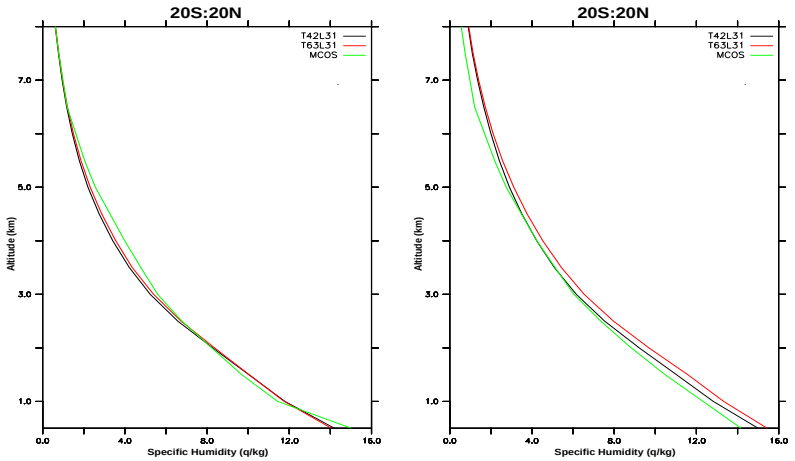

(a) Latitude range 20S:20N for DJF (b) Latitude range 20S:20N for JJA

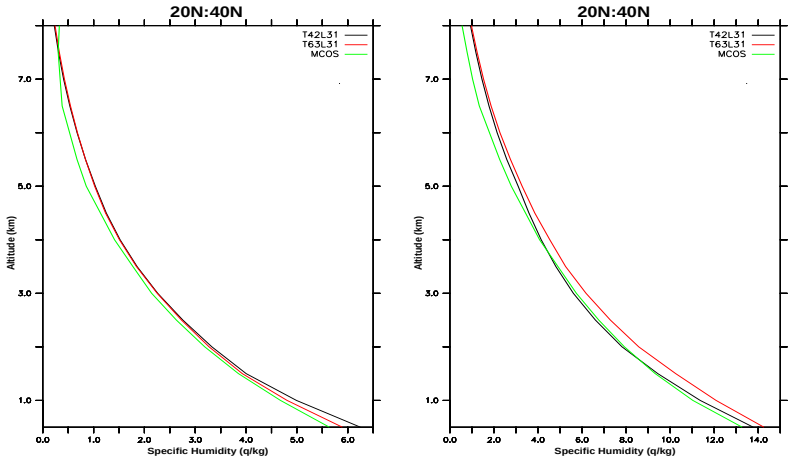

(c) Latitude range 20N:40N for DJF (d) Latitude range 20N:40N for JJA

Figure 3.15: Vertical profiles of specific humidity (in g/kg) for the latitude ranges: (a) 20S:20N DJF, (b)20S:20N JJA, (c) 20N:40N DJF, (d) 20N:40N DJF, (e) 20S:40S DJF, (f) 20S:40S JJA, (g) 40N:60N DJF, (h) 40N:60N JJA, (i) 40S:60S DJF, (j) 40S:60S JJA.

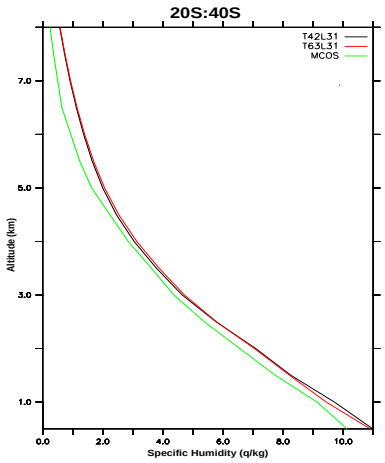

(e) Latitude range 20S:40S for DJF

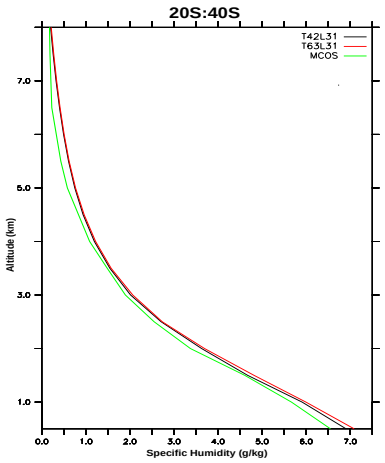

(f) Latitude range 20S:40S for JJA

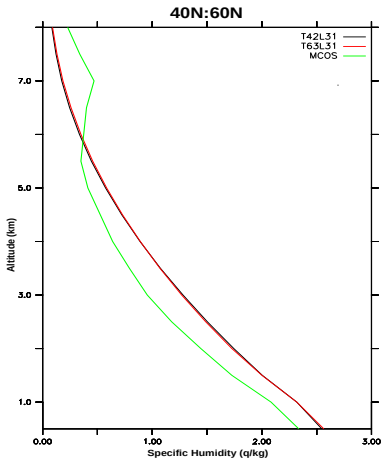

(g) Latitude range 40N:60N for DJF

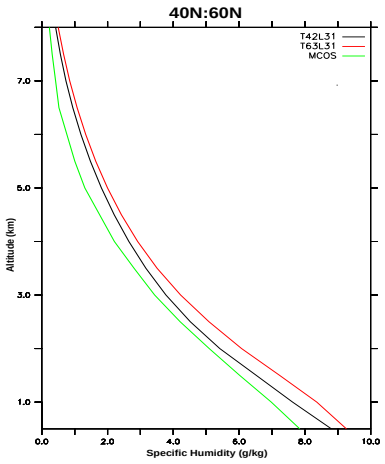

(h) Latitude range 40N:60N for JJA

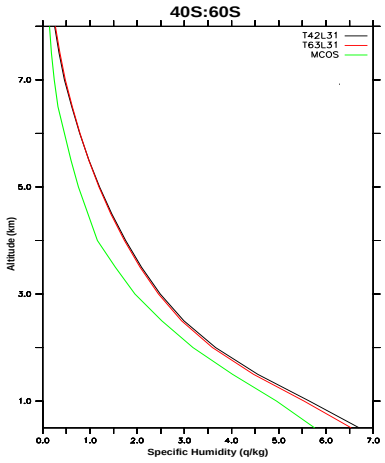

(i) Latitude range 40S:60S for DJF

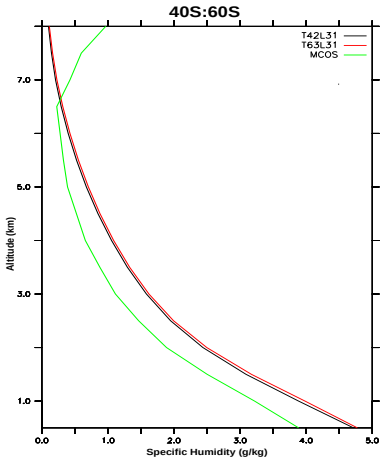

(j) Latitude range 40S:60S for JJA

Figure 3.15: Continued.

Temperature

The simulated temperature of the two resolutions are compared to MCOS in Figure 3.16. Small biases are observed for almost all latitude ranges. Warm biases are generally found above 5km altitude for both resolutions, although T42L31 shows a cold bias of 2 to 4K overall in comparison to T63L31.

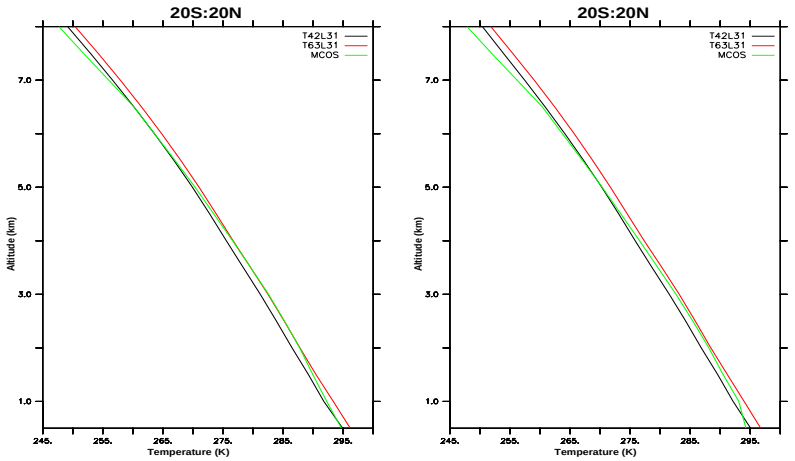

(a) Latitude range 20S:20N for DJF (b) Latitude range 20S:20N for JJA

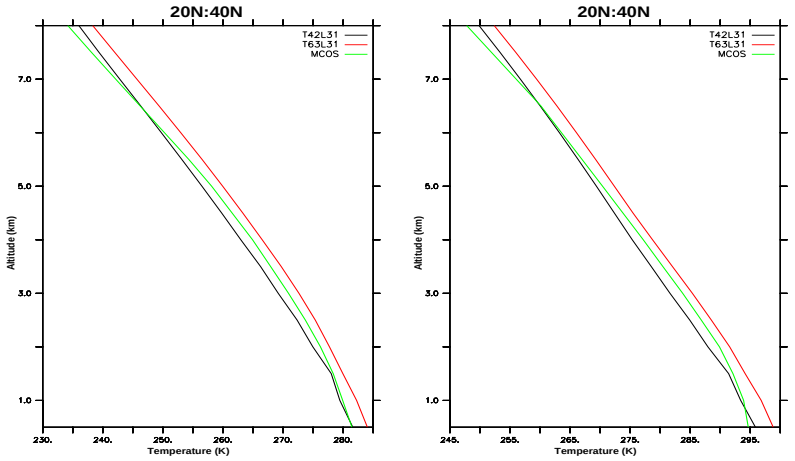

(c) Latitude range 20N:40N for DJF (d) Latitude range 20N:40N for JJA

Figure 3.16: Vertical profiles of temperature (in K) for the latitude ranges: (a) 20S:20N DJF, (b)20S:20N JJA, (c) 20N:40N DJF, (d) 20N:40N DJF, (e) 20S:40S DJF, (f) 20S:40S JJA, (g) 40N:60N DJF, (h) 40N:60N JJA, (i) 40S:60S DJF, (j) 40S:60S JJA.

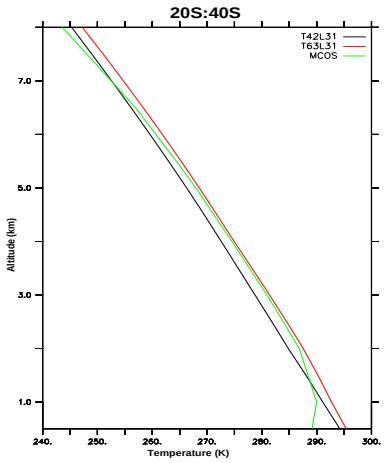

(e) Latitude range 20S:40S for DJF

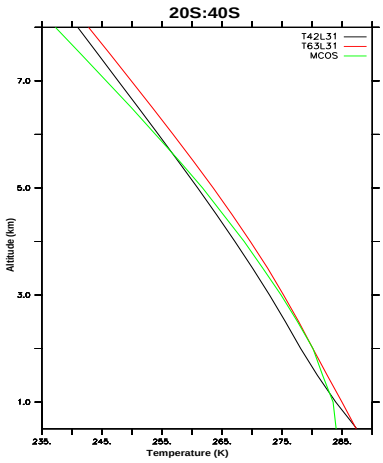

(f) Latitude range 20S:40S for JJA

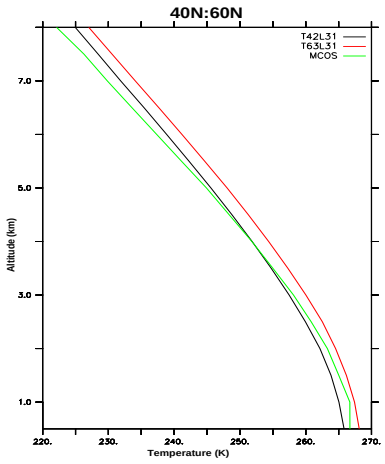

(g) Latitude range 40N:60N for DJF

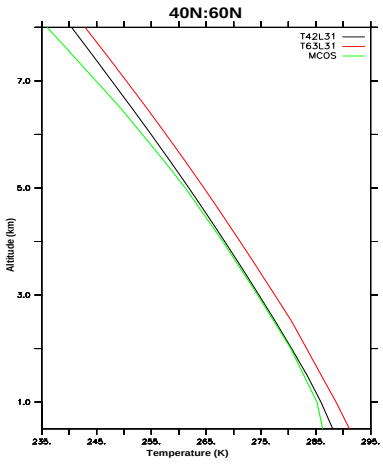

(h) Latitude range 40N:60N for JJA

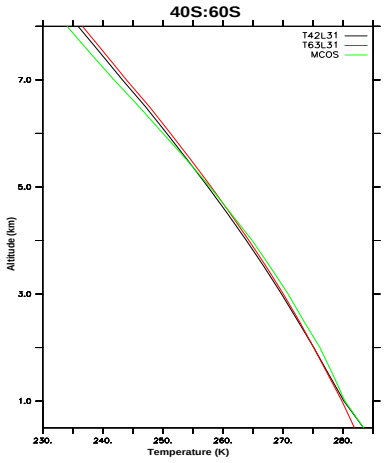

(i) Latitude range 40S:60S for DJF

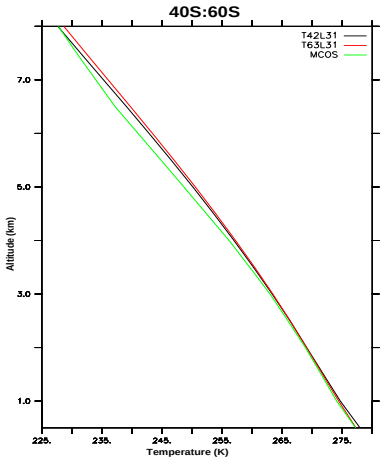

(j) Latitude range 40S:60S for JJA

Figure 3.16: Continued.

As in many studies (Roeckner et al., 2006 and references therein) increasing horizontal resolution leads to a warming of the troposphere. The high correlation coefficient (above 0.7) combined with low biases and relatively low normalized RMSE confirm the good agreement between the T42L31 model resolution and MCOS.

Relative humidity

The scatter plot representing the regression between the model's relative humidity and MCOS for all seasons is shown in Figure 3.17. There is a clear moist bias in the model increasing with altitude. This causes the correlation between the two to be low (r^2=0.51). The increasing bias with altitude is also apparent in Table 3.4 showing the details of the statistical analysis of the comparison for global fields and different latitude ranges. Large biases combined with large NRMSE are found at 7km altitude with relatively low correlation coefficients.

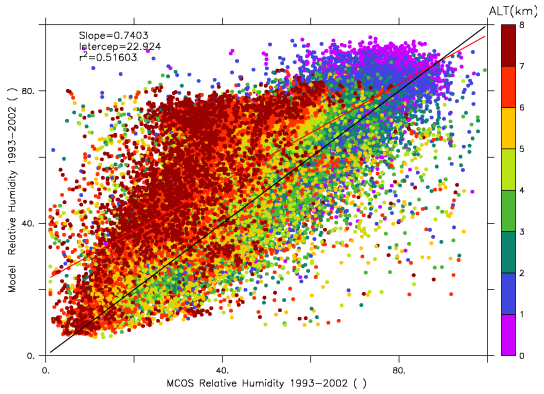

Figure 3.17: Scatter plot of the seasonal mean model relative humidity (in %) with MCOS color-coded according to the altitude.

The vertical profiles presented in Figure 3.18 for DJF and JJA confirm these large biases. These profiles demonstrate the overall C-shaped profile in the tropics and in midlatitudes. The strong increase in relative humidity in the midtroposphere occurs at much lower altitude as what has been observed by the sondes. A rapid increase (not shown here) in tropical relative humidity occurs within the deep outflow layer, which is a layer of enhanced convective flow starting near 10km and extending to 17km (Folkins et al., 2002). Radiosondes fail or underpredict this increase. Folkins et al. (2006) showed that models with more pronounced convective outflow in the upper troposphere simulate better the increase in the the relative humidity and these models are associated with increased evaporative moistening in the middle and lower troposphere. It is beyond the scope of this work to investigate these discrepancies, and

additional observational datasets are needed, and probably more simulations with alternative convection parameterizations might help to understand this early increase of RH.

Table 3.4: Statistics of the relative humidity analysis for the EMAC model resolution T42L31 compared with MCOS for the globe and the latitude ranges 20S:20N, 20N:40N, 20S:40S, 40N:60N and 40S:60S at the surface, 3km altitude and 7 km altitude.

	at the surface					
	Global	20S:20N	20N:40N	20S:40S	40N:60N	40S:60S
Model Mean (g/kg)	78.35	79.79	71.76	66.75	79.72	86.81
Obs. Mean (g/kg)	70.86	76.74	67.34	65.15	69.97	72.40
Model STD (g/kg)	16.36	15.32	17.48	18.49	14.97	8.59
Obs. STD (g/kg)	12.41	13.71	13.83	12.60	10.12	5.96
Bias (%)	10.57	3.97	6.57	2.46	13.93	19.90
Norm. RMSE	1.13	0.85	0.97	1.00	1.44	1.68
r	0.54	0.67	0.64	0.73	0.37	0.07
	at 3km					
Model Mean (g/kg)	54.92	53.29	46.28	41.10	60.91	62.54
Obs. Mean (g/kg)	49.32	54.61	44.49	35.93	51.78	41.89
Model STD (g/kg)	17.89	20.56	18.63	14.48	12.19	11.14
Obs. STD (g/kg)	15.29	17.90	17.16	13.61	10.49	7.61
Bias (%)	11.36	-2.40	4.01	14.37	17.65	49.28
Norm. RMSE	0.98	0.91	0.82	0.98	1.32	1.44
r	0.59	0.64	0.69	0.54	0.25	0.35
	at 7km					
Model Mean (g/kg)	53.89	41.12	48.27	37.10	64.02	64.80
Obs. Mean (g/kg)	35.48	34.28	32.99	21.24	39.95	31.13
Model STD (g/kg)	20.21	22.66	18.20	14.97	12.47	10.71
Obs. STD (g/kg)	13.82	17.15	13.15	8.74	9.92	5.85
Bias (%)	51.90	19.95	46.31	74.66	60.26	33.67
Norm. RMSE	1.22	1.09	1.16	1.43	1.37	1.95
r	0.56	0.58	0.56	0.54	0.27	0.14

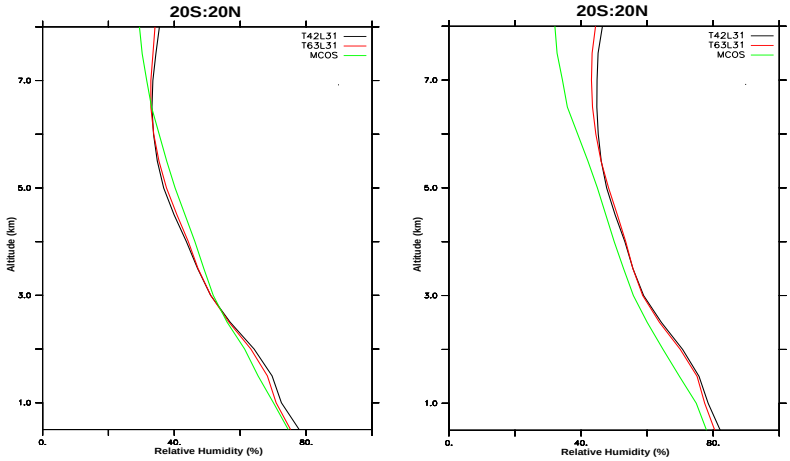

(a) Latitude range 20S:20N for DJF (b) Latitude range 20S:20N for JJA

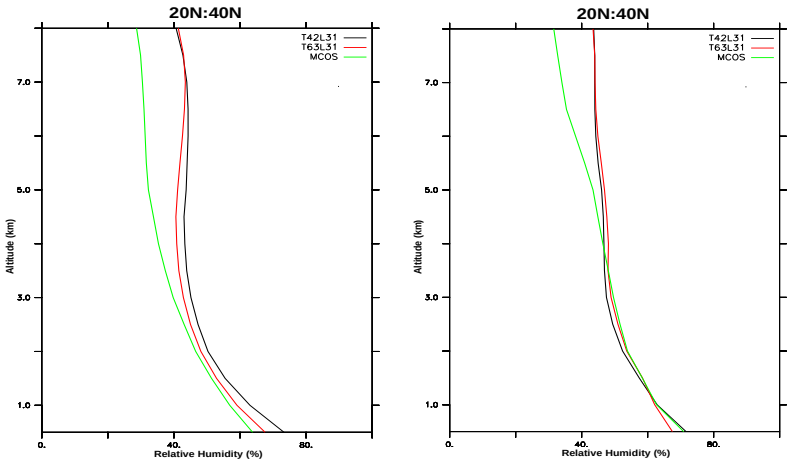

(c) Latitude range 20N:40N for DJF (d) Latitude range 20N:40N for JJA

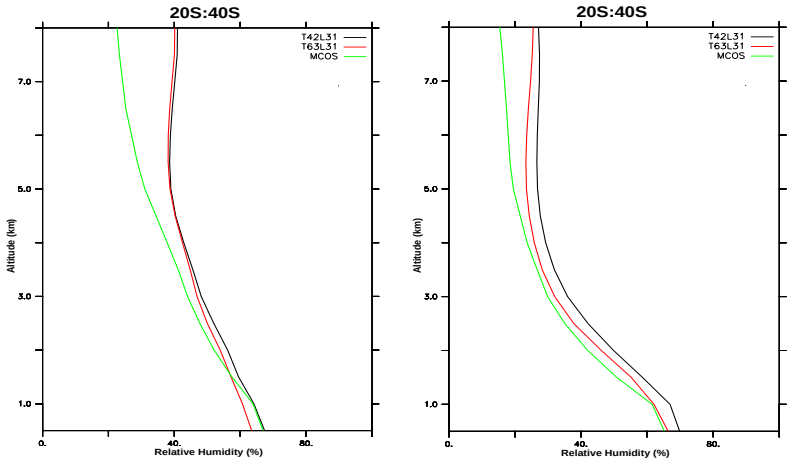

(e) Latitude range 20S:40S for DJF (f) Latitude range 20S:40S for JJA

Figure 3.18: Vertical profiles of specific humidity (in g/kg) for the latitude ranges: (a) 20S:20N DJF, (b)20S:20N JJA, (c) 20N:40N DJF, (d) 20N:40N DJF, (e) 20S:40S DJF, (f) 20S:40S JJA, (g) 40N:60N DJF, (h) 40N:60N JJA, (i) 40S:60S DJF, (j) 40S:60S JJA.

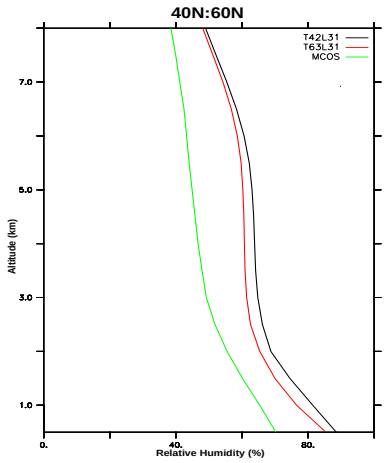

(g) Latitude range 40N:60N for DJF

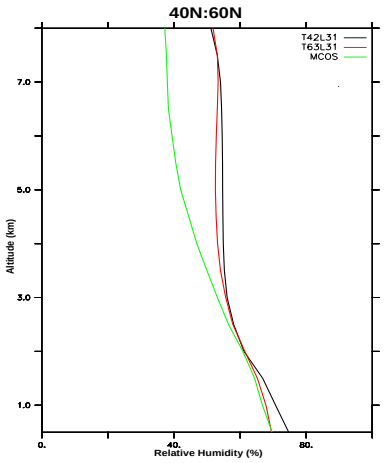

(h) Latitude range 40N:60N for JJA

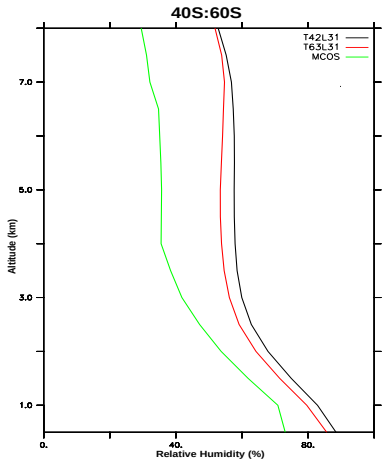

(i) Latitude range 40S:60S for DJF

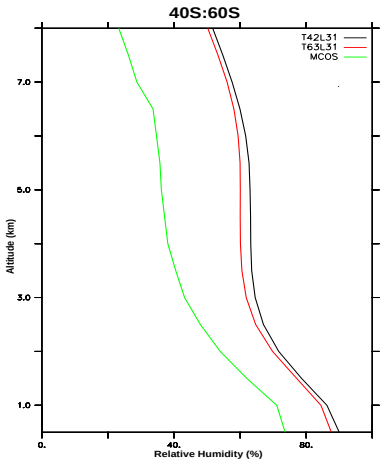

(j) Latitude range 40S:60S for JJA

Figure 3.18: Continued.

3.5 Summary and conclusions

Selected features of the EMAC hydrological cycle have been presented for both resolutions T42L31 and T63L31. The latter exhibits a stronger hydrological cycle. Most of the features we focused on, like water vapor columns and profiles agree quite well with observations in zonal means and seasonal averages. For the precipitation rates, relatively large errors are found over the tropical regions and high mountain chains. This is attributed to the convection

representation in the model and has been studied in detail by Tost et al. (2007).
The comparison of the model evapotranspiration with GSWP2 over land shows a clear overestimation over the tropical land masses. In the mean annual values, evapotranspiration correlates quite well with the total water vapor column (r=0.85). The correlation is lowest in JJA (r=0.6). This is visible in the geographic distributions of evapotranspiration and TWVC. The high model TWVCs, observed in JJA over Europe and eastern North America, are not correlated with high evapotranspiration rates. Similarly the low TWVC over Angola and eastern Brazil do not correspond to low evapotranspiration rates. This might be explained by an excess (lack) of moisture transport in these regions due to deficiencies in atmospheric circulation. Further, high evapotranspiration rates as in northern Amazon in DJF or in austral Africa in JJA (mostly vegetated areas) are not due to an excess in precipitation. This can be explained by the excess of soil moisture memory in these seasons which allow the vegetation to transpire although there is a lack of precipitation.
As mentioned above, where TWVC is strong, especially at the ITCZ, we find a high bias in model precipitation. High (low) moisture content of the atmosphere could lead in some specific regions to high (low) precipitation rates, but an overestimated precipitation can cause the TWVC to decrease. The first holds particularly for the ITCZ over land in DJF and JJA with both too high precipitation and TWVC and for Atlantic and eastern Pacific ITCZ with both too low rainfall and column humidity. Over the oceans, high TWVC is generally simulated well except over the ITCZ in DJF consistently with relatively low precipitation and with large short wave cloud forcing found by Wild et al. (2006) over the Southern Ocean in the same season. In JJA, again high model TWVC over oceans are correlated with low rainfall rates except over the West Pacific warm pool. This implies that the TWVC, even though overestimated in some regions might not reach the threshold to make substantial rainfall occur, but once this threshold is reached, as in the west Pacific and tropical land masses, precipitation might increase exponentially with increasing moisture. In fact, heavy precipitation regions are more consistent with major moisture convergence regions, indicating that the large-scale moisture convergence is the main source of water vapor supply for the rainfall in these regions. The changes in precipitation are probably mainly due to changes in water vapor transport and local evaporation changes may play only a minor role in the precipitation changes, especially over the ocean areas. This can only be assessed and understood through a complete analysis of the model water vapor transport.
The discrepancies, found in relative humidity comparisons, might explain some of these differences through the effects on cloudiness, although observational datasets for RH are all uncertain and have all advantages and disadvantages. Further comparisons to other radiosondes datasets like Durre et al. (2006) or satellite data like AIRS (The Atmospheric Infrared Sounder) on the Aqua satellite of the Earth Observing System (EOS), besides a careful evaluation of cloudiness, should help us to understand better the hydrological cycle.

Chapter 4

Impact of rainfall interception on surface exchanges and atmospheric chemistry

4.1 Introduction

Dry deposition and biogenic emissions of reactive trace gases and aerosols depend on land surface properties including biogeochemical and physical properties. The dry deposition flux of gases from the atmosphere to a receptor surface is governed by the concentration of the gas at a specific height and the dry deposition velocity, which in turn depends on the turbulent transport processes in the boundary layer through the aerodynamic resistance, and by the efficiency of the surface to capture and absorb gases through the surface resistance. The uptake by vegetation is a major sink for many trace gases such as SO_2 and O_3 and is controlled by turbulent transport and diffusion to the leaf or needle surface and the subsequent uptake by stomata, mesophilic tissue and the cuticle (Erisman and Van Pul, 1994; Ganzeveld and Lelieveld, 1995; Gut and et al., 2002). This uptake is affected by water covering the leaf or needle surface. The source of this surface water is dewfall or rainwater intercepted by the vegetation canopy, which subsequently evaporates, usually referred to as interception loss. The latter tends to be overestimated in the tropics by most current GCM land surface schemes (Lean and Warrilow, 1989; Dolman and Gregory, 1992; Eltahir and Bras, 1993a; Wang and Eltahir, 2000; Hahmann, 2003). For example, evaluation of the Amazon tropical forest energy partitioning using a single-column version of the chemistry-GCM ECHAM4 (Ganzeveld et al., 2002b) indicated a misrepresentation of the evapotranspiration through significant discrepancies between the modeled and observed sensible heat fluxes (20 versus 200 W/m^2) and the net radiation (450 versus 600 W/m^2) for tropical rainforest near Manaus, Brazil. This inadequacy has been partially attributed to the misrepresentation of the modeled convective rainfall interception,

more particularly the subgrid variability in convective rainfall interception, which results in an overestimation of the fraction of wet vegetation in the grid-cell (the so-called "wet skin fraction"). In addition, model evaluation has also revealed that ECHAM4 underestimates O_3 dry deposition in the tropical regions (Ganzeveld et al., 2002b; von Kuhlmann et al., 2003) most likely due to an overestimation of the wet skin fraction.

Neglecting the subgrid variability in convective rainfall and its interception in the tropics has been recognized to be a serious source of error in the parameterization of interception in GCMs (Shuttleworth and Dickinson, 1989; Dolman and Gregory, 1992; Eltahir and Bras, 1993a). A typical convective rain cell covers about 10^2-10^3 km^2 (Rodriguez-Iturbe and Eagleson, 1987) whereas a grid-cell in a GCM covers typically areas of more than 10^4 km^2. Considering convective rainfall uniformly falling over the entire grid-cell results in an increase of the amount of water retained and evaporated by the vegetation. This misrepresentation affects the partitioning between wet surface evaporation and dry vegetation transpiration as well as the partitioning of the net radiation between latent and sensible heat fluxes (Wang and Eltahir, 2000).

Here the impact of the spatial subgrid variability in convective rainfall interception on surface trace gases exchanges and global atmospheric chemistry is investigated using EMAC. This chapter examines the direct effects on dry deposition focusing on trace gases with contrasting solubilities, O_3 and HCOOH (formic acid) with a low and high solubility, respectively, to illustrate the potential impact of changes in the surface hydrology on insoluble and soluble gas exchanges. The indirect effects on the exchanges involving the sources and sinks of these and other trace gases like isoprene due to changes in meteorology are also included. The importance of linkages between the hydrological cycle and atmospheric chemistry focusing on this specific feature of rainfall interception is demonstrated and how the misrepresentation of rainfall interception in large-scale atmospheric chemistry models can influence surface exchanges and the atmospheric burden of important trace gases like ozone. Section 2 of Chapter 4 describes the model used in this study as well as the two performed experiments, one assuming the subgrid variability of the rainfall interception distribution and one assuming a uniform rainfall interception distribution. In Section 3 we present the results of these two experiments followed by a discussion in Section 4 and conclusions in Section 5.

4.2 Methodology

The overestimation of interception loss is due to the neglect of spatial variability in convective rainfall. We take a statistical approach to represent the subgrid variability of convective rainfall in order to allow for spatial precipitation variation and for the fact that the GCM grid is not fully covered by convective storms. According to Shuttleworth (1988), precipitation is assumed to fall over a fraction μ of the grid cell and the precipitation P_0 in the rain-covered part of the grid cell follows a negative exponential probability distribution, as shown in the following expression:

$$f(P) = \frac{\mu}{P} exp(\frac{-\mu P_0}{P}) \tag{4.1}$$

with P being the model grid-averaged precipitation rate. As a result, the grid-averaged throughfall T, which is the part of the grid rainfall that falls from the canopy to the ground during the wetting-up phase of the canopy, can be derived according to Dolman and Gregory (1992) as:

$$T = P(1 - \frac{C}{S}) exp(\frac{-\mu S}{P \delta t}) + P\frac{C}{S} \tag{4.2}$$

with C being the depth of water on the grid-cell or skin reservoir content, S the maximum amount of water that can be held by the skin reservoir and δt the model timestep. The skin reservoir represents the fraction of the grid square covered by water in bare-soil and vegetation. The choice of the parameter μ (i.e. the fraction of a grid cell where precipitation occurs) is recognized as an important factor affecting the model climatology (Wang and Eltahir, 2000). Pitman (1990) showed the sensitivity of the climate to the choice of μ. Hahmann (2003) recommended that μ should depend on the model resolution, region and season. In Eltahir and Bras (1993b) and Wang et al. (2005), the fraction μ is estimated as the ratio of the model-predicted rainfall intensity P_m to the conditional mean rainfall intensity P_o derived from high-resolution observational data, $\mu = P_m/P_o$, which varies temporally and spatially, but it is not clear on what grounds this assumption is warranted (Onof and Wheater, 1996). Wang et al. (2005) make use of high-resolution satellite rainfall observation in estimating μ and f(P). We use an estimate of the precipitable convective cloud cover over the grid-cell column as an estimation of μ (Crutzen and Lawrence, 2000) for convective rainfall and the value of 1 for large-scale rainfall. This estimation allows μ to vary not only with time and location, but also with the model resolution and introduces a more sound physical representation of the subgrid variability of convective precipitation in the tropics.
Two experiments, one labeled as BASE and one SUBGRID, are performed to evaluate the implications of rainfall interception subgrid variability for atmospheric chemistry. In the "BASE" experiment, the rainfall is uniformly intercepted over the grid-cell with an interception coefficient of 0.25 (see chapter 2) and limited by the capacity of the interception reservoir S. In the subgrid experiment, throughfall is calculated according to (4.2). The rain water on the leaves is intercepted by the vegetation (P-T) until its water holding capacity S is attained.

4.3 Results

4.3.1 Impact on the hydrological cycle

Annual mean values The comparison between the two simulations is presented in this section. Figure 4.1 shows the comparison between the BASE run and SUBGRID run for

interception loss, evapotranspiration, runoff, soil moisture and precipitation. The BASE yearly-averaged values and differences with the SUBGRID values are displayed. Most of the changes are found in the tropics and the BASE case overestimates the interception loss in the Amazon, Central Africa, Europe, southeastern Asia and eastern US. The decrease in interception loss is due the decrease in the wet skin fraction (Figure 4.2) determined by less rain intercepted by the vegetation and more throughfall falling to the ground.
The decrease in interception loss causes the evapotranspiration to decrease in most of the vegetated areas in the tropics but not in the Amazon and Congo rainforest. Despite the large decrease in evaporation from vegetation, the evapotranspiration remains almost the same in the Amazon rainforest.

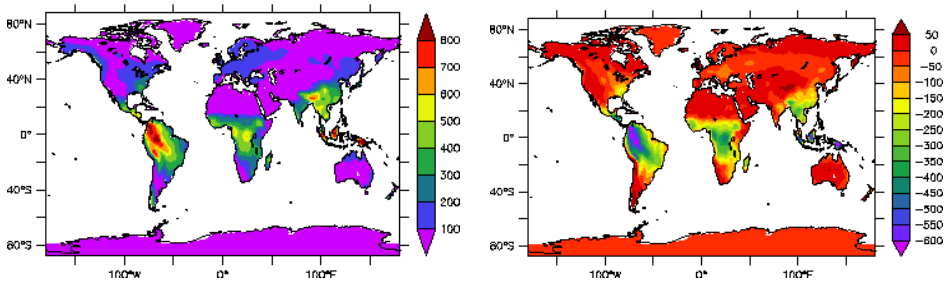

(k) Interception loss BASE (mm/d) (l) SUBGRID - BASE

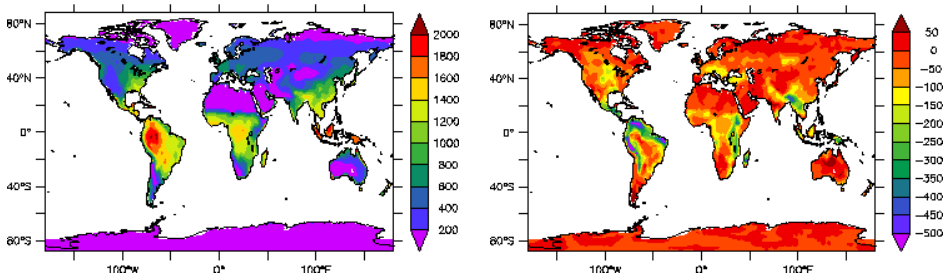

(m) Evapotranspiration BASE (mm/d) (n) SUBGRID - BASE

Figure 4.1: Comparison of the global distributions of (a) interception loss, (c) evapotranspiration, (e) runoff, (g) soil moisture and (i) precipitation between the BASE case and the SUBGRID case. The yearly accumulated absolute values for interception loss, evapotranspiration and precipitation and the yearly averaged absolute values for soil moisture are presented in the left panels and the difference between SUBGRID and BASE in the right panels.

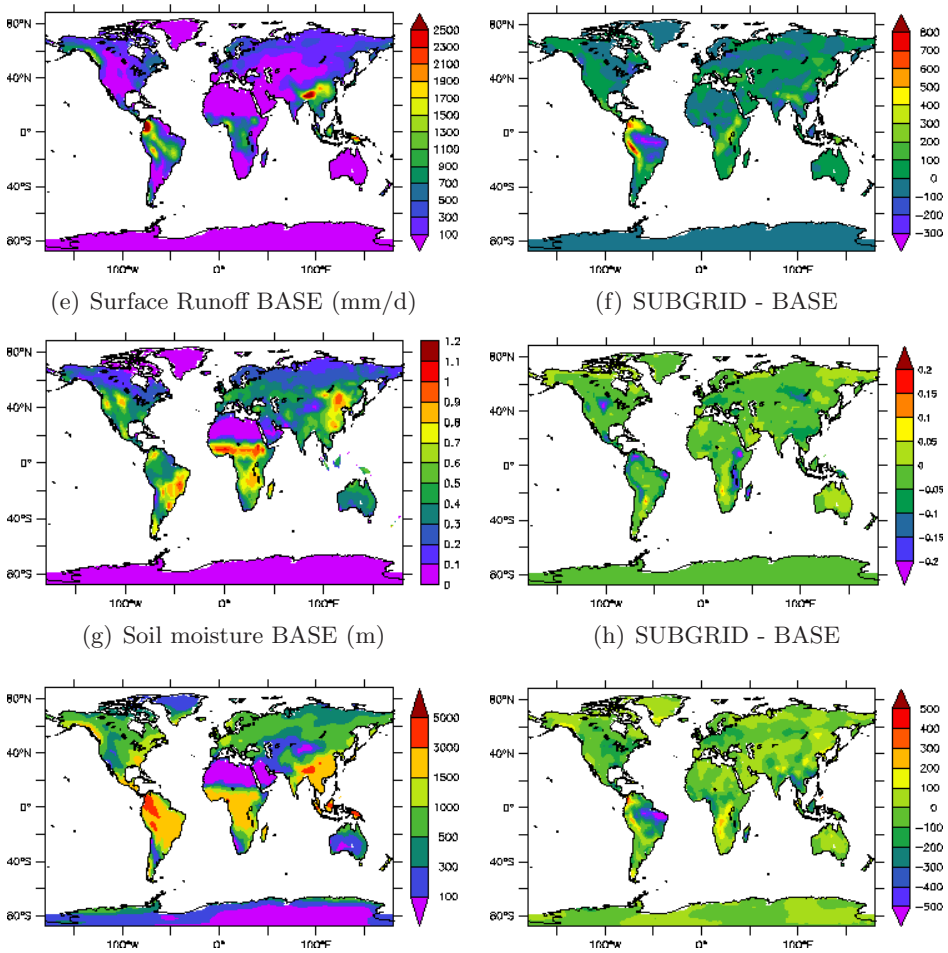

(e) Surface Runoff BASE (mm/d)

(f) SUBGRID - BASE

(g) Soil moisture BASE (m)

(h) SUBGRID - BASE

(i) Precipitation BASE (m)

(j) SUBGRID - BASE

Figure 4.1: Continued.

Moreover the surface runoff (Figure 4.1f) decreases in this region unlike the regions covered by savannah and grass type of vegetation (over Colombia and the Andes region). The surface runoff is calculated from a scheme which takes into account the heterogeneous distribution of field capacities within a grid-cell (Dümenil and Todini, 1992; Hagemann and Dümenil Gates, 2003) and topography variations influence the distribution of saturated subgrid areas within the model gridbox. This explains the high surface runoff rates over regions with high topographical variations like the Andes and Himalaya regions. In these areas the excess of throughfall, generated by the new parameterization in SUBGRID case, feeds the surface runoff instead of the soil moisture (through infiltration) which increases the runoff rates over these regions. Since

the wet skin fraction decreases, the vegetation transpires freely depleting the soil moisture and causes a negative feedback on transpiration and thus evapotranspiration.

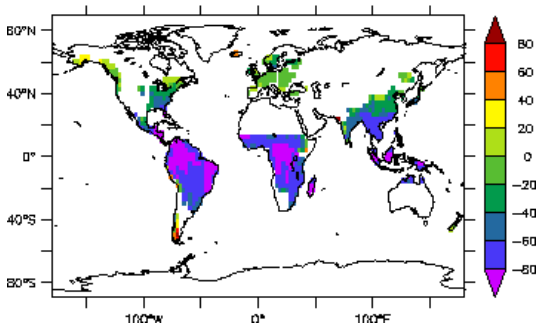

Figure 4.2: Relative change ($\frac{SUBGRID-BASE}{BASE}$) in the wet skin fraction (%)

In other vegetated regions like southern Europe or eastern US characterized by less biomass (lower leaf are index and vegetation ratio) and less convective activity the decrease in evapotranspiration is attributed to the vegetation characteristics including the maximum water holding capacity in the canopy (S) and the field capacity (the maximum water held by the soil after drainage).
The diagram shown in Figure 4.3 summarizes the mechanism by which the evapotranspiration decreases dramatically over mountains and to a lesser extent over other vegetated areas than rainforest. Over rainforest, as in the Amazon or central Africa or Indonesia, the excess of water is simply infiltrated into the soil and the vegetation can use this additional soil moisture to transpire. The dramatic decrease in interception loss is therefore compensated by transpiration. This is consistent with the findings of Dolman and Gregory (1992) using a one dimensional coupled land-atmosphere model in the Amazon, and Wang and Eltahir (2000) using a zonally symmetric biosphere-atmosphere model (ZonalBAM) applied to West Africa. Both studies focus on a rainforest region or a comparison of vegetation types (rainforest versus grassland) as in the latter study.
The comparison of precipitation between the two experiments (Figure 4.2j) shows a decrease of up to 500 mm/year over eastern Brazil and southeastern Asia and approximately the same increase over the northern part of the Andes. This amount of precipitation represents less than 15% of the yearly-averaged total precipitation over these regions. As a direct result of the changes in precipitation the surface runoff over eastern Brazil and the Amazon is lower in the SUBGRID case but contributes to an excess in the runoff in the western part of South America. Since the evapotranspiration in the Amazon remains almost the same between the two cases, the slight reduction in precipitation indicate a decrease in moisture convergence that can only be explained by changes in the large scale circulation patterns.

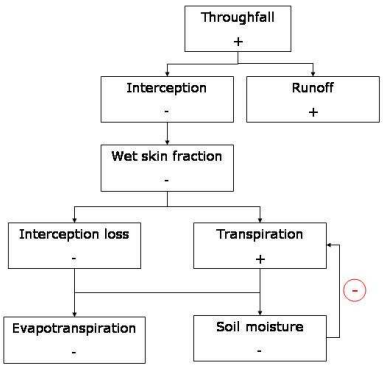

Figure 4.3: Diagram explaining the effects of the changes in rainfall interception on the hydrological cycle.

Seasonal cycle

To illustrate the model response, we focus on the following on four regions (Figure 4.4): 70W:55W-14S:2S (hereafter R1) which represents the Amazon Basin, 78W:55W-0:10N (hereafter R2) in South America, 44N:50N-0:25N in Europe (hereafter R3) which represents partly the Danube Basin and 92E:110E-10N:25N which covers part of southeastern Asia (hereafter R4). The four regions have different climates and different vegetation (density and type), but all are sensitive to a decrease in interception loss and the consequent decrease in evapotranspiration. Figure 4.5 shows the seasonal cycle of evapotranspiration and soil moisture for the four regions. Although all regions show a decrease in the annual mean evapotranspiration, the seasonal cycle is not affected in the same manner. In the rainy season, the evapotranspiration is slightly affected in all regions except R2, whereas in the dry season the evapotranspiration is strongly decreased everywhere and the soil moisture is depleted. The effects on precipitation are negligible in all regions, except in summer in R3, where we observe a strong coupling between soil moisture and precipitation. This feature of the land-atmosphere interaction has been observed in a multimodel experiment, including ECHAM5 (Koster et al., 2004).
To understand the hydrological processes involved, we emphasize two regions with contrasting hydrological regimes: an evapotranspiration regime where the excess of throughfall feeds the soil reservoir enabling a higher transpiration and a runoff regime characterized by the recycling of throughfall into surface runoff. As shown in the previous section, the Amazon basin (R1) illustrates the evapotranspiration regime and the region between the Amazon Basin and the Caribic sea (R2) favors a runoff regime. Both regions have strong convective activity but differ in the vegetation type and their related hydrological properties (field capacity, S, the maximum water held by the leaves), and topography. The differences between the two regimes

can be observed in the comparison of the seasonal cycle in the two regions (Fig.4.5). The rainy/dry season in R1 corresponds clearly to a maximum/minimum in soil moisture and thus evapotranspiration, whereas in R2 a time lag exists between precipitation and the soil moisture and the evapotranspiration is at its maximum in the dry season (with a peak in August). Although not apparent in annual mean figure, the evapotranspiration in R1 and R4 decreases slightly in the SUBGRID case, as the interception loss decreases. In R2, as explained above the reduced transpiration causes a strong decrease in the total evapotranspiration, which in turn explains the associated decrease in soil moisture (Fig. 4.3). Similarly for R3 and despite the decrease in precipitation, the runoff is increasing in both seasons due to the same runoff regime, whereas the evapotranspiration is affected only in summer due to the strong decrease in soil moisture.

The response of precipitation to the changes in rainfall interception appears to be less robust than other hydrological parameters. The rainfall interception and soil moisture exert a strong control on evapotranspiration and runoff, but the connection from rainfall interception and soil moisture to precipitation is rather tenuous, involving different levels of impacts of heat and moisture fluxes, and is modulated by the nature of the atmospheric boundary layer and general circulation. Further, the land surface changes may increase or decrease the moisture convergence to and from some specific regions, depending on the relative changes in latent and sensible heat flux, and the large circulation (e.g. Shukla and Mintz (1982); Dirmeyer and Shukla (1994); Wang and Eltahir (2000)). Due to the complexity of the feedbacks involved and the small effect of our experiment on rainfall in most of the regions considered, the precipitation feedback is neglected in our analysis.

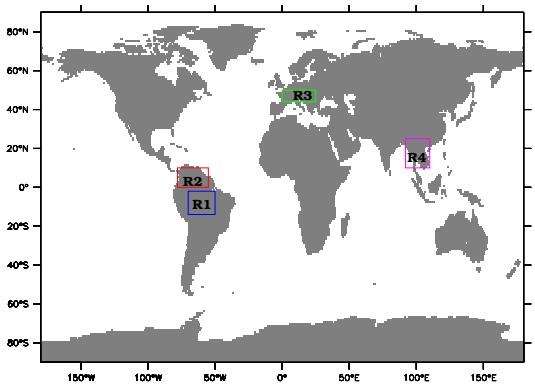

Figure 4.4: The selected focus four regions: R1 = 70W:55W-14S:2S, R2 = 78W:55W-0:10N, R3 = 44N:50N-0:25N, R4 = 92E:110E-10N:25N.

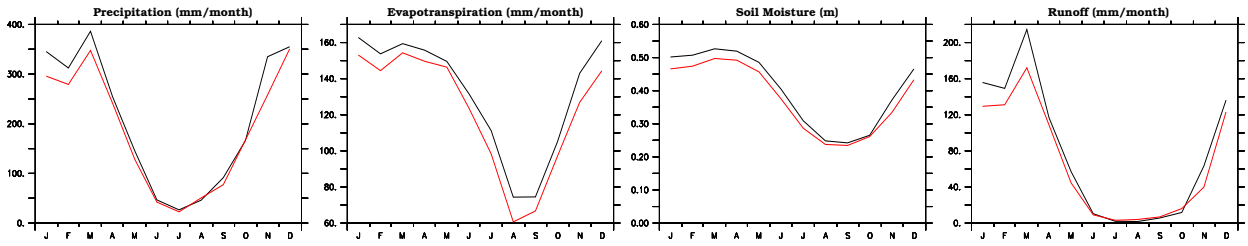

(a) Region 1

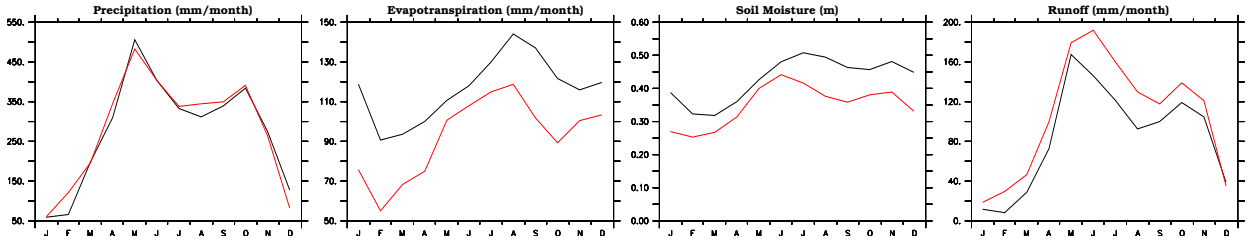

(b) Region 2

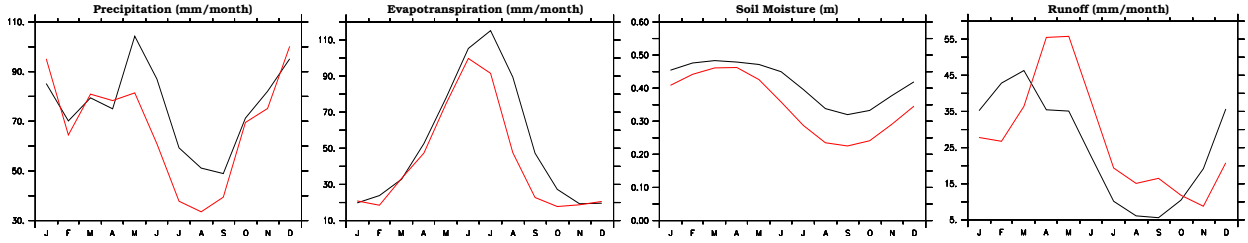

(c) Region 3

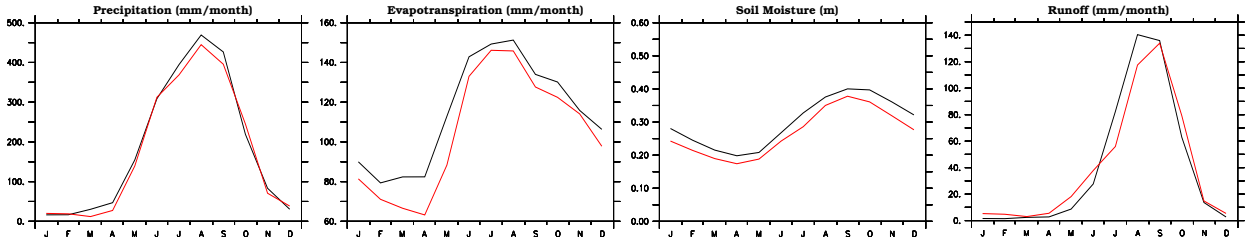

(d) Region 4

Figure 4.5: Seasonal cycle of precipitation (mm/month), evapotranspiration (in mm/month), soil moisture (in m) and runoff (mm/month) from the left to the right respectively for the 4 regions (a) R1, (b) R2, (c) R3 and (d) R4. The black represents the BASE case and the red, the SUBGRID case.

4.3.2 Impact on micro-meteorology and transport

The changes in the water cycle greatly affect the energy balance and propagate further into the atmosphere. The coupling between the soil moisture and surface temperature causes the latter to increase by about 2K in the regions where the soil water has been depleted: central and south America, East Africa, southern China, Indonesia and southeastern Europe. The higher surface temperature (Fig. 4.6b) tends to increase the sensible heat flux (Fig. 6d) causing a warming effect. As a result more energy is transferred to the boundary layer causing more instability and turbulence. This might be the cause of the convection intensification over the Andes.

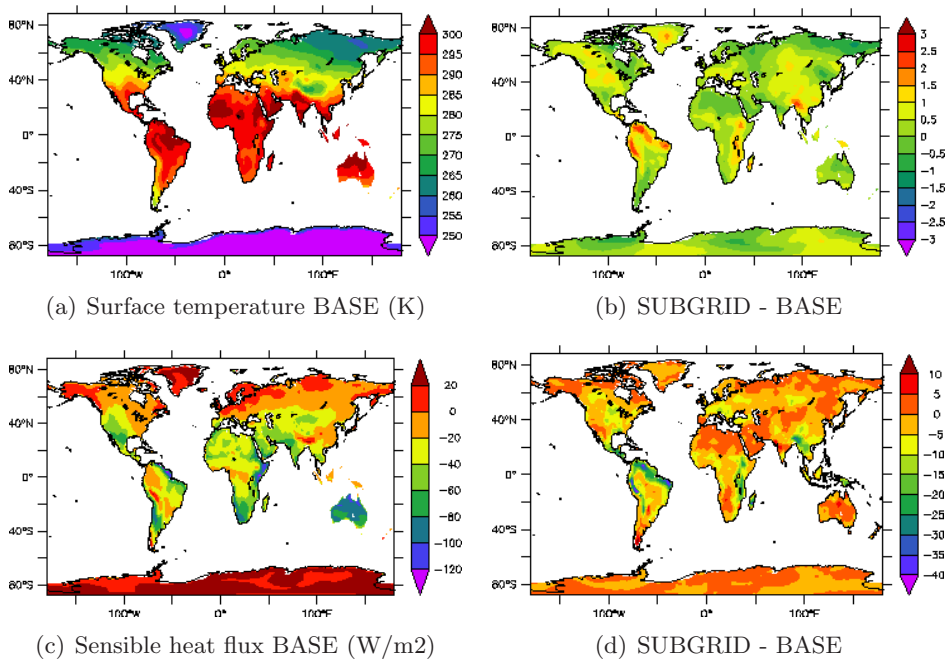

(a) Surface temperature BASE (K)

(b) SUBGRID - BASE

(c) Sensible heat flux BASE (W/m2)

(d) SUBGRID - BASE

Figure 4.6: Comparison of the global distributions of the BASE case (left panels) and the difference SUBGRID minus BASE for: sensible heat flux (W/m^2), surface temperature (K).

The analysis of the energy budget for the four regions considered above is presented in Table 4.1; note that the ground heat flux is negligible. The decrease in the latent heat flux for R1 and R4 remains very low, as shown above, but is compensated by a higher relative increase in the sensible heat flux. Over R2 and R3, the relative change in both latent and sensible heat fluxes is large, reaching up to +136% for R3. The changes in the net thermal surface radiation are due to the increased surface temperature influencing the outgoing longwave radiation. Moreover, a small relative change in the net solar surface radiation is observed over all regions (less than

5%), which imply a small change in cloudiness. The changes in water vapor column over the four regions are remarkably small (not shown), less than 10% in all of the regions, reflecting the low direct impact of land surface evapotranspiration and the important role of moisture convergence in the water vapor column (see Chapter 3). As a consequence of the enhancement in sensible heat flux, the depth of the boundary layer (PBLH, see Table 4.2) is greater in all seasons, with a stronger enhancement in the dry season for all regions. This indicates the strong effect of soil moisture on the energy budget in this season and its consequences for the convective and turbulent transport of chemical species.

Table 4.1: Energy budget for the regions R1, R2, R3 and R4.

R1			
	BASE	SUBGRID	Relative change (%)
Latent Heat Flux (W m^{-2})	125.3	116.1	-7
Sensible Heat Flux (W m^{-2})	29.2	37.11	27
Net solar surface radiation flux (W m^{-2})	202.1	203.1	0.5
Net thermal surface radiation flux (W m^{-2})	-47.3	-49.8	5
R2			
Latent Heat Flux (W m^{-2})	110.9	88.0	-20
Sensible Heat Flux (W m^{-2})	38.9	55.3	42
Net solar surface radiation flux (W m^{-2})	204.4	201.9	1
Net thermal surface radiation flux (W m^{-2})	-48.0	-52.1	8
R3			
Latent Heat Flux (W m^{-2})	50.08	40.8	-18
Sensible Heat Flux (W m^{-2})	6.4	15.3	136
Net solar surface radiation flux (W m^{-2})	99.7	105.1	5
Net thermal surface radiation flux (W m^{-2})	-45.27	-50.8	12
R4			
Latent Heat Flux (W m^{-2})	109	99.6	-8
Sensible Heat Flux (W m^{-2})	26.2	33.8	28
Net solar surface radiation flux (W m^{-2})	202.7	203.2	0.2
Net thermal surface radiation flux (W m^{-2})	-54.7	-57.4	4

To assess the impact of vertical transport and advection, the effect of rainfall interception on artificial tracers similar to Radon 222 is introduced: Rn_{01}, Rn_{10} and Rn_{100} emitted over land with a constant flux of 1 atom/(cm^2.s), and a lifetime of one day, ten days and a hundred days respectively, which correspond to the lifetimes of a range of trace gases. Since they are not chemically reactive, such tracers are suitable for the study of vertical and horizontal transport processes. The effects of the changes in PBLH are investigated through the comparison of

profiles of Rn_{01} in the lower troposphere for the months January and August (Figure 4.7), and the region R2 is chosen due to its largest relative differences in PBLH in both months. Although the diagnosed averaged maximum daily PBLH has increased substantially in this region in those months (36% for January and 27% for August), the effects on the tracer Rn_{01} are rather small at the surface, but a relatively larger enhancement is seen in the concentrations in the upper part of the boundary layer. This can be attributed to the deeper PBLH, but also to a more effective convective updraft. Similarly, the Rn_{10} tracer shows the same relative increase in the mid-troposphere in the dry season (January), and a slight increase in the upper troposphere in the rainy season, which are attributed to convective transport. On the other hand, the comparison of the horizontal distribution of Rn_{100} at the surface layer between the two runs shows hardly any changes, implying no major changes in the large scale circulation patterns.

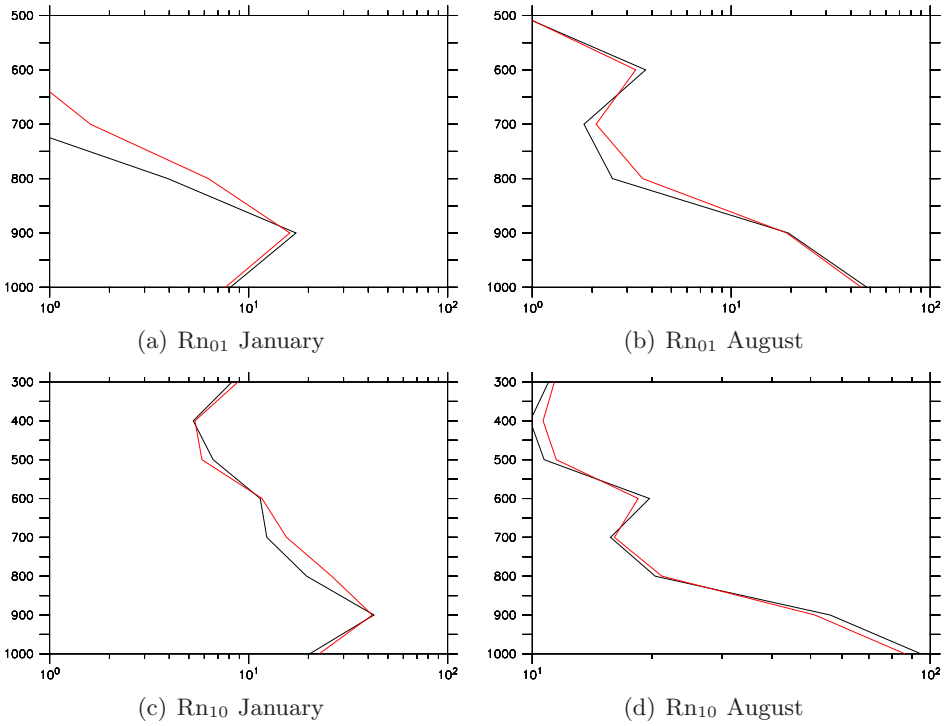

(a) Rn_{01} January (b) Rn_{01} August

(c) Rn_{10} January (d) Rn_{10} August

Figure 4.7: Vertical profiles of Rn_{01} (10^{-21} mol/mol) for the region R2 for (a) January and (b) August. The same for Rn_{10}: (c) January and (d) August.

Table 4.2: Maximum daily planetary boundary height for R1, R2, R3 and R4

	R1		
	PBLH BASE (m)	PBLH SUBGRID (m)	Relative change (%)
January	823	974	16.8
August	1876	2059	13.9
	R2		
January	1279	1752	36.7
August	994	1266	27
	R3		
January	598	599	5.2
August	1188	1616	37
	R4		
January	852	971	14.0
August	695	739	4.8

4.3.3 Impact on trace-gas exchanges: dry deposition and emissions

Emissions

The changes in rainfall interception result in a slight relative increase in soil-biogenic nitric oxide (NO) annual mean emissions of less than 5% over most of the regions affected by the change in rainfall interception, except over northern Colombia, eastern Brazil and the east-African rift region, where it reaches a relative increase of 20% (Figure 4.8). The relative differences in all seasons for R1, R2, R3 and R4 (Table 4.3) confirm the low sensitivity of NO emissions to the change in rainfall interception. The soil NO emissions, based on the Yienger and Levy algorithm (1995), are calculated as a function of surface temperature for two soil states: wet and dry. A threshold of 0.1 m for the soil moisture is chosen to distinguish between a dry and wet soil. For all the regions mentioned, the soil moisture is mostly above the threshold (see Fig. 4.5). In these conditions, the role of pulsing in those regions is not expected to play an important role. Therefore the changes reflect only the sensitivity to soil temperature. For tropical rainforest, the emission class applied does not account for the effect of temperature and resembles the emission for wet soils. Similarly, the isoprene (ISOP) emissions, calculated according to Guenther et al. (1995), increase with surface temperature and net surface solar radiation. Since the latter hardly changed in SUBGRID, the change in ISOP emissions depends solely on surface temperature, resulting in a yearly-averaged emission increase of up to 40% in the same regions where surface temperature has shown significant increases. The seasonal relative change shows the maximum sensitivity for R3 for all seasons, due to the low absolute isoprene emission fluxes in this region.

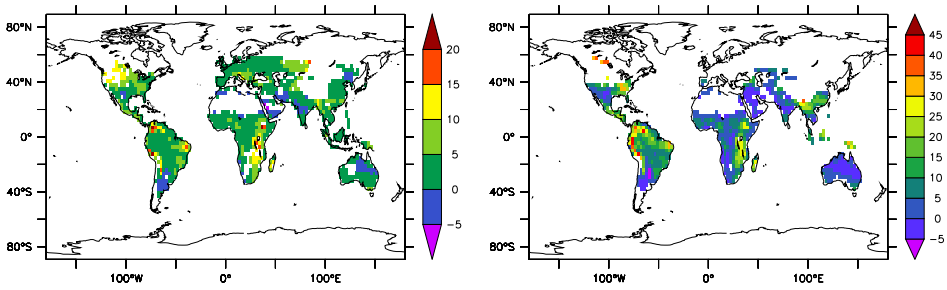

(a) NO (b) ISOP

Figure 4.8: Relative difference ($\frac{SUBGRID-BASE}{BASE}$) (in %) for the NO and isoprene annual mean emissions fluxes.

Table 4.3: Relative differences ($\frac{SUBGRID-BASE}{BASE}$) of NO and isoprene emissions in % for R1, R2, R3 and R4

	NO	ISOP
R1		
DJF	2	15
MAM	1	9
JJA	2	8
SON	2	12
R2		
DJF	2	17
MAM	2	11
JJA	2	14
SON	3	14
R3		
DJF	-5	-3
MAM	2	30
JJA	5	38
SON	7	27
R4		
DJF	4	13
MAM	3	8
JJA	2	11
SON	4	14

Dry deposition

Annual mean The effects of the the subgrid parametrization on the dry deposition of O_3 and HCOOH, with a low and high solubility, respectively, are assessed in this subsection. Figure 4.9 shows the relative change in dry deposition velocity for O_3 and HCOOH between the BASE and SUBGRID simulation experiments. The uptake of O_3 by vegetation is solely determined by the stomatal resistance, when the vegetation is not covered by rainwater from interception. The strong decrease in the wet skin fraction observed in Figure 4.1 causes the O_3 dry deposition velocity (V_{dO_3}) to increase up to +40 % over densely vegetated areas in the tropical rainforest in the Amazon, central Africa and south east Asia, and over forest zones in Europe and eastern North America where the rainfall interception represents an important hydrological process. However this increase is restricted to regions where the interception loss has been compensated by transpiration and the soil moisture has not been affected (type R1). In regions characterized by a runoff regime (type R2), soil moisture has been depleted by transpiration, resulting in an enhancement of the stomatal resistance. The uptake by the leaves is thus considerably reduced. The water covering the leaves prevents the dependency of the dry deposition velocity on the stomatal resistance in this case. The different levels of dependency are summarized in the flowchart in Figure 4.3. This explains the large decrease (up to -40 %) in V_{dO_3} over northeastern South America, the East African rift region and to a lesser extent southeast Europe. HCOOH, unlike O_3, is mainly affected by changes in surface wetness. The HCOOH dry deposition velocity (V_{dHCOOH}) decreases up to 50% in all regions due to the accumulated effect of the decrease in wet skin fraction and stomatal conductance.

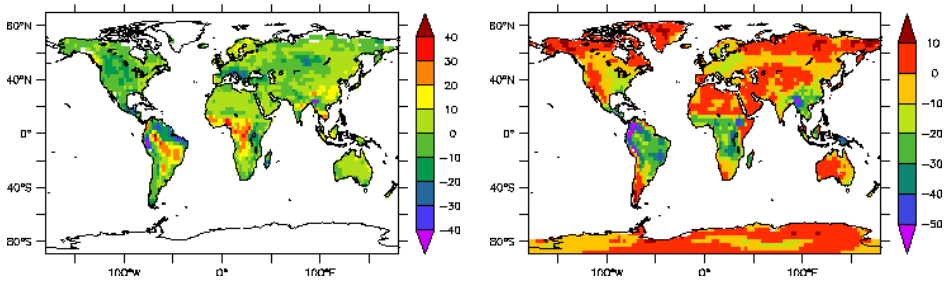

(a) O_3 (b) HCOOH

Figure 4.9: Relative change ($\frac{SUBGRID-BASE}{BASE}$) in the global distributions of the dry deposition velocity (%) for: (a) O_3, (b) HCOOH

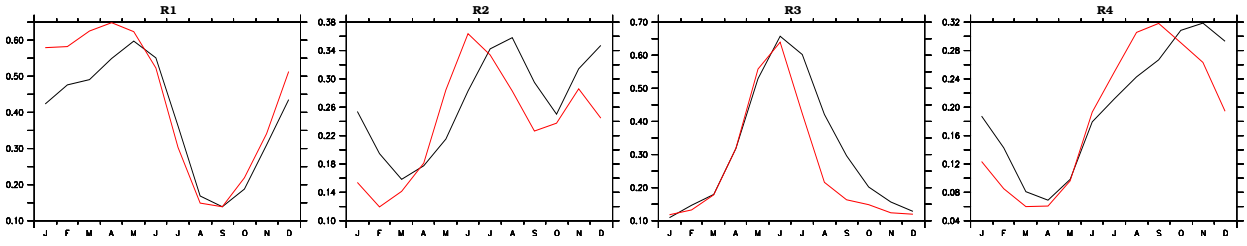

(a) O_3 dry depostioon velocity

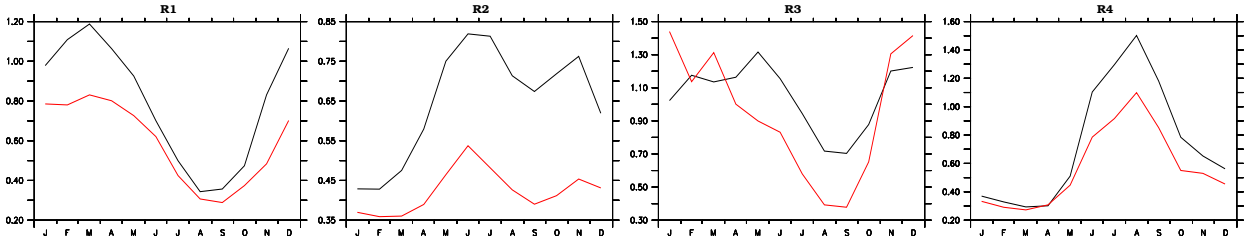

(b) HCOOH dry deposition velocity

Figure 4.10: Seasonal cycle of (a) O_3 and (b) HCOOH dry deposition velocity (cm/s) for the regions R1, R2, R3, and R4 (from the left to the right)

Seasonal cycle The analysis of the seasonal cycle shows the interplay between the roles of the wet skin fraction and the soil moisture in the modulation of dry deposition velocities of O_3 and HCOOH (Fig. 4.10). V_{dO_3} has a maximum in the rainy season over the Amazon (R1), which makes it more dependent on the wet skin fraction rather than soil moisture. This explains the increase observed between January and May due to the decrease in wet skin fraction in SUBGRID. In the following months, when the dry season starts, the velocity becomes dependent only on the stomatal aperture because of the absence of precipitation. Over R2, the interplay is more complex: due to a decrease in soil moisture in all seasons causing more water stress, V_{dO_3} decreases in the dry season but the tendency is inverted as soon as the wet season reaches its peak in May implying a more effective role of the wet skin fraction. For R3, the effect in the European rainy season (from January to June) is negligible due to low changes in the wet skin fraction in this period of the year, due itself to the dominance of large scale precipitation rather than convective precipitation. In the warm season (June to September), when convection is more prevalent, V_{dO_3} undergoes the effect of the reduction of soil moisture and stomatal closure. Like for R1, R4 with its tropical forest shows the same evolution for V_{dO_3} (though offset by 6 months) with a reduction in a dry season and a relative enhancement in the rainy season.
In contrast, V_{dHCOOH} has decreased in all regions by the combined impact of both leaf wetness and soil moisture depletions in all seasons: less water covering the leaves leads to lower uptake by the stomata and the reduced soil moisture, caused by the feedback described above, exacerbates

the first effect by stomata closure due to water stress. As for O_3, the uptake of NO and NO_2 by vegetation is controlled by the stomatal conductance, and is limited into the aqueous-phase, which makes the effects of the changes in the wet skin fraction similar to O_3.
Table 4.4 summarizes the relative differences in dry deposition velocities and fluxes between the two runs for the four regions and for O_3, NO, NO_2 and HCOOH. In general, the changes in deposition fluxes reflect the changes in dry deposition velocities for all species, except for HCOOH. Both generally have the same sign reflecting the same seasonal cycle, but show differences in intensity reflecting the changes in the surface layer concentrations of the respective trace gases.

Table 4.4: Relative differences ($\frac{SUBGRID-BASE}{BASE}$) of dry deposition velocity and flux (in parentheses) in % for major trace gases and for R1, R2, R3 and R4.

	R1			
	O_3	NO	NO_2	HCOOH
DJF	29.3(16.1)	33.4 (24.7)	32.7 (33.0)	-25.4 (3.3)
MAM	8.3(2.6)	9.8 (2.3)	9.6 (5.4)	-20.7(-1.7)
JJA	-11.1(-16.0)	-10.5(-7.8)	-10.4 (-9.4)	-17.5(-9.1)
SON	15.6(6.6)	20.1 (12.0)	19.2 (17.1)	-33.6(-5.0)
	R2			
DJF	-31.6(-29.6)	-40.9(-48.3)	-32.2(-30.9)	-18.2(-8.3)
MAM	22.7(3.5)	39.8(38.6)	31.8(31.5)	-35.2(-8.3)
JJA	-15.3(-4.1)	-7.9(-9.4)	-11.9(0.03)	-41.0(-14.2)
SON	-15.7(-9.2)	-11.1(-8.7)	-13.1(-8.6)	-38.2(-14.2)
	R3			
DJF	-1.4(-5.07)	-3.19(-2.1)	-4.1(-0.5)	16.6(5.9)
MAM	0.76(5.8)	2.1(0.64)	1.7(4.2)	-24.8(-5.9)
JJA	-39.1(-32.3)	-47.7(-43.0)	-39.9(-28.8)	-42.9(-19.2)
SON	-19.4(-19.7)	-43.5(-33.7)	-21.6(-13.0)	2.1(-0.3)
	R4			
DJF	-18.1(-10.5)	-30.4(-25.0)	-20.5(-9.1)	-4.0(-2.5)
MAM	-5.1(-7.7)	-9.8(-18.0)	-3.3(-8.9)	-16.8(-13.5)
JJA	28.8(24.7)	38.3(30.5)	36.6(37.1)	-27.7(-9.1)
SON	-8.3(-4.8)	-8.3(-5.4)	-8.1(-3.6)	-16.2(-2.9)

4.3.4 Impact on trace gases burdens

The relative differences in the surface layer mixing ratios of NO_x, isoprene, HCOOH, O_3 and OH between SUBGRID and BASE are shown in Table 4.5 for the four regions studied above. Our purpose is to show the direct impacts of the changes in surface exchanges on the atmospheric burden of key trace gases, therefore the chemical production/loss pathways of these chemical species will not be focused on in this study.

Table 4.5: Relative differences ($\frac{SUBGRID-BASE}{BASE}$) (in %) for O_3, NO_x, OH, isoprene and HCOOH for the four regions R1, R2, R3 and R4

		R1			
	O_3	NO_x	OH	ISOP	HCOOH
DJF	-9	-6	-34	13	37
MAM	1	-3	-14	7	17
JJA	1	-0.1	-20	5	7
SON	-6	-1	-23	19	27
		R2			
DJF	-1	-7	-9	18	13
MAM	-11	-4	-9	28	50
JJA	5	-3	-6	14	53
SON	6	-1	-4	17	43
		R3			
DJF	-1	2	1	7	-6
MAM	4	-1	-2	26	24
JJA	18	4	-25	30	26
SON	0.6	7	-8	36	12
		R4			
DJF	6.3	-1	-2	3	-4
MAM	1.0	-9.2	-5.4	1.0	-5.5
JJA	-2.8	-3.9	-3.9	15.2	32.5
SON	0.6	0.3	-1.0	15.7	22.1

There is a significant relative increase in the surface layer concentrations of HCOOH in nearly all seasons and regions explained by the significant reduction in the dry deposition velocity. This causes the changes in the dry deposition flux to be of less intensity than for the dry deposition velocity. The accumulation of HCOOH in the surface layer might be also attributed to a less efficient chemical sink through the reaction with OH, since OH concentrations are reduced in all regions and most dramatically in the Amazon region (R1). The isoprene concentrations are

relatively enhanced systematically in all four regions due to the enhanced isoprene emissions. The strongest effect is observed over the Alps region R3, reaching up to 36% increase in SON. As a direct consequence of the enhancement in isoprene concentrations, OH is reduced significantly in the tropical rainforest over the Amazon, reaching up to -34% in DJF, but does not exceed a 10% reduction in the other regions. In these regions isoprene is less abundant, so that the absolute change in isoprene concentrations is much smaller than over the Amazon. This implies that the change in OH loss will be also much smaller. Although NO_2 dry deposition fluxes (the NO dry deposition being negligible) have changed significantly due to changes in rainfall interception, the relative changes in NO_x concentrations are rather low (less than 10% reduction) for all regions. The decrease in OH in all regions reduces NO_2 conversion to HNO_3, combined with the change in the PBL height and contributes to an accumulation of NO_2 which increases O_3 formation. In effect the large relative increase/decrease in the O_3 dry deposition velocity and flux affects hardly the surface layer concentrations. The concentrations remain mainly unchanged in all regions and seasons with a relative difference not exceeding the 10 %, except in summer for the Alps region (18% increase) and spring in R2 (11 % decrease). The chemical production/loss pathways can not be assessed precisely without the complete budgeting tools necessary to quantify the tendencies due to each chemical reaction contributing to the production or loss of O_3.

4.3.5 Robustness of the results

As a means to establish the significance of the impact of rainfall interception, we estimate the noise in our results. This is derived by calculating the standard error of a set of values of a parameter for all combinations involving only consecutive years of simulation. The noise is calculated then for the 4 regions considered in this study and for annual precipitation and O_3 dry deposition velocity, as two main factors affected by rainfall interception, contrasting by their robustness.
For 1 year, the noise is calculated for precipitation P as follows:

$$N_1 = \frac{1}{6}\sqrt{\sum_{i=1}^{6}(X_{1i} - Av_{1err})} \tag{4.3}$$

with $X_{1i} = P_{SUBGRID} - P_{BASE}$ and the average error $Av_{1err} = \frac{1}{6}\sum_{i=1}^{6} X_{1i}$ The years from 1992 to 1997 are numbered from 1 to 6.
For 2 years, the noise is:

$$N_2 = \frac{1}{6}\sqrt{\sum_{i=1}^{6}(X_{2i} - Av_{2err})} \tag{4.4}$$

with $X_{2i} = X_j - X_k$ with j and k taken for consecutive years only and $Av_{2err} = \frac{1}{6}\sum_{i=1}^{6} X_{2i}$

The same operation is repeated for 3, 4, and 5 years. The noise is then compared to the signal, which is the average error for each year:

$$R = 100 * \frac{noise}{signal} \tag{4.5}$$

In Table 4.6, the ratio R is calculated for 1 to 5 years of simulation. R remains relatively high for precipitation for the four regions affected by the changes in rainfall interception. A strong decrease is observed from year to year, reaching 9% for R1 as minimum ratio and 34% for R2 as maximum. The large variability of R is maximum for R2 (between 167% and 34%) and R4 (between 246% and 14%) suggests that interannual variability within the climate model is important for these regions. The land surface state (rainfall interception, here) exerts an indirect control on precipitation. The connection from the rainfall interception to precipitation is rather tenuous and depends on several factors, such as both surface heat and moisture fluxes, the boundary layer characteristics and the general circulation. The ratio R in O_3 dry deposition velocity is varying between 75% for R1 after 1 year of simulation and 9% for after 5 years of simulation. This suggests less variability of R and more robustness in the results related to this parameter than in precipitation. The O_3 dry deposition velocity is affected by the indirect changes in the net surface radiation and soil moisture (through the regulation of the stomatal conductance) and the direct changes in wet skin fraction.

Table 4.6: The ratio R calculated for precipitation and O_3 dry deposition velocity for the four regions R1, R2, R3 and R4

Precipitation					
	1 year	2 years	3years	4 years	5 years
R1	83.9	59.8	37.0	18.6	9.6
R2	167.9	107.6	68.8	49.0	34.9
R3	113.4	69.7	55.3	35.9	23.7
R4	246.7	137.2	80.7	45.5	14.1
O_3 dry deposition velocity					
	1 year	2 years	3 years	4 years	5 years
R1	68.6	53.4	37.4	19.8	9.6
R2	59.6	35.3	20.8	14.4	11.7
R3	47.6	30.2	15.5	5.9	5.17
R4	75.1	50.5	32.3	20.1	7.07

We conclude that more than 5 years of simulation are enough to draw robust conclusions on surface exchanges, such as dry deposition and emissions, and the consequent changes on atmospheric chemistry. Less robustness is found for parameters for which the connection with

the land surface is less evident and involve different levels of changes in the general circulation and atmospheric dynamics, such as precipitation or cloudiness. Although R drops to low values after 5 years, its large variability suggests that more years are needed to draw strong conclusions involving precipitation.

4.3.6 Summary and discussion

In the present work, the effects of rainfall interception, an important aspect of the terrestrial hydrological cycle, on surface exchange processes and atmospheric chemistry have been assessed. An attempt to understand the complex feedbacks between soil moisture, evapotranspiration and runoff, and their effects on surface exchanges, transport and atmospheric burden of important trace gases such as isoprene, OH, O_3, NO_x, has been made. Including the subgrid variability in rainfall interception reduces the interception loss and increases the plant transpiration with the total evapotranspiration staying more or less the same in tropical forests, but decreasing in savannah regions and/or high altitudes regions where the excess of throughfall feeds the runoff rather than the soil moisture. The decreased evapotranspiration increases the surface temperature, which causes more instability in the boundary layer, causing the PBLH to be deeper. The changes in surface temperature affect also the isoprene emissions and NO emissions. Additionally, rainfall interception on wet skin fraction directly affects the dry deposition velocity of soluble and insoluble gases causing significant changes in the chemical composition of the atmosphere. The changes in precipitation reflect a change in the moisture convergence in the regions considered, but this has been difficult to demonstrate using a passive tracer Rn_{100}. Wang (2007) has shown that the subgrid variability in precipitation in CAM3 (Community Atmosphere Model version 3) causes a decrease in low-level cloudiness, apparent in an increase of the net radiation. This has not been confirmed by our study. This might be due to differences in the cloud cover and convection parametrizations.
Nevertheless, there are still some uncertainties involving the dry deposition formulation, the rainfall interception parametrization and the chemical mechanism:

- Uncertainties in μ factor

  The interception parametrization used in this study is based on the Shuttleworth scheme (Shuttleworth, 1988), which is sensitive to the μ factor and the model timestep. For the latter, to avoid the model sensitivity, a robust canopy hydrology scheme has been proposed by Wang et al. (2005) and Wang (2007) to reduce the temporal resolution sensitivity. Further simulations using this scheme within a GCM are needed to assess the impact of a better representation of rainfall interception on the hydrological cycle and atmospheric chemistry. One of the uncertainties is the specification of the rainfall wetting area μ (the fraction of a grid square where precipitation occurs). Most GCM studies use fixed values of μ that are larger than those estimated from observations. We used an estimate of the precipitating part of the convective cloud based on an updraft velocity

threshold of 1 m/s. This choice results in a convective precipitation coverage of 1-5% (Crutzen and Lawrence, 2000). This way of estimating is an attempt to allow μ to change with time and location and to bring more physical realism into the representation of the subgrid variability of convective rainfall. However, the precipitating part of convective clouds remains difficult to parameterize and further research is being carried out for a better representation of this factor in convection schemes.

- Uncertainties in the uptake of O_3

  Another uncertainty in the calculation of the O_3 dry deposition is associated with the uptake of O_3 by wet vegetation. In our model it is assumed that the non-stomatal uptake of O_3 by vegetation is negligible and that the foliage wetness has an inhibitory effect. The effect of vegetation surface wetness on removal of ozone (O_3) is limited by the fact that the non-stomatal uptake is a poorly understood process. It can range from inhibition to enhancement according to the plant physiology, the source of wetness (i.e., rain or dew or surface hygroscopicity) and the chemical composition of the water (Wesely and Hicks, 2000b).

  The effects of rainfall interception on surface exchanges have highlighted the role of the soil moisture, as a crucial parameter controlling severalaspects of the moisture, energy and chemical compounds exchange between the land surface and the atmosphere. The role of this parameter will be studied in more details in the following chapter.The linkages found between the exchange of various compounds and the terrestrial hydrological cycle demonstrate the control exerted on these fluxesby the land-atmosphere interactions. The hydrological cycle and the biogeochemical cycles are tightly coupled and should be studied togetherfrom the local geographical, to the continental scale.

Chapter 5

Impact of soil moisture on surface exchanges and atmospheric chemistry

5.1 Introduction

The land surface plays a key role in the climate system through interactions with the atmosphere (Sellers et al., 1997; Pitman, 2003; Betts, 2004). Soil moisture (SM) may be the most important state variable in this regard, since it is key for model initial conditions for weather and climate forecasts, and an important factor affecting surface heat fluxes and land surface temperature (Guo and Dirmeyer, 2006). Much research has been conducted on the effects of soil moisture on weather and climate, using various observational studies [e.g., Namias (1960), Betts et al. (1996) and Findell and Eltahir (2003)] and theoretical treatments (Entekhabi et al., 1992; Eltahir, 1998)). Studies with numerical models have been performed to analyze the global or regional sensitivity to soil moisture (Yeh et al., 1984), the response to regional soil moisture anomalies (Rowntree and Bolton, 1983; Kim and Wang, 2007), and the impact of initial soil conditions in weather forecasting models (Mahfouf, 1991; Beljaars et al., 1996; Douville et al., 2007). Several studies have suggested that the projected changes in summer climate strongly rely on soil moisture atmosphere interactions (Koster et al., 2004; Seneviratne et al., 2006; Vidale et al., 2007).

The sensitivity of urban air pollution to other land surface parameters related to soil moisture has been also studied. Taha (1996) and Taha (1997) investigated the effects of increased urban vegetation and reduced air temperatures on ozone air quality in the Los Angeles basin. Jacobson (1999) examined the effects of soil moisture on temperatures, winds and pollutant concentrations.

Soil moisture is a key factor affecting the land surface temperature and latent heat flux, and the partitioning of the energy fluxes between sensible and latent heat. This has consequences not only on climate but also on surface-atmosphere exchanges and the atmospheric burden of important trace gases. Soil moisture is then of primary importance when considering the performance of a general circulation model (GCM). Typically a simulation of a GCM coupled to a land surface model begins from a set of initial atmospheric and land surface boundary conditions specified from analyses from different sources. The coupled system then evolves freely, with only sea surface temperature (SST) as a boundary condition. With the full coupling, errors in one component of the land-atmosphere system may affect other parameters in other components of the model. As an example: atmospheric processes such as precipitation and land processes such as evapotranspiration and soil moisture which evolve simultaneously in GCMs and can cause positive or negative feedbacks. A systematic bias toward an excessive rainfall (due to the convection parametrization, for example) over a location would necessarily lead to a wetter soil. This wetter soil would produce more evapotranspiration, contributing more moisture to the system and enhancing rainfall further (positive feedback). This would amplify the errors introduced by other compartments of the GCM, not necessarily related to the land surface model, even if this individual component were performing perfectly.
There have been attempts to include the soil moisture as a boundary condition in model experiments aiming at exploring the influence of soil moisture on climate variability and predictability (Delworth and Manabe, 1988; Dirmeyer, 2000; Douville, 2002, 2003). These case studies have highlighted the relevance of using realistic and reliable soil moisture boundary conditions. A lack of consistent global estimates of soil moisture, either from an in situ observational network or from satellite remote sensing, has been a major obstacle in performing such experiments. The Global Soil Wetness Project (GSWP) (Dirmeyer, 2000) was created to generate long-term global estimates of SM using uncoupled land surface models driven by meteorological forcing and a common set of soil and vegetation parameters. The resulting GSWP-2 soil moisture simulations are one of the best multiyear global estimates of soil moisture available (Douville, 2004; Guo and Dirmeyer, 2006).
In this study, we apply a climatological soil moisture derived from GSWP-2 as a boundary condition to our atmospheric chemistry general circulation model to assess the sensitivity of surface exchanges (dry deposition and biogenic emissions) and atmospheric chemistry to soil moisture. The simulation experiment design is presented in Section 2. Section 3 describes how specified soil moisture affects the seasonal hydrological cycle and climate simulations. Impacts on micrometeorology are discussed in Section 3, followed by the impacts on emission and dry deposition in Section 4, and finally the effects on the oxidizing capacity of the atmosphere are discussed in Section 5.

5.2 Experiment design

The lack of consistency in the soil moisture representation between land surface models (LSMs) is an important caveat for the application of an external soil moisture product in a GCM. The Project for Intercomparison of Land-surface Parameterization Schemes (PILPS) has shown that different LSMs driven by the same meteorological forcing can produce different surface energy and water budgets, even when certain critical aspects of the LSMs (e.g. vegetation cover, soil properties) are carefully controlled (Koster and Milly, 1997). LSMs have different ranges of SM estimates and a comparison between models is always very tricky. Hence an external SM product cannot be used directly as boundary condition in any LSM. Transferability requires a method of translating soil moisture to a given model from a data source. Several methods of transferability have been proposed by Dirmeyer et al. (2004) and Rodell et al. (2005). We use the method of standard deviation to produce an SM product that follows the time variability and also uses the mean annual cycle and the variance of our model at each grid point:

$$W_{new} = m_M + (W_p - m_p)\frac{\sigma_M}{\sigma_p} \tag{5.1}$$

where W_{new} is the new SM climatology, m_M the mean annual cycle of EMAC calculated from a previous 15 years AMIP-II style integration, m_p the mean annual cycle of the GSWP-2 soil wetness product, W_p is the GSWP-2 soil wetness SM climatology, σ_M is EMAC SM standard deviation, and σ_p is GSWP-2 soil wetness standard deviation. In the present study, EMAC is used to perform global simulations in which soil moisture is either interactive or relaxed toward a monthly mean climatology. Both simulation experiments are summarized in Table 5.1. Each simulation experiment consists of seven years of simulation between 1991 and 1997. The first year is discarded as spin-up. Thus all the results are analyzed over the 6 year period between 1992 and 1997. Both experiments are forced by the AMIP-II observed monthly means SSTs. The monthly mean SM climatology is interpolated linearly on a daily basis. The GSWP-2 soil wetness data are interpolated from $1^\circ \times 1^\circ$ resolution to the GCM grid (T42) using NCREGRID (Jöckel, 2006).

Table 5.1: Summary of the experiments performed in this study.

Name of experiment	period of analysis	SM boundary
CTL	1992-1997	Interactive
SMB	1992-1997	Climatological

5.3 Impact on the seasonal hydrological cycle

The difference between the GSWP soil moisture as specified for the SMB simulation and the soil moisture that evolves freely in the CTL simulation can be large. Figure 5.1 shows the 6-year-averaged spatial distributions of soil moisture for both simulations. A strong drying feature is observed in the Northern Hemisphere tropics in boreal winter and Southern Hemisphere tropics and North Hemisphere midlatitudes over Europe and North America in summer. An increased soil moisture is observed in DJF in eastern Brazil, southern Africa, northern Australia, southern Europe, southeastern US and over the Rocky mountains. In JJA, the soil moisture increases in the monsoon regions in Asia (India and Southeastern Asia), Central Africa and the east coast of South America. The difference between CTL and SMB simulations shows that the free-running model shows excessive moistening due to an overestimation precipitation after the rainy season. The changes in soil moisture have a direct impact on evapotranspiration (Figure 5.2), which shows the same change patterns as for soil moisture in the tropics and midlatitudes.

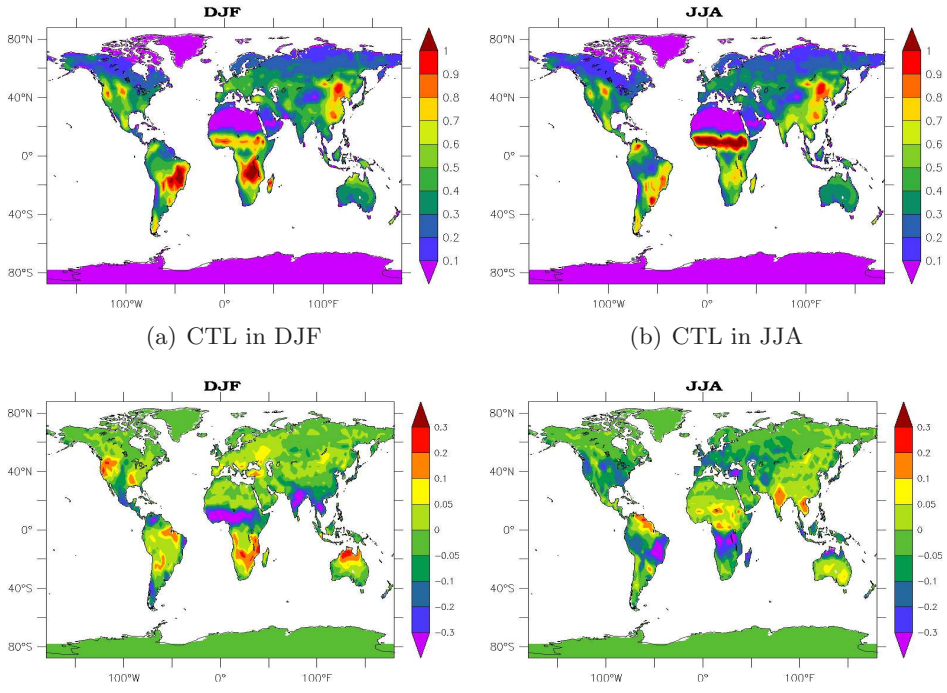

(a) CTL in DJF (b) CTL in JJA

(c) SMB - CTL in DJF (d) SMB - CTL in JJA

Figure 5.1: Soil moisture comparison (in m) between SMB and CTL simulations: (a) CTL simulation for DJF, (b) CTL simulation for JJA, (c) SMB - CTL for DJF and (d) SMB - CTL for JJA.

The strong enhancement in evapotranspiration in the Sahel region and in arid western China in boreal summer shows the high sensitivity of the soil evaporation, as the main contributor to evapotranspiration in these regions, to the slight change in soil moisture (less than 0.05 m) occurring in these regions. The evapotranspiration values in these regions are unrealistic and might be due to a flaw in the soil evaporation parameterization.

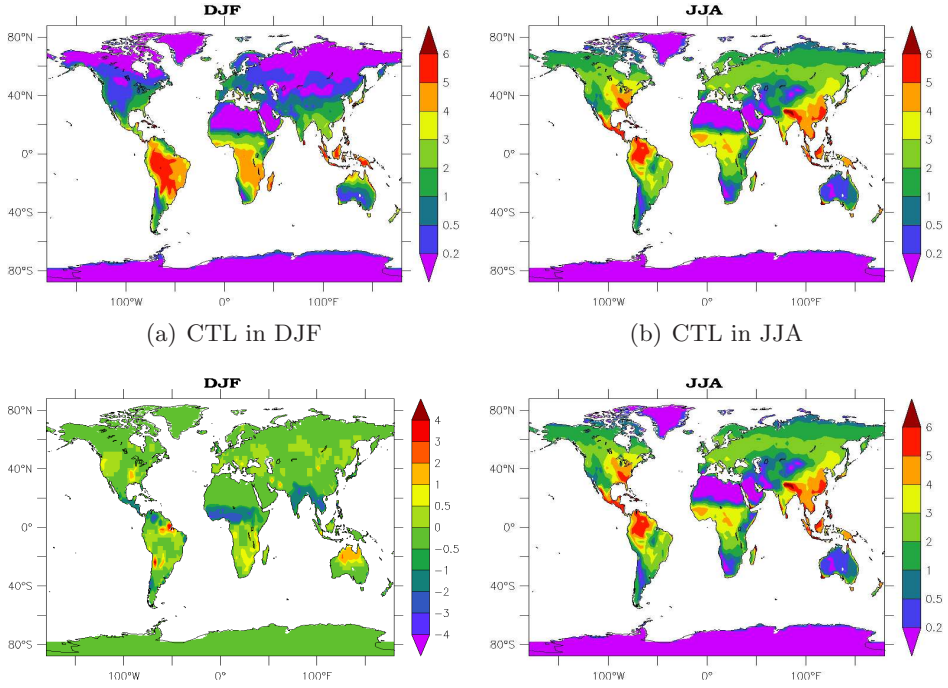

(a) CTL in DJF

(b) CTL in JJA

(c) SMB - CTL in DJF

(d) SMB - CTL in JJA

Figure 5.2: Evapotranspiration comparison (in mm/d) between SMB and CTL simulations: (a) CTL simulation for DJF, (b) CTL simulation for JJA, (c) SMB - CTL for DJF and (d) SMB - CTL for JJA.

The comparison of the water vapor column (WVC) in Figure 5.3 shows an increase over the arid regions of Sahel and North Africa in DJF and JJA, and over Australia in DJF and western China in JJA, whereas a strong decrease is found over the Amazon in JJA. Surprisingly, differences are also found over the oceans. It appears that the changes in soil moisture between CTL and SMB in the tropics and subtropics affect the Hadley, Walker and local land-sea circulations in the Indian Ocean with a decrease of more than 5mm in DJF and an increase of about 3mm in the Western Pacific Intertropical Convergence Zone (ITCZ).

Although the differences in evapotranspiration are highly correlated with the changes in soil moisture with a correlation coefficient of 0.71 and 0.59, over land for DJF and JJA, respectively, the correlations between changes in WVC and soil moisture are found to be very low: 0.04 for DJF and 0.24 for JJA. The low correlations emphasize the small contribution of the local evapotranspiration to the total WVC and the predominant role of advection in determining the water vapor burden in a grid box.

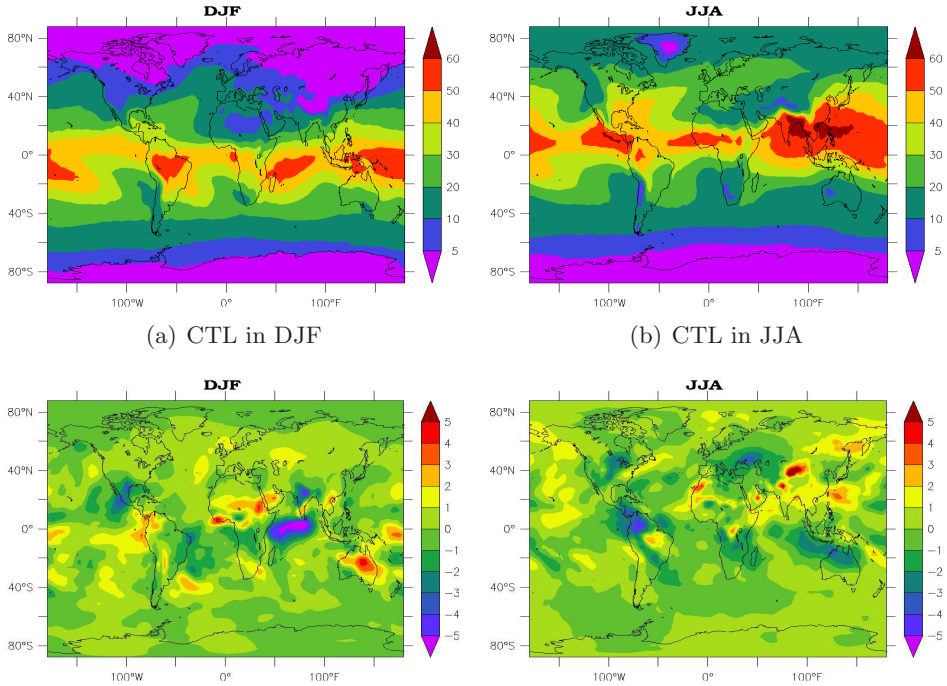

(a) CTL in DJF

(b) CTL in JJA

(c) SMB - CTL in DJF

(d) SMB - CTL in JJA

Figure 5.3: Water vapor column comparison (in mm) between SMB and CTL simulations: (a) CTL simulation for DJF, (b) CTL simulation for JJA, (c) SMB - CTL for DJF and (d) SMB - CTL for JJA.

Similarly there are pronounced differences in precipitation between the SMB and CTL integrations on the local scale. The global distribution changes are shown in Fig. 5.4. Precipitation decreases by up to 5 mm/day over the Amazon and the Indian Ocean, and increases over the western Pacific ITCZ. Changes affect again both tropical and subtropical land and ocean, and the precipitation change patterns are highly correlated with WVC changes with a correlation coefficient varying from 0.55 in DJF to 0.49 in JJA, whereas the correlation between land precipitation and soil moisture is rather low (0.07 in DJF and 0.11 in JJA). As for the WVC,

precipitation is more affected by the changes in large scale circulation, such as the Hadley and Walker circulations, rather than surface conditions. Nevertheless these changes in precipitation are triggered by the changes in land surface conditions. Moreover, the comparison of the SMB run precipitation with GPCP precipitation (not shown here) shows no systematic improvement of the precipitation patterns, and large biases persist over most of the regions affected by an excessive precipitation, such as in the tropics (see Chapter 1). Specifying the model soil moisture might improve the model precipitation in some regions, like over the Indian ocean or the western Pacific ITCZ, by removing some of the unrealistic feedbacks, but can also exacerbate some large biases, as in the eastern Pacific in JJA.

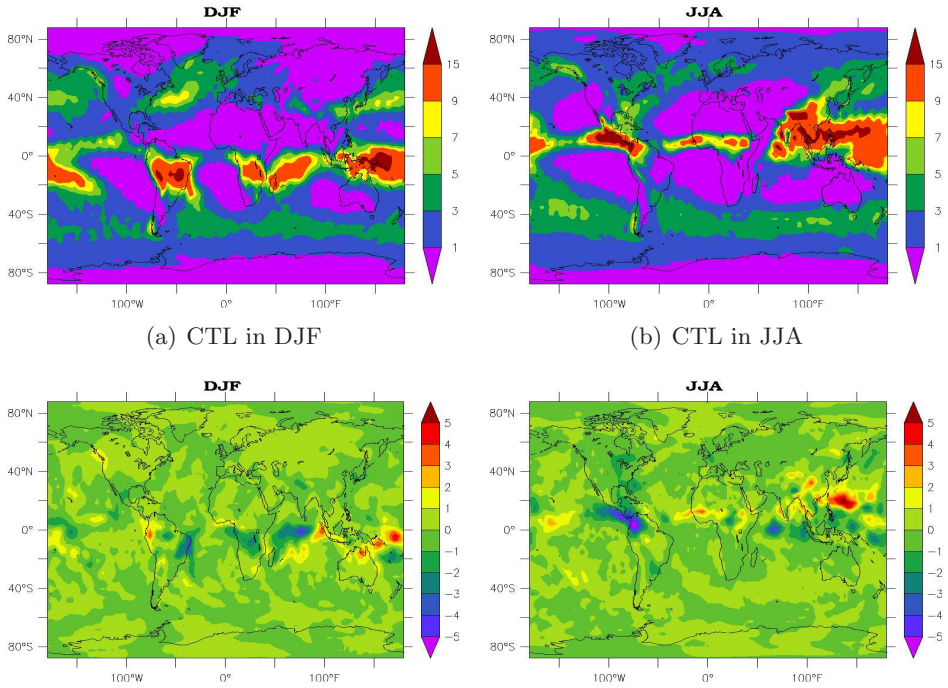

(a) CTL in DJF

(b) CTL in JJA

(c) SMB - CTL in DJF

(d) SMB - CTL in JJA

Figure 5.4: Precipitation comparison (in mm/d) between SMB and CTL simulations: (a) CTL simulation for DJF, (b) CTL simulation for JJA, (c) SMB - CTL for DJF and (d) SMB - CTL for JJA.

To assess the robustness of the response of the precipitation field to changes in soil moisture, we use the ratio R defined in Chapter 4 as a measure of the ratio of noise (interannual variability) to the absolute change (signal). R is calculated for three regions which show a strong change in seasonally averaged precipitation. The ratio shown in Table 5.2 varies in a wide range of 14%-

Table 5.2: The ratio R (see Chap. 4 equation 4.5) as a measure of the robustness of the response of precipitation and surface temperature for 3 regions showing a large change

Precipitation					
	1 years	2 years	3 years	4 years	5 years
85W-65W and 5S-15N	95.3	58.6	37.5	24.1	14.4
10E-40E and 0:20S	107.2	71.0	48.6	28.7	22.0
40E:100E and	118.2	85.1	50.6	28.9	16.2
Surface temperature					
	1 year	2years	3 years	4 years	5 years
75W-38W and 8S:20S	57.6	37.1	25.9	15.2	5.3
10W-40E and 15N-25N	28.5	16.9	9.7	5.0	1.7
100W-70W and 30N-50N	97.2	89.9	64.5	44.6	17.3

118% with a significant tendency towards less noise with an increasing number of simulation years reaching only 14%, 22% and 16% for the 3 regions. This suggests a decreasing interannual variability with an increased number of simulation years, and 5 years of simulation seem to provide robustness in precipitation averages. However, the high variability of R suggests again the sensitive nature of precipitation, as changes in soil moisture induce large perturbations in the general circulation, affecting the conditions for cloud formation and subsequent precipitation.

5.4 Impact on the micrometeorology

5.4.1 Surface temperature and energy balance

The changes in soil moisture only slightly affect the yearly averaged latent heat flux (Fig. 5.5a) in most areas. Nevertheless, pronounced increases are found over the Sahel region, the Middle East region, the Tibetan Plateau and over the northeastern coast of South America. There are also regions over land of reduced latent heat flux, the most prominent being tropical Africa and South America, and the southeastern USA. The changes in the sensible heat flux (Fig. 5.5b) mirror mostly those of the latent heat flux, especially over North Africa. This suggests that much of the soil moisture variation is manifest in the partitioning of available surface energy between latent and sensible heat flux. Figure 5.5e shows the impact on surface temperature, which resembles the sensible heat flux changes. Soil moisture strongly affects surface temperature through changes in the partitioning of the net surface radiation between latent and sensible heat fluxes. Anomalies in outgoing longwave radiation reflect the surface temperature changes, and dominate the changes seen in the net surface longwave radiative flux (Fig. 5.5d). It appears that the slight increase in soil moisture in some arid regions serves to enhance evaporation and latent heat flux at the expense of other surface energy fluxes, cooling

(up to 5K) the surface in those areas. Regions with decreasing soil moisture are subject to the opposite effect. The increase/decrease in the latent heat flux appears to also have little effect on cloudiness, as indicated by the change in net surface shortwave radiation (Fig. 5.5c).

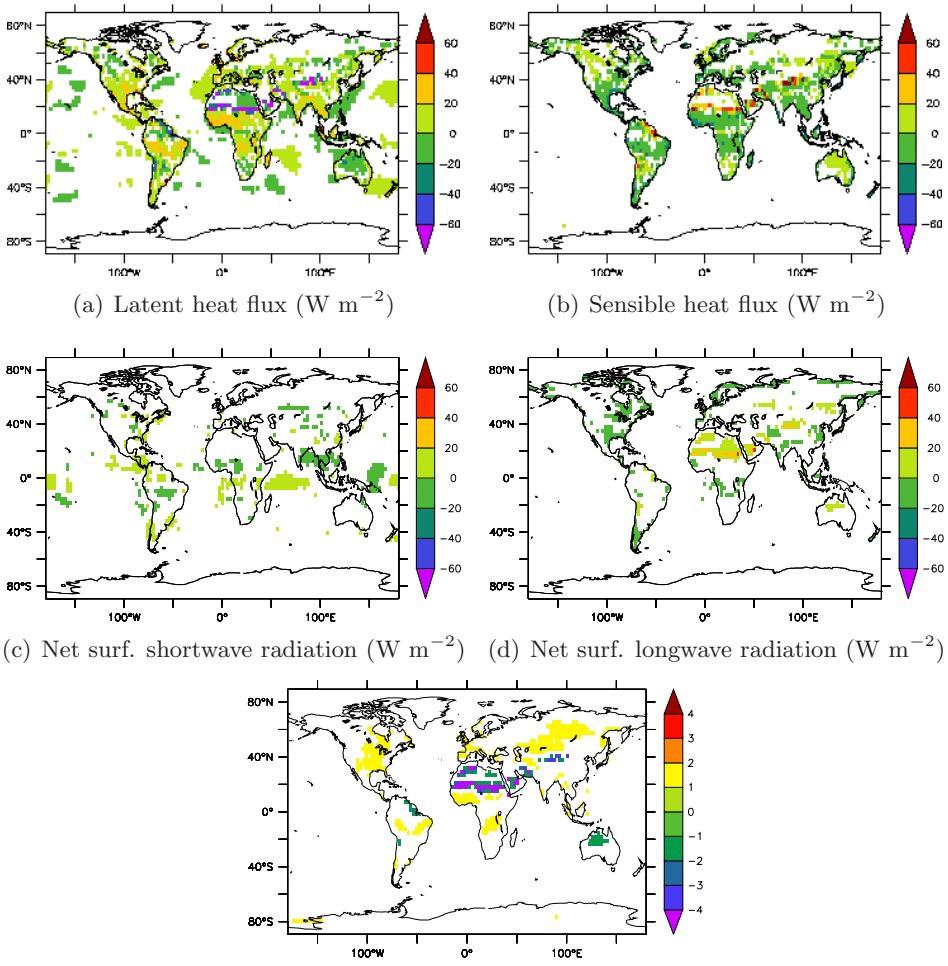

(a) Latent heat flux (W m^{-2})

(b) Sensible heat flux (W m^{-2})

(c) Net surf. shortwave radiation (W m^{-2})

(d) Net surf. longwave radiation (W m^{-2})

(e) Surface temperature (K)

Figure 5.5: Absolute change (SMB-CTL): (a) latent heat flux (W m^{-2}), (b) sensible heat flux (W m^{-2}), (c) Net surface shortwave radiation (W m^{-2}), (d) Net surface longwave radiation (W m^{-2}), (e) Surface temperature (K)

The ratio R, calculated above in Table 5.2, shows that the response to changes in soil moisture appears to be more robust for the surface temperature, with a range between 5% and 97% for

all regions affected by the changes, with a net decreasing trend of the noise with the number of simulation years and much less variability than for precipitation. Soil moisture directly affects surface temperature through the partitioning of the net surface radiation between latent and sensible heat flux.

5.4.2 Vertical transport and Planetary Boundary Layer Height (PBLH)

The effects of soil moisture on vertical transport are assessed through the use of artificial tracers similar to Radon 222: Rn_{01}, Rn_{10} emitted over land with a constant flux of 1 atom/(cm^2.s), and a lifetime of one day and ten days, respectively. Not being chemically reactive, these tracers are suitable to study the effects of the land surface changes on turbulence and convection, two processes occurring on similar timescales. The yearly averaged global distribution of the difference between the two simulations for Rn_{01} and Rn_{10}, shown in Figures 5.6a-b, suggest an accumulation of the tracers near the surface over northeastern coast of South America and the desert areas of the Sahel and North Africa, Saudi Arabia and central Asia. Alternatively a dilution effect is observed over the Amazon and eastern Brazil in South America, central and eastern US, central Africa, India and the Indochinese Peninsula. These changes inversely match the changes observed in surface temperature in Fig. 5e. The increase in surface temperature makes the atmosphere more buoyantly unstable and enhances the thermal turbulence, causing the tracers to be mixed to a greater height.

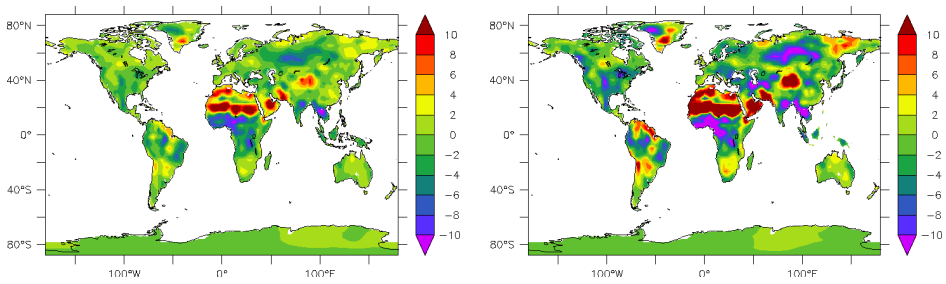

(a) Radon 1 day (b) Radon 10 days

Figure 5.6: Absolute change (SMB-CTL) of the (a) Rn_{01} and (b) Rn_{10} mixing ratios at the surface (in 10^{-21} mol/mol) between SMB and CTL simulations

This is supported by the changes in the PBLH, presented for January and August in Figure 5.7. The large increase (up to 100 %) in both seasons in the eastern USA and southern Brazil (boreal summer), central Africa (in both seasons), and southeastern Asia (in boreal winter) is clearly associated with the dilution effect observed for the artificial tracers. The same is true for regions with maximum concentrations at the surface associated with shallower PBLH such as the northeastern part of South America and North Africa.

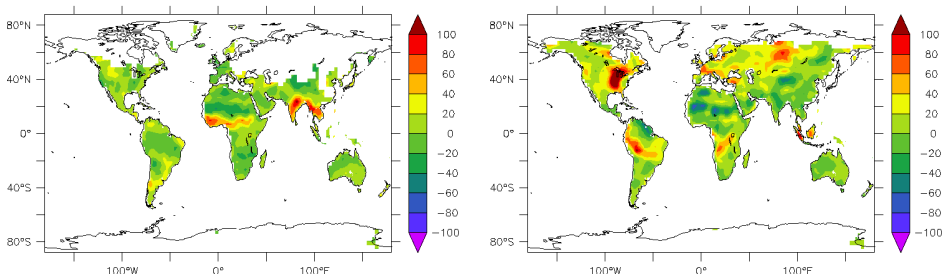

(a) January (b) August

Figure 5.7: Relative PBL height change ($\frac{SUBGRID-BASE}{BASE}$, in %) in (a) January and (b) August

5.5 Impact on surface exchanges

5.5.1 Emissions

The biogenic emissions of isoprene are calculated as a function of surface radiation and temperature, among other factors. The soil moisture changes induce hardly any change in the net surface radiation, but cause significant changes in surface temperature, as shown above. These changes mainly affect the tropics, characterized by high isoprene emissions. Figure 5.8 shows the high relative increase in isoprene emissions over southeastern Asia in DJF and over the Eastern US, southern Brazil and over Angola in JJA. A slight relative decrease is observed over the northeastern coast of South America can be attributed to the slight decrease (less than 2K) in surface temperature. Although dependent on soil moisture and temperature, the NO emissions are not affected by the changes induced by our experiment due to the arbitrary definitions of dry and wet soils in the Yienger and Levy (1995) algorithm.

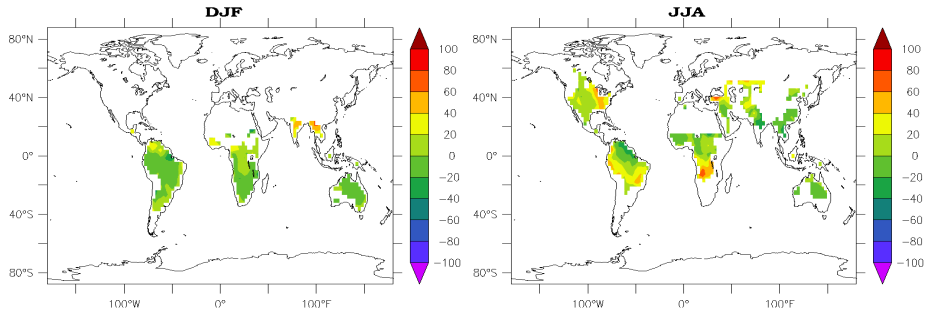

Figure 5.8: Relative change ($(\frac{SUBGRID-BASE}{BASE}$, in %) of isoprene emission flux (molec cm^2/s) in (a) DJF and (b) JJA , for absolute emission flux higher than 0.1 cm/s

5.5.2 Dry deposition

To illustrate the impact of the changes in soil moisture, we analyze the seasonal effects on the dry deposition, focusing on trace gases with contrasting solubilities, O_3 and HNO_3 (nitric acid vapour) with a low and with a high solubility, respectively and NO_x. O_3 plays an important role in tropospheric chemistry and dry deposition is one of its important sinks. NO_x is of major importance for the photochemical production of O_3, and HNO_3 serves as a sink for NO_x through the reaction between NO_x and OH.

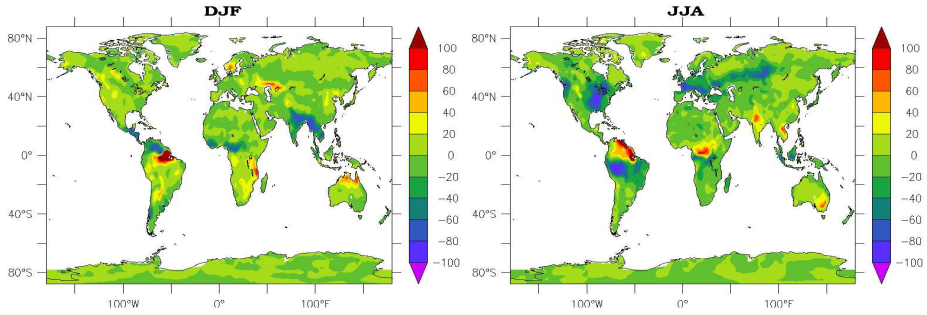

(a) O_3

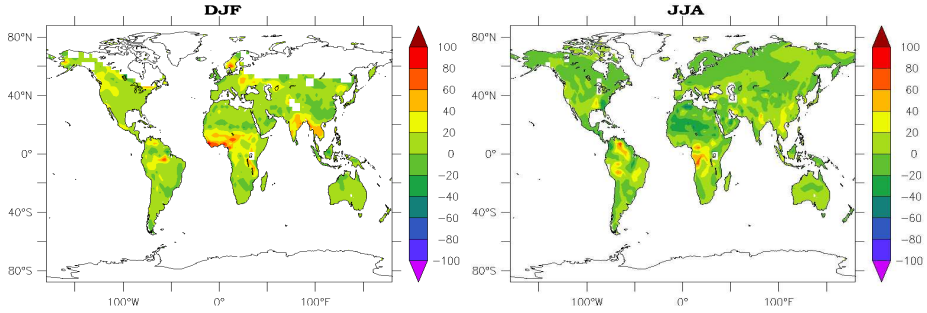

(b) HNO_3

Figure 5.9: Relative change ($\frac{SUBGRID-BASE}{BASE}$) of (a) V_{dO3} and (b) V_{dHNO3} (in %) in DJF and JJA, for absolute dry deposition velocities higher than 0.1 cm/s.

The O_3 dry deposition velocity (V_{dO3}) is controlled by the stomatal aperture of the vegetation, whereas the dry deposition velocity for gas phase HNO_3 (V_{dHNO3}) is controlled by the aerodynamic resistance over most surfaces, which suggests that a more efficient turbulence enhances deposition (Ganzeveld and Lelieveld, 1995). As for O_3, plus taking into account the canopy interactions through the canopy reduction factor, the NO_2 dry deposition velocity is controlled by the stomatal uptake in vegetation. The changes observed in vegetated areas in both seasons,

DJF and JJA, support the dependence of the dry deposition velocities of O_3 and NO_2 to the changes in stomatal conductance and its sensitivity to soil moisture (Fig. 5.9 for O_3, NO_2 not shown). A strong enhancement is observed in DJF over eastern Brazil, reaching more than 100%, but also over eastern Africa and northern Australia. In JJA, the increase is apparent over southeastern Asia, the northern part of South America, Congo and southeastern Australia. The soil drying causes the dry deposition velocities to decrease strongly over Colombia, the Gulf of Guinea and southeastern Asia in DJF, and over the southeastern US, western Brazil and the region extending from southern Europe to southern Russia. The seasonal global changes in NO/NO_2 (not shown) have similar distribution patterns and intensity to V_{dO3}. The relative increase in V_{dHNO3} (Fig. 5.9b) over central Africa and southeastern Asia in both seasons confirms the dependence of this parameter to the turbulence in the boundary layer, shown in the previous section.

5.6 Impact on the oxidizing chemistry of the Troposphere

The global distribution of the relative change of the isoprene surface layer mixing ratio between our two simulations (Fig. 5.10) follows the same patterns as for the isoprene emissions, reaching maximum increases over South America in Colombia in DJF and Brazil in JJA, over central Africa in DJF and JJA and over the eastern USA and Central Asia in JJA.
Despite the changes observed in NO_x deposition velocities and the related changes of the deposition fluxes observed over western Europe and the eastern USA (not shown), the NO_x surface layer mixing ratio (not shown) remains nearly the same over these regions, supporting the hypothesis that the changes due to dry deposition are balanced by feedbacks in the chemistry and the changes in the boundary layer height. Figure 5.11 shows the DJF and JJA relative difference of the O_3 surface layer mixing ratio between the SMB and CTL simulations. Changes reaching up to -40%, affect tropical regions in Amazonia and central Africa in DJF and JJA, whereas a significant increase is observed in the Northern Hemisphere in JJA, reaching more than +50% in the eastern US. The observed changes are generally smaller in magnitude than the differences in O_3 deposition, as in northeast South America, and southeastern Asia where the dry deposition differences reach more than 80%, but the differences in concentrations are less than 20%. The O_3 deposition flux shows the same patterns of relative change as for the O_3 deposition velocity. This emphasizes the role of dry deposition as an important sink for surface ozone. The increase in isoprene concentrations over South America, central Africa and over the eastern US and Asia also contribute partly to ozone production in the presence of more NO_x in the case of regions with relatively high concentrations (eastern USA and India, for instance), affected by a decrease in its dry deposition flux. In tropical south America and central Africa, where the dominant source of NO_x is soil NO emissions and biomass burning, the changes in NO_x dry deposition fluxes, being the same as for O_3, might also contribute to ozone production. Interestingly, the effects of the drastic changes in the PBLH are counteracted by the changes

in dry deposition of O_3 and its precursors NO_x and isoprene.

Major relative differences in the OH surface mixing ratio (Figure 5.12) affect the desert areas of the Sahel, North Africa and the Arabian peninsula in both seasons, with an increase reaching up to 100% in DJF. A large decrease is also observed over India and central Africa in DJF, and over Amazonia, central Africa south of the Equator and southern Europe in JJA. The large changes in desert zones and Southern Europe in JJA can be attributed to the changes in water vapour, shown in Fig. 5.4. The decrease over Africa, India and Amazonia is correlated with the increase in isoprene surface mixing ratio, but this should be confirmed using the chemical budgeting tools, which are not included in this study.

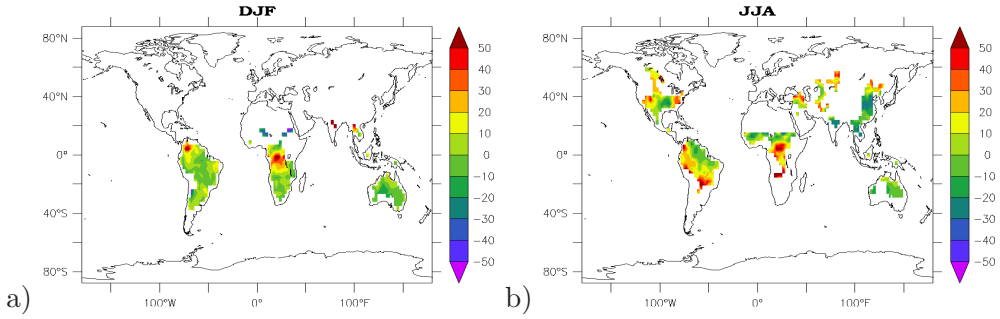

Figure 5.10: Relative change ($\frac{SUBGRID-BASE}{BASE}$) of the isoprene surface layer mixing ratio (in %) in (a) DJF and (b) JJA, shown only for mixing ratios higher than 1 nmol/mol

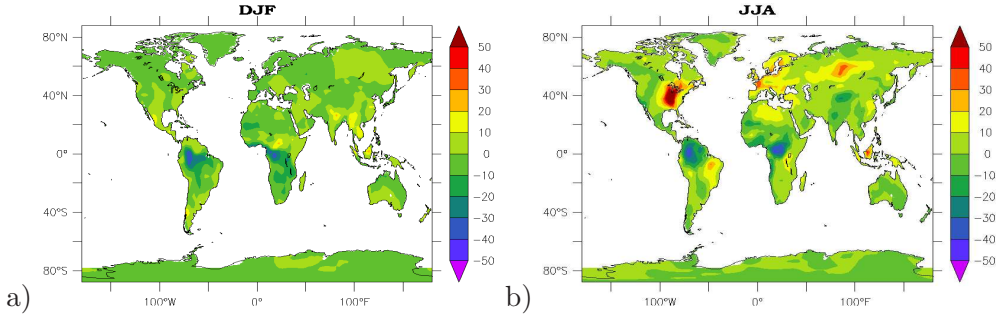

Figure 5.11: Relative change ($\frac{SUBGRID-BASE}{BASE}$) of the O_3 surface layer mixing ratio (in %) in DJF and JJA

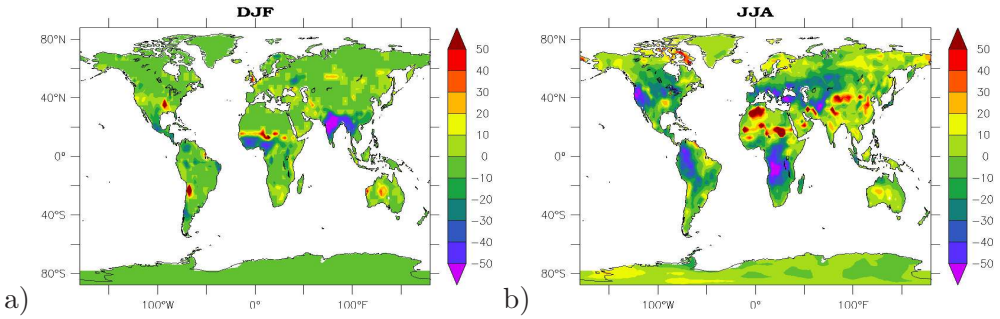

Figure 5.12: Relative change ($\frac{SUBGRID-BASE}{BASE}$) of the OH surface layer mixing ratio (in %) in (a) DJF and (b) JJA

5.7 Summary and discussion

This chapter examined the effects of soil moisture forcing in EMAC on the hydrological cycle, micrometeorology, surface exchanges and the oxidizing capacity of the atmosphere. Two simulations were performed: a baseline simulation with an interactive soil moisture and a simulation with prescribed soil moisture using a soil moisture climatology derived from the GSWP-2 product. Changes in soil moisture have a substantial effect on local surface latent heat fluxes. Evapotranspiration appears to be changed either in vegetated areas where the plant canopy exerts a control over the total evapotranspiration or desert areas where soil evaporation is the dominant component in evapotranspiration. The strong increase observed over the Sahel in boreal summer appears to be not realistic. This might be due to a misrepresentation in the soil evaporation parameterization, which shows a large sensitivity to small changes in soil moisture. The changes in surface fluxes also affect remote precipitation but not in a systematic manner, but these changes are of the same order as the apparently random perturbations in precipitation inherent in any coupled model system.

The patterns of the changes in latent heat fluxes are usually the same as for other fluxes. An increase (decrease) in soil moisture causes an increase (decrease) in surface latent heat flux, with a corresponding decrease (increase) in sensible heat flux. The land surface is cooler (warmer), and the longwave radiation is reduced (increased), although to a lesser extent than the changes in the heat fluxes. The changes in surface exchanges are affected by the changes in soil moisture, through the regulation of the stomatal conductance for dry deposition: an increase (decrease) in soil moisture brings about an increase (decrease) in stomatal conductance, corresponding to an increase (decrease) in the dry deposition velocity of trace gases for which dry deposition is controlled by the stomatal aperture, like ozone and NO_x. The changes in surface temperature affect the vertical transport in the boundary layer: an increase (decrease) in the surface temperature causes more (less) turbulence and the aerodynamic resistance is

increased (reduced), increasing the dry deposition of HNO_3. The PBL height also becomes deeper (shallower) causing a potential dilution of the trace gases at the surface. However, the trace gas burden appear to be more affected by the changes in emissions/dry deposition than the changes in the PBLH.
The isoprene emissions show a clear sensitivity to the changes in surface temperature. The MEGAN algorithm (Guenther et al., 2006) has demonstrated another direct effect of soil moisture with a regional increase/decrease of isoprene emissions by about 40%. The soil moisture forcing might help to assess the impact of this direct effect on isoprene emissions in EMAC. Additionally, large uncertainties remain in the NO emissions and the effects of soil moisture on pulsing or the changes in the microbiological activity of the soil. Alternative NO emissions algorithms should be considered.
The results show that there is significant interannual variability in precipitation, but rather robust results for surface temperature, becoming more robust with the number of simulation years. To reduce this variability, longer integrations are probably needed to show the impact of soil moisture changes on other aspects of surface exchanges such as wet deposition. Such aspects have been omitted in this study and the focus has been made on the surface exchanges directly affected by the changes in the soil moisture. These aspects show less interannual variability and provide a strong and significant signal after merely 3-4 years of simulation.

Chapter 6

Conclusions

The aim of this work, as presented in the introduction chapter, has been to better understand some of the feedbacks between the land surface hydrology and atmospheric chemistry. This was motivated by the dependence of the surface-atmosphere trace gas exchanges, such as dry deposition and emissions, to important hydrological processes represented in the land surface model. A first step toward this aim has been the understanding of the interactions between the terrestrial and atmospheric parts of the hydrological cycle, through an evaluation of selected features such as evapotranspiration, water vapor column and precipitation. The precipitation rates from two simulations, using T42L31 and T63L31 resolutions, have been compared to GPCP and CMAP data. The comparisons showed large biases over the tropical regions and high mountain chains. An excess in precipitation causes an overestimation of the model evapotranspiration compared to the GSWP2 dataset evapotranspiration over the same regions. Nevertheless high evapotranspiration rates as in northern Amazon or in southern Africa (mostly vegetated areas) are not correlated with high precipitation rates, which can be attributed to a longer soil moisture memory allowing a time lag in transpiration. The simulated water vapor fields have been extensively evaluated against GOME WVC for the total water vapor column (TWVC), and the MCOS global radiosondes data set which include specific humidity fields, relative humidity and temperature fields. Water vapor is an important climate variable and crucial for the oxidizing capacity of the atmosphere, at the interface between the land surface and the atmosphere. In general, water vapor columns agree well with observations in zonal means and seasonal averages, though TWVC are found to be slightly overestimated over the ITCZ over land, correlated with the high precipitation rates. This does not apply to oceanic TWVC. Most regions with high precipitation rates are more consistent with major moisture convergence regions rather than high TWVC, indicating that the changes in precipitation are probably mainly due to changes in water vapor transport and local evaporation changes may play only a minor role in the precipitation changes. The excess of evapotranspiration initiated by an overestimation in precipitation may sustain more water vapor, reaching the threshold to

make substantial rainfall to occur. The comparison with the MCOS fields: TWVC, specific humidity, relative humidity and temperature profiles, confirms the model overestimation of the humidity fields at the surface, especially over the tropics. Other discrepancies are found in the upper troposphere, due to some inconsistencies in MCOS data and probably the calculation of the model saturation vapour pressure. These inconsistencies have no impact on our results near the surface. The large biases found between the model precipitation, evapotranspiration and humidity fields at the surface and possible errors in the hydrological cycle over land are not only the result of a misrepresentation of the land surface model. Other processes of the atmospheric system, such as convection, have inaccuracies that might be partly or totally responsible for these errors (see Tost et al., 2007). Nevertheless, the land surface may largely affect the Earth system in a different manner, by modulating the surface exchanges of trace gases and the consequent effects on the chemical composition of the atmosphere.

The rainfall interception is an important hydrological process controlling the surface wetness that affects the stomatal uptake of O_3, among other trace gases. In Chapter 4, the impact of a parametrization taking into account the subgrid-variability of rainfall interception in the LSM on the hydrological cycle, dry deposition and emissions are analyzed. The newly implemented parametrization affects highly the repartitioning between evaporation and transpiration on the one hand, with a decrease in interception loss and increase in transpiration, and between runoff and evapotranspiration on the other hand, depending on the regional topography and the vegetation type and density. The effects on four regions with different characteristics have been shown and two hydrological regimes have been defined to distinguish between the regions: a "runoff regime", where the decrease in interception loss is compensated by an excess of runoff and the soil moisture is depleted by excess of transpiration, and an "evapotranspiration regime" where the interception loss is compensated by transpiration fed by an increase in soil moisture. The evapotranspiration decrease in all regions is caused mainly by the soil moisture decrease, and not the decrease in the wet skin fraction. The resulting increased surface temperature enhances the atmospheric instability, reflected by a deeper boundary layer. Moreover, the combined effects of the wet skin fraction and soil moisture alter the dry deposition velocity of soluble gases, such as HCOOH, and insoluble gases, such as O_3. The effects on NO and VOC emissions are found to be non-negligible, being the result of the changes in the surface temperature and soil moisture. The impact on the oxidation capacity of the atmosphere is more difficult to assess directly, even though the chemical mechanism we have chosen is simple and does not reflect the entire complexity of the chemical feedbacks involved. The changes in dry deposition and VOC emissions are compensated by several feedbacks in chemistry.

The analysis of the role of canopy hydrology (reflected by the changes in rainfall interception) in surface exchanges highlights the role of soil hydrology (reflected by the role of soil moisture) as a crucial aspect of land surface modeling. In Chapter 5, a soil moisture forcing is applied to the EMAC model, suppressing the coupling between the excessive precipitation and the model's soil moisture. This has a direct impact on the local evapotranspiration, especially in the transition period between seasons. Besides the dependencies between evapotranspiration,

surface temperature and PBLH analyzed in the previous chapter, changes in the local vertical transport and large circulation (reflected by changes in precipitation and the water vapour column) have been found. A large signal from these changes is observed in some tropical regions, but the interannual variability remains large in our multi-year simulations. Our simulations with a complete coupling of the climate-atmospheric chemistry system (although using a simple chemical mechanism) requires large CPU (Central Processing Unit) time, and the type of simulations used in the climate research community (using either ensemble simulations or long simulations of several decades) are not yet feasible. Nevertheless, our prime purpose goes beyond the assessment of the role of the land surface on climate, whereas we focus more on the effects on trace gases exchanges. These aspects of our results, related to evapotranspiration, surface temperature, dry deposition and emissions, showed more robustness after 4-5 years of simulation than the climate related aspects.

Understanding the interactions between the land surface hydrology and atmospheric chemistry provides the opportunity to assess the potential impact of a changing climate system, affecting the hydrological cycle, on the atmospheric chemical composition and its consequences for the climate. In addition, the land use changes (such as deforestation and irrigation), related to the global socio-economical changes, imply changes in the land surface hydrology and contribute to changes in the climate system not only through the physical feedbacks inherent to the climate system, but also through the chemical composition of the atmosphere. This should make the atmospheric chemistry community aware of the importance of such processes, and make use of the research advances in hydrology. The sensitivity experiments did not include comparisons with observations. As future extension of this work, comparisons with measured interception losses, throughfalls as well as dry deposition velocities or emission fluxes should be added.

In future EMAC will be applied to study complex interactions between physical and chemical processes considering changes in the land surface on a global scale. However, large uncertainties remain in the characterization of dry deposition and emission algorithms. The O_3 uptake by wet surfaces is still under debate; observations suggest an uptake by wet vegetation (Altimir et al., 2006) (and references therein) and this process needs to be included in dry deposition models. The uncertainties in NO emissions and their dependencies to soil moisture and temperature might be reduced using a third generation land surface model (Pitman, 2003) that incorporate a simulation of the hydrological cycle including an explicit representation of plant canopy, snow cover, soil moisture profile, and the advances in biogeochemical and biogeographical modeling including the carbon cycle, the nitrogen cycle and the vegetation dynamics. Comprehensive models such as DAYCENT or CLM (Community Land Model) could be used to reduce such uncertainties.

In this study, the effects on aerosols exchanges were not considered. There is a potential impact of the land surface hydrology on aerosols. The terrestrial hydrological cycle may modulate aerosols as dust and biogenically derived particles through terrestrial ecosystems. Additionally, biogenic aerosols are linked with the atmospheric branch of the hydrological cycle (cloud formation and rainfall) through cloud and precipitation formation. The effects on VOC emissions

assessed in this study could be extended to the secondary aerosol production. Likewise, the soil moisture might contribute significantly to the total aerosol burden through the emission of microbial particles and mineral dust (Barth et al., 2005). Studies show the crucial role of soil moisture in mineral dust emissions through the change of erosion thresholds (Laurent et al., 2008).

Appendix A

Abbreviations and variable definitions

Table A.1: Acronyms and abbreviations

Acronym	Description
AMIP	Atmospheric Model Intercomparison Project
AIRS	Atmospheric Infrared Sounder satellite system
BVOC	Biogenic Volatile Organic Compounds
CCM3	Community Climate Model
CMAP	Climate Prediction Center (CPC) Merged Analysis of Precipitation
DJF	December-January-February
ECHAM5	European Centre Hamburg Model (global climate model)
ECMWF	European Centre for Medium Range Weather Forecasts
EMAC	ECHAM/MESSy Atmospheric Chemistry
ENSO	El Niño Southern Oscillation
ERA40	40 year dataset of meteorological reanalysis by ECMWF
GCM	General Circulation model
GEWEX	Global Energy and Water Cycle Experiment
GOME	Global Ozone Monitoring Experiment
GPCP	Global Precipitation Climatology Project
GSWP2	Global Soil Wetness Project Phase 2
HIRS	High-resolution Infrared Radiation Sounder
ISLSCPII	International Satellite Land Surface Climatology Project Initiative II
ITCZ	Inter Tropical Convergence Zone

Table A.1: Acronyms and abbreviations (... continued)

Acronym	Description
JJA	June-July-August
KPP	Kinetic PreProcessor
LSM	Land Surface Model
MAM	March-April-May
MESSy	Modular Earth Submodel System
MCOS	Max Planck Institute for Chemistry Operational Sonde data set
MPIM	Max Planck Institute for Meteorology
MEGAN	Model of Emissions of Gases and Aerosols from Nature
NCAR	National Center for Atmospheric Research (USA)
NCEP	National Center for Environmental Prediction
NMHC	Non-Methane Hydrocarbons
NMVOC	Non-Methane Volatile Organic Compounds
NRMSE	Normalized Root Mean Square Error
NSTD	Normalized Standard Deviation
NVAP	NASA Water Vapor Project
PAR	Photosynthetically Active Radiation
PILPS	Project for the Intercomparison of Land-surface Parameterization Schemes
PBL	Planetary Boundary Layer
SACZ	South Atlantic Convergence Zone
SON	September-October-November
SPCZ	South Pacific Convergence Zone
SSM/I	Special Sensor Microwave Imager
SST	Sea Surface Temperature
SM	Soil Moisture
TOVS	TIROS-N Operational Vertical Sounder
TWVC	Total Water Vapor Column
VOC	Volatile Organic Compounds

Table A.2: Variables and units

Variable	Description	Unit
C	net convergence of atmospheric water vapor flux over the control region	m

Table A.2: Variables and units (... continued)

Variable	Description	Unit
C_h	transfer coefficient for heat	
C_l	wet skin fraction or fraction of the grid-cell covered with water	1
C_{sn}	fraction of the grid-cell covered with snow	1
C_v	grid fraction occupied by vegetation	1
E	Evapotranspiration	m
E_v	evaporation from vegetative surface	m
F_c	deposition flux	molecules m^{-2} s^{-1}
$F(W_s)$	available water in the root zone	1
G	soil heat flux	W m^{-2}
h	relative humidity	1
H	Sensible heat flux	W m^{-2}
I	Rainfall Interception	m
J_q	moisture flux over sea	kg m^{-2} s−1
J_{qdv}	evaporation from dry (no water in skin reservoir) vegetated areas	kg m^{-2} s−1
J_{qs}	Evaporation from snow and the skin reservoir	kg m^{-2} s−1
J_{qw}	evaporation from bare soil	kg m^{-2} s−1
LAI	leaf area index	-
p_s	surface pressure	Pa
P	precipitation	m
q	specific humidity	kg kg^{-1}
q_s	saturation specific humidity	kg kg^{-1}
R	runoff	m
R_a	aerodynamic resistance	s m^{-1}
R_b	quasi-laminar boundary-layer resistance	s m^{-1}
R_{co}	stomatal resistance of the canopy	s m^{-1}
R_{net}	net radiation	W m^{-2}
R_{sd}	downwelling solar radiation	W m^{-2}
R_{ld}	downwelling longwave radiation	W m^{-2}
R_{surf}	surface resistance	s m^{-1}
S	terrestrial water storage	m
S_v	moisture stored on the surface of vegetation	m
T	Throughfall	m
T_s	surface temperature	K

Table A.2: Variables and units (... continued)

Variable	Description	Unit
v_d	dry deposition velocity for a trace gas	m s^{-1}
v_h	horizontal wind vector	m s^{-1}
w	precipitable water	m
W_l	skin reservoir content	m
W_{lmx}	maximum skin reservoir content	m
W_{lmax}	maximum amount of water that can be held on one layer of leaf or bare ground	m
W_{pwp}	permanent wilting point	m
W_s	total amount of water available in the root zone	m
W_{Smax}	field capacity	m
α_s	the surface albedo	1
ϵ	surface emissivity	-
λ	latent heat of vaporization or sublimation of water 2.5008*10^6/2.8345*10^6	J/kg
σ	Stefan-Boltzmann constant 5.67*10^-8	W/m^2 K^4
ρ	the air density	kg m^{-3}

Appendix B

Description of the statistical parameters

The statistics that are applied in this thesis are standard, based on basic text books of statistical analysis (e.g., Wilks, 2005). For completeness they are presented in this section. The used parameters are:

- The mean value $\bar{f}$: It is defined by the sum of all values f_n, divided by the number of valid points N:

$$\bar{f} = \frac{1}{N} \sum_{n=1}^{N} f_n \tag{B.1}$$

- The bias $\bar{E}$: It is defined by the difference of the mean values of the simulation $\bar{f}$ and the reference $\bar{r}$.

$$\bar{E} = \bar{f} - \bar{r} \tag{B.2}$$

  The bias expressed in %:

$$\bar{E} = 100 * \frac{\bar{f} - \bar{r}}{\bar{r}} \tag{B.3}$$

- The standard deviation:

$$\sigma_f = \sqrt{\frac{1}{N} \sum_{n=1}^{N} (f_n - \bar{f})^2} \tag{B.4}$$

$$\sigma_r = \sqrt{\frac{1}{N}\sum_{n=1}^{N}(r_n - \bar{r})^2} \tag{B.5}$$

The normalized standard deviation NSTD is expressed by:

$$NSTD = \frac{\sigma_f}{\sigma_r} \tag{B.6}$$

- The root mean square RMS E It is defined by the square-rooted sum of the squared differences of the values of the simulation f_n and the reference r_n:

$$E = \sqrt{\frac{1}{N}\sum_{n=1}^{N}(f_n - r_n)^2} \tag{B.7}$$

The normalized root mean square NRMSE:

$$NRMSE = \frac{E}{\sigma_r} \tag{B.8}$$

- The correlation r (usually r^2 is used) is defined by:

$$r = \frac{\frac{1}{N}\sum_{n=1}^{N}(f_n - \bar{f})(r_n - \bar{r})}{\sigma_f \sigma_r} \tag{B.9}$$

Appendix C

MECCA Reaction Tables

Table C.1: Gas phase reactions

#	reaction	rate coefficient	reference
G1000	$O_2 + O(^1D) \rightarrow O(^3P) + O_2$	`3.2E-11*EXP(70./temp)`	Sander et al. (2003)
G1001	$O_2 + O(^3P) \rightarrow O_3$	`6.E-34*((temp/300.)**(-2.4))*cair`	Sander et al. (2003)
G2100	$H + O_2 \rightarrow HO_2$	`k_3rd(temp,cair,5.7E-32,1.6,7.5E-11,0.,0.6)`	Sander et al. (2003)
G2104	$OH + O_3 \rightarrow HO_2$	`1.7E-12*EXP(-940./temp)`	Sander et al. (2003)
G2105	$OH + H_2 \rightarrow H_2O + H$	`5.5E-12*EXP(-2000./temp)`	Sander et al. (2003)
G2107	$HO_2 + O_3 \rightarrow OH$	`1.E-14*EXP(-490./temp)`	Sander et al. (2003)
G2109	$HO_2 + OH \rightarrow H_2O$	`4.8E-11*EXP(250./temp)`	Sander et al. (2003)
G2110	$HO_2 + HO_2 \rightarrow H_2O_2$	`k_HO2_HO2`	Christensen et al. (2002), Kircher and Sander (1984)*
G2111	$H_2O + O(^1D) \rightarrow 2\ OH$	`2.2E-10`	Sander et al. (2003)
G2112	$H_2O_2 + OH \rightarrow H_2O + HO_2$	`2.9E-12*EXP(-160./temp)`	Sander et al. (2003)
G3101	$N_2 + O(^1D) \rightarrow O(^3P) + N_2$	`1.8E-11*EXP(110./temp)`	Sander et al. (2003)
G3103	$NO + O_3 \rightarrow NO_2 + O_2$	`3.E-12*EXP(-1500./temp)`	Sander et al. (2003)
G3106	$NO_2 + O_3 \rightarrow NO_3 + O_2$	`1.2E-13*EXP(-2450./temp)`	Sander et al. (2003)
G3108	$NO_3 + NO \rightarrow 2\ NO_2$	`1.5E-11*EXP(170./temp)`	Sander et al. (2003)
G3109	$NO_3 + NO_2 \rightarrow N_2O_5$	`k_NO3_NO2`	Sander et al. (2003)*

Table C.1: Gas phase reactions (... continued)

#	reaction	rate coefficient	reference
G3110	$N_2O_5 \rightarrow NO_2 + NO_3$	`k_NO3_NO2/ (3.E-27*EXP(10990./temp))`	Sander et al. (2003)*
G3200	$NO + OH \rightarrow HONO$	`k_3rd(temp,cair,7.E-31, 2.6,3.6E-11,0.1,0.6)`	Sander et al. (2003)
G3201	$NO + HO_2 \rightarrow NO_2 + OH$	`3.5E-12*EXP(250./temp)`	Sander et al. (2003)
G3202	$NO_2 + OH \rightarrow HNO_3$	`k_3rd(temp,cair,2.E-30, 3.,2.5E-11,0.,0.6)`	Sander et al. (2003)
G3203	$NO_2 + HO_2 \rightarrow HNO_4$	`k_NO2_HO2`	Sander et al. (2003)
G3204	$NO_3 + HO_2 \rightarrow NO_2 + OH + O_2$	`3.5E-12`	Sander et al. (2003)
G3205	$HONO + OH \rightarrow NO_2 + H_2O$	`1.8E-11*EXP(-390./temp)`	Sander et al. (2003)
G3206	$HNO_3 + OH \rightarrow H_2O + NO_3$	`k_HNO3_OH`	Sander et al. (2003)*
G3207	$HNO_4 \rightarrow NO_2 + HO_2$	`k_NO2_HO2/ (2.1E-27*EXP(10900./ temp))`	Sander et al. (2003)*
G3208	$HNO_4 + OH \rightarrow NO_2 + H_2O$	`1.3E-12*EXP(380./temp)`	Sander et al. (2003)
G4101	$CH_4 + OH \rightarrow CH_3O_2 + H_2O$	`1.85E-20*EXP(2.82*log(temp) -987./temp)`	Atkinson (2003)*
G4102	$CH_3OH + OH \rightarrow HCHO + HO_2$	`7.3E-12*EXP(-620./temp)`	Sander et al. (2003)
G4103a	$CH_3O_2 + HO_2 \rightarrow CH_3OOH$	`4.1E-13*EXP(750./temp) /(1.+1./497.7*EXP(1160./ temp))`	Sander et al. (2003)*
G4103b	$CH_3O_2 + HO_2 \rightarrow HCHO + H_2O + O_2$	`4.1E-13*EXP(750./temp) /(1.+497.7*EXP(-1160./ temp))`	Sander et al. (2003)*
G4104	$CH_3O_2 + NO \rightarrow HCHO + NO_2 + HO_2$	`2.8E-12*EXP(300./temp)`	Sander et al. (2003)
G4105	$CH_3O_2 + NO_3 \rightarrow HCHO + HO_2 + NO_2$	`1.3E-12`	Atkinson et al. (1999)
G4106a	$CH_3O_2 + CH_3O_2 \rightarrow 2\ HCHO + 2\ HO_2$	`9.5E-14*EXP(390./temp) /(1.+1./26.2*EXP(1130./ temp))`	Sander et al. (2003)

Table C.1: Gas phase reactions (... continued)

#	reaction	rate coefficient	reference
G4106b	CH_3O_2 + CH_3O_2 → HCHO + CH_3OH	`9.5E-14*EXP(390./temp) /(1.+26.2*EXP(-1130./ temp))`	Sander et al. (2003)
G4107	CH_3OOH + OH → .7 CH_3O_2 + .3 HCHO + .3 OH + H_2O	`k_CH3OOH_OH`	Sander et al. (2003)*
G4108	HCHO + OH → CO + H_2O + HO_2	`9.52E-18*EXP(2.03*log(temp) +636./temp)`	Sivakumaran et al. (2003)
G4109	HCHO + NO_3 → HNO_3 + CO + HO_2	`3.4E-13*EXP(-1900./temp)`	Sander et al. (2003)*
G4110	CO + OH → H + CO_2	`1.57E-13 + cair*3.54E-33`	McCabe et al. (2001)
G4111	HCOOH + OH → HO_2	`4.E-13`	Sander et al. (2003)
G4500	ISOP + O_3 → .28 HCOOH + .65 MVK + .1 MVKO2 + .1 $CH_3C(O)OO$ + .14 CO + .58 HCHO + .09 H_2O_2 + .08 CH_3O_2 + .25 OH + .25 HO_2	`7.86E-15*EXP(-1913./temp)`	Pöschl et al. (2000)
G4501	ISOP + OH → ISO2	`2.54E-11*EXP(410./temp)`	Pöschl et al. (2000)
G4502	ISOP + NO_3 → ISON	`3.03E-12*EXP(-446./temp)`	Pöschl et al. (2000)
G4502	ISOP + HO_2 → ISOOH	`2.22E-13*EXP(-1300./temp)`	Pöschl et al. (2000)
G4504	ISO2 + NO → .88 NO_2 + .88 MVK + .88 HCHO + .88 HO_2 + .12 ISON	`2.22E-13*EXP(1300./temp)`	Boyd et al. (2003)
G4505	ISO2 + CH_3O_2 → .5 MVK + 1.25 HCHO + HO_2 + .25 CH_3COCHO +.25 CH_3COCH_2OH + .25 CH_3OH	`2.E-12`	von Kuhlmann (2001)
G4506	ISO2 + ISO2 → 2 MVK + HCHO + HO_2	`2.E-12`	Pöschl et al. (2000)
G4507	ISOOH + OH → MVK + + OH	`1E-10`	Pöschl et al. (2000)

Table C.1: Gas phase reactions (... continued)

#	reaction	rate coefficient	reference
G4507	ISON + OH → + CH_3COCH_2OH + NACA	`1.3E-11`	Pöschl et al. (2000)
G0101	Rn_01 → UNITY	`1.1574e-05`	see note
G0102	Rn_10 → UNITY	`1.1574e-06`	see note
G0103	Rn_100 → UNITY	`1.1574e-07`	see note

*Notes:

Rate coefficients for three-body reactions are defined via the function `k_3rd`(T, M, k_0^{300}, n, k_{inf}^{300}, m, f_{c}). In the code, the temperature T is called `temp` and the concentration of "air molecules" M is called `cair`. Using the auxiliary variables $k_0(T)$, $k_{\mathrm{inf}}(T)$, and k_{ratio}, `k_3rd` is defined as:

$$k_0(T) = k_0^{300} \times \left(\frac{300\mathrm{K}}{T}\right)^n \tag{C.1}$$

$$k_{\mathrm{inf}}(T) = k_{\mathrm{inf}}^{300} \times \left(\frac{300\mathrm{K}}{T}\right)^m \tag{C.2}$$

$$k_{\mathrm{ratio}} = \frac{k_0(T)M}{k_{\mathrm{inf}}(T)} \tag{C.3}$$

$$\texttt{k\_3rd} = \frac{k_0(T)M}{1+k_{\mathrm{ratio}}} \times f_{\mathrm{c}}^{\left(\frac{1}{1+(\log_{10}(k_{\mathrm{ratio}}))^2}\right)} \tag{C.4}$$

A similar function, called `k_3rd_iupac` here, is used by Atkinson et al. (2005) for three-body reactions. It has the same function parameters as `k_3rd` and it is defined as:

$$k_0(T) = k_0^{300} \times \left(\frac{300\mathrm{K}}{T}\right)^n \tag{C.5}$$

$$k_{\mathrm{inf}}(T) = k_{\mathrm{inf}}^{300} \times \left(\frac{300\mathrm{K}}{T}\right)^m \tag{C.6}$$

$$k_{\mathrm{ratio}} = \frac{k_0(T)M}{k_{\mathrm{inf}}(T)} \tag{C.7}$$

$$N = 0.75 - 1.27 \times \log_{10}(f_{\mathrm{c}}) \tag{C.8}$$

$$\texttt{k\_3rd\_iupac} = \frac{k_0(T)M}{1+k_{\mathrm{ratio}}} \times f_{\mathrm{c}}^{\left(\frac{1}{1+(\log_{10}(k_{\mathrm{ratio}})/N)^2}\right)} \tag{C.9}$$

G1002: path leading to 2 O(^{3}P) + O_2 neglected

G01Diag: `k_O3s = (1.7E-12*EXP(-940./temp)) * C(KPP_OH) + (1.E-14*EXP(-490./temp)) * C(KPP_HO2) + J_O1D * 2.2E-10 * C(KPP_H2O) / ( 3.2E-11*EXP(70./temp)*C(KPP_O2) + 1.8E-11*EXP(110./temp)*C(KPP_N2) + 2.2E-10*C(KPP_H2O) )`

G2108: branching ratio from Hack et al., see note B5 of Sander et al. (2003)

G2110: The rate coefficient is: `k_HO2_HO2 = (1.5E-12*EXP(19./temp) +1.7E-33*EXP(1000./temp)*cair)* (1.+1.4E-21*EXP(2200./temp)*C(KPP_H2O))`. The value for the first (pressure-independent) part is from Christensen et al. (2002), the water term from Kircher and Sander (1984)

G3109: The rate coefficient is: `k_NO3_NO2 = k_3rd(temp,cair,2.E-30,4.4,1.4E-12,0.7,0.6)`.

G3110: The rate coefficient is defined as backward reaction divided by equilibrium constant.

G3203: The rate coefficient is: `k_NO2_HO2 = k_3rd(temp,cair,1.8E-31,3.2,4.7E-12,1.4,0.6)`.

G3206: The rate coefficient is: `k_HNO3_OH = 2.4E-14 * EXP(460./temp) + 1./ ( 1./(6.5E-34 * EXP(1335./temp)*cair) + 1./(2.7E-17 * EXP(2199./temp)) )`

G3207: The rate coefficient is defined as backward reaction divided by equilibrium constant.

G4103: product distribution is from Elrod et al. (2001)

G4107: The rate coefficient is: `k_CH3OOH_OH = 3.8E-12*EXP(200./temp)`

G4109: same temperature dependence assumed as for CH_3CHO+NO_3

Table C.2: Photolysis reactions

#	reaction	rate coefficient	reference
J1001a	$O_3 + h\nu \rightarrow O(^1D)$	J_O1D	see note
J1001b	$O_3 + h\nu \rightarrow O(^3P)$	J_O3P	see note
J2101	$H_2O_2 + h\nu \rightarrow 2$ OH	J_H2O2	see note
J3101	$NO_2 + h\nu \rightarrow NO + O(^3P)$	J_NO2	see note
J3103a	$NO_3 + h\nu \rightarrow NO_2 + O(^3P)$	J_NO2O	see note
J3103b	$NO_3 + h\nu \rightarrow NO$	J_NOO2	see note
J3104	$N_2O_5 + h\nu \rightarrow NO_2 + NO_3$	J_N2O5	see note
J3200	$HONO + h\nu \rightarrow NO +$ OH	J_HONO	see note
J3201	$HNO_3 + h\nu \rightarrow NO_2 +$ OH	J_HNO3	see note

Table C.2: Photolysis reactions (... continued)

#	reaction	rate coefficient	reference
J3202	$HNO_4 + h\nu \rightarrow .667\ NO_2 + .667\ HO_2 + .333\ NO_3 + .333\ OH$	`J_HNO4`	see note
J4100	$CH_3OOH + h\nu \rightarrow HCHO + OH + HO_2$	`J_CH3OOH`	see note
J4101a	$HCHO + h\nu \rightarrow H_2 + CO$	`J_COH2`	see note
J4101b	$HCHO + h\nu \rightarrow H + CO + HO_2$	`J_CHOH`	see note

*Notes: J-values are calculated with an external module and then supplied to the MECCA chemistry

Bibliography

Adler, R., Kidd, C., Petty, G., Morissey, M., and Goodman, H. M.: Intercomparison of Global Precipitation Products: The Third Precipitation Intercomparison Project (PIP3), B. Am. Meteorol. Soc., p. 1377 1396, 2001.

Adler, R., Huffman, G., Chang, A., Ferraro, R., Xie, P., Janowiak, J., Rudolf, B., Schneider, U., Curtis, S., Bolvin, D., Gruber, A., Susskind, J., and Arkin, P.: The Version 2 Global Precipitation Climatology Project (GPCP) Monthly Precipitation Analysis (1979-Present), J. Hydrometeorol., 4, 1147–1167, 2003.

Allan, R., Ringer, M., and Slingo, A.: Evaluation of moisture in the Hadley Centre climate model using simulations of HIRS water-vapour channel radiances, Quat. J. Roy. Meteorol. Soc., 129, 3371–3389, 2003.

Altimir, N., Kolari, P., Tuovinen, J.-P., Vesala, T., Bck, J., Suni, T., Kulmala, M., and Hari, P.: Foliage surface ozone deposition: a role for surface moisture?, Biogeosciences, 3, 209–228, 2006.

Arpe, K., Hagemann, S., Jacob, D., and Roeckner, E.: The realism of the ECHAM5 models to simulate the hydrological cycle in the Arctic and North European area, Nordic Hydrology, 36, 349–367, 2005.

Atkinson, R.: Kinetics of the gas-phase reactions of OH radicals with alkanes and cycloalkanes, Atmos. Chem. Phys., 3, 2233–2307, 2003.

Atkinson, R., Baulch, D. L., Cox, R. A., Hampson, Jr., R. F., Kerr, J. A., Rossi, M. J., and Troe, J.: Summary of evaluated kinetic and photochemical data for atmospheric chemistry: Web version August 1999, `http://www.iupac-kinetic.ch.cam.ac.uk/`, 1999.

Atkinson, R., Baulch, D. L., Cox, R. A., Crowley, J. N., Hampson, Jr., R. F., Hynes, R. G., Jenkin, M. E., Kerr, J. A., Rossi, M. J., and Troe, J.: Summary of evaluated kinetic and photochemical data for atmospheric chemistry: Web version March 2005, `http://www.iupac-kinetic.ch.cam.ac.uk/`, 2005.

Baldocchi, D. D., Hicks, B. B., and Camara, P.: A canopy stomatal resistance model for gaseous deposition to vegetated surfaces, Atmos. Environ., 21, 91–101, 1987.

Barth, M., McFadden, J., Sun, J., Wiedinmyer, C., Chuang, P., Collins, D., Griffin, R., Hannigan, M., Karl, T., Kim, S., Lasher-Trapp, S., Levis, S., Litvak, M., Mahowald, N., Moore, K., Nandi, S., Nemitz, E., Nenes, A., Potosnak, M., Raymond, T., Smith, J., Stroud, C., and Still, C.: Coupling between land ecosystems and the atmospheric hydrologic cycle through biogenic aerosol pathways, B. Am. Meteorol. Soc., 86, 1738–1742, 2005.

Bastiaanssen, W.: Regionalization of surface flux densities and moisture indicators in composite terrain. A remote sensing approach under clear skies in Mediterranean climates, Phd thesis, Agricultural University of Wageningen, 273 pp, 1995.

Beljaars, A., Viterbo, P., Miller, M., and Betts, A.: The Anomalous Rainfall over the United States during July 1993: Sensitivity to Land Surface Parameterization and Soil Moisture Anomalies, Monthly Weather Review, 124, 362383, 1996.

Betts, A.: The land surface-atmosphere interaction: A review based on observational and global modeling perspectives, J. Geophys. Res., 101, 7209–7225, 1996.

Betts, A. K.: Understanding hydrometeorology using global models, B. Am. Meteorol. Soc., 85, 1673–1688, 2004.

Betts, A. K., Ball, J. H., Beljaars, A. C. M., Miller, M. J., and Viterbo, P. A.: The land surface-atmosphere interaction: A review based on observational and global modeling perspectives, J. Geophys. Res., 101, 72097225, 1996.

Bonan, G. B.: Forests and Climate Change: Forcings, Feedbacks, and the Climate Benefits of Forests, Science, 320, 1444–1449, 2008.

Bouwman, A. F., van der Hoek, K. W., and Olivier, J. G. J.: Uncertanties in the global source distribution of nitrous oxide, J. Geophys. Res., 100, 2785–2800, 1995.

Boyd, A. A., Flaud, P.-M., Daugey, N., and Lesclaux, R.: Rate constants for RO_2 + HO_2 reactions measured under a large excess of HO_2, J. Phys. Chem. A, 107, 818–821, 2003.

Brutsaert, W.: Evaporation into the Atmosphere, Kluwer Academic Pulishers, Boston, 299p, 1982.

Chahine, M.: The hydrological cycle and its influence on climate, Nature, 359, 373–380, 1992.

Chen, C., Roeckner, E., and Soden, B.: A comparison of satellite observations and model simulations of column-integrated moisture and upper-tropospheric humidity, J. Climate, 9, 1561–1585, 1996.

Christensen, L. E., Okumura, M., Sander, S. P., Salawitch, R. J., Toon, G. C., Sen, B., Blavier, J.-F., and Jucks, K. W.: Kinetics of $HO_2 + HO_2 \rightarrow H_2O_2 + O_2$: Implications for stratospheric H_2O_2, Geophys. Res. Lett., 29, doi:10.1029/2001GL014525, 2002.

Conrad, R.: Soil microorganisms as controllers of atmospheric trace gases (H-2, CO, CH_4, OCS, N_2O, and NO), Microbiological reviews, 60, 609–641, 1996.

Crutzen, P. J.: Overview of tropospheric chemistry: developments during the past quarter century and a look ahead, Faraday Discuss, 100, 1–20, 1995.

Crutzen, P. J. and Lawrence, M. G.: The impact of Precipitation Scavenging on the Transport of Trace Gases: a 3-Dimensional Model Sensitivity Study, J. Atmos. Chem., 37, 81–112, 2000.

Damian, V., Sandu, A., Damian, M., Potra, F., and Carmichael, G. R.: The kinetic preprocessor KPP - a software environment for solving chemical kinetics, Computers and Chemical Engineering, 26, 1567–1579, 2002.

Davidson, E. A. and Kingerlee, W.: A global inventory of nitric oxide emissions from soils, Nutrient cycling in agroecosystems, 48, 37–50, 1997.

Delworth, T. and Manabe, S.: The Influence of Soil Wetness on Near-Surface Atmospheric Variability, J. Climate, 2, 1447 1462, 1988.

Dirmeyer, P., Gao, X., Zhao, M., Guo, Z., Oki, T., and Hanasaki, N.: GSWP-2: Multimodel Analysis and Implications for Our Perception of the Land Surface, B. Am. Meteorol. Soc., 87, 1381–1397, 2006.

Dirmeyer, P. A.: Using a Global Soil Wetness Dataset to Improve Seasonal Climate Simulation, J. Climate, 13, 2900–2922, 2000.

Dirmeyer, P. A. and Shukla, J.: Albedo as a modulator of climate response to tropical deforestation, J. Geophys. Res., 99, 20 863–20 877, 1994.

Dirmeyer, P. A., Guo, Z., and Gao, X.: Validation and forecast applicability of multi-year global soil wetness products, 3, 1011–1033, 2004.

Dolman, A. and Gregory, D.: The parametrization of rainfall interception in GCMs, Quat. J. Roy. Meteorol. Soc., 118, 455–467, 1992.

Douville, H.: Influence of Soil Moisture on the Asian and African Monsoons. Part II: Interannual Variability, J. Climate, 15, 701720, 2002.

Douville, H.: Assessing the Influence of Soil Moisture on Seasonal Climate Variability with AGCMs, 4, 10441066, 2003.

Douville, H.: Relevance of soil moisture for seasonal atmospheric predictions: is it an initial value problem?, Clim. Dyn., 22, 429–446, 2004.

Douville, H., Conil, S., Tyteca, S., and Voldoire, A.: Soil moisture memory and West African monsoon predictability: artefact or reality?, Clim. Dyn., 28, 723–742, 2007.

Dümenil, L. and Todini, E.: Advances in Theoretical Hydrology, A Tribute to James Dooge, chap. A rainfall-runoff scheme for use in the Hamburg climate model, pp. 129–157, Elsevier, Amsterdam, 1992.

Durre, I., Vose, R. S., and Wuertz, D. B.: Overview of the Integrated Global Radiosonde Archive, J. Climate, 19, 53–68, 2006.

Eagleson, P. S.: Climate, soil, and vegetation. 1. Introduction to water balance dynamics, Water Res. Research, 14, 705–712, 1978.

Elrod, M. J., Ranschaert, D. L., and Schneider, N. J.: Direct kinetics study of the temperature dependence of the CH_2O branching channel for the CH_3O_2 + HO_2 reaction, Int. J. Chem. Kinetics, 33, 363–376, 2001.

Eltahir, E. A. B.: The role of vegetation in sustaining large-scale atmospheric circulations in the tropics, J. Geophys. Res., 101, 4255–4268, 1996.

Eltahir, E. A. B.: A Soil Moisture - Rainfall Feedback Mechanism,1. Theory and Observations, Water Res. Research, 34, 765–776, 1998.

Eltahir, E. A. B. and Bras, R. L.: A description of rainfall interception over large areas, J. Climate, 6, 1002–1008, 1993a.

Eltahir, E. A. B. and Bras, R. L.: Estimation of the Fractional Coverage of Rainfall in Climate Models, J. Climate, 6, 1002–1008, 1993b.

Engelen, R. and Stephens, G.: Characterization of water-vapor retrievals from TOVS/HIRS and SSM/T-2 measurements, Quat. J. Roy. Meteorol. Soc., 125, 331–351, 1999.

Entekhabi, D., Rodriguez-Iturbe, I., and Bras, R. L.: Variability in Large-Scale Water Balance with Land Surface-Atmosphere Interaction, J. Climate, 5, 798813, 1992.

Erisman, J. W. and Van Pul, A.: Parameterization of surface resistance for the quantification of atmospheric deposition of acidifying pollutants and ozone, Atmos. Environ., 28, 2595–2607, 1994.

Erisman, J. W., Pul, A. V., and Wyers, P.: Parameterization of surface-resistance for the quantification of atmospheric deposition of acidifying pollutants and ozone, Atmos. Environ., 28, 2595–2607, 1994.

Findell, K. L. and Eltahir, E. A. B.: An analysis of the soil moisture-rainfall feedback, based on direct observations from Illinois, Water Res. Research, 33, 725735, 2003.

Folkins, I., Kelly, K. K., and Weinstock, E. M.: A simple explanation for the increase in relative humidity between 11 and 14 km in the tropics, J. Geophys. Res., 107, 13051327, 2002.

Folkins, I., Bernath, P., Boone, C., Donner, L. J., Eldering, A., Lesins, G., Martin, R. V., Sinnhuber, B.-M., and Walker, K.: Testing convective parameterizations with tropical measurements of HNO3, CO, H2O, and O3: Implications for the water vapor budget, J. Geophys. Res., 111, 13051327, 2006.

Fuentes, J. D., Gillespie, T. J., Hartog, G. D., and Neumann, H. H.: Ozone deposition onto a deciduous forest during dry and wet conditions, Agric. For. Meteor., 62, 1–18, 1992.

Gaffen, D. and Barnett, T.: A comparison of observations and model simulations of tropospheric water vapor, J. Geophys. Res., 97, 2775–2780, 1992.

Gaffen, D., Rosen, R., Salstein, D., and Boyle, J.: Evaluation of tropospheric water vapor simulations from the atmospheric model intercomparison project, J. Climate, 10, 1648–1661, 1997.

Ganzeveld, L. and Lelieveld, J.: Dry deposition parameterization in a chemistry general circulation model and its influence on the distribution of reactive trace gases, J. Geophys. Res., 100, 20 99921 012, 1995.

Ganzeveld, L. and Lelieveld, J.: Impact of Amazonian deforestation on atmospheric chemistry, Geophys. Res. Lett., 31, 6105, doi:10.1029/2003GL019 205",, 2004.

Ganzeveld, L., Lelieveld, J., and Roelofs, G.: A dry deposition parameterization for sulfur oxides in a chemistry and general circulation model, J. Geophys. Res., 103, 5679–5694, 1998.

Ganzeveld, L., Lelieveld, J., Dentener, F. J., Krol, M. C., Bouwman, A. J., and Roelofs, G. J.: Global soil-biogenic NOx emissions and the role of canopy processes, J. Geophys. Res., 107, 0148–0227, 2002a.

Ganzeveld, L. N., Lelieveld, J., Dentener, F. J., Krol, M. C., and Roelofs, G. J.: Atmosphere-biosphere trace gas exchanges simulated with a single-column mode, J. Geophys. Res., 107, 4297, 2002b.

Gash, J. H. C.: Analytical model of rainfall interception by forests, Quat. J. Roy. Meteorol. Soc., 105, 43–55, 1979.

Gash, J. H. C., Lloyd, C. R., and Lachaud, G.: Estimating sparse forest rainfall interception with an analytical model, J. Hydrology, 170, 79–86, 1995.

Giorgi, F.: Analysis of the surface hydrology in a regional climate model, Quat. J. Roy. Meteorol. Soc., 120, 161–183, 1994.

Grantz, D.: Effects of stomatal conductance and surface wetness on ozone deposition in field-grown, Atmos. Environ., 29, 3189–3198, 1995.

Guenther, A., Hewitt, C. N., Erickson, D., Fall, R., Geron, C., Graedel, T., Harley, P., Klinger, L., Lerdau, M., McKay, W. A., Pierce, T., Scholes, B., Steinbrecher, R., Tallamraju, R., Taylor, J., and Zimmerman, P.: A global model of natural volatile organic compound emissions, J. Geophys. Res., 100, 8873–8892, 1995.

Guenther, A., Karl, T., Harley, P., Wiedinmyer, C., Palmer, P., and Geron, C.: Estimates of global terrestrial isoprene emissions using MEGAN (Model of Emissions of Gases and Aerosols from Nature), Atmos. Chem. Phys., 6, 107–173, 2006.

Guo, Z. and Dirmeyer, P. A.: Evaluation of the Second Global Soil Wetness Project soil moisture simulations: 1. Intermodel comparison, J. Geophys. Res., 111, doi:10.1029/2006JD007 233, 2006.

Gut, A. and et al.: Exchange fluxes of NO, NO2, and O3 at soil and leaf surfaces in an Amazonian rain forest, J. Geophys. Res., 107, doi:1029/2001JD000 654, 2002.

Hagemann, S.: An improved land surface parameter dataset for global and regional climate models, Technical report, Max Planck Institute for Meteorology, 2002.

Hagemann, S. and Dümenil Gates, L.: Improving a subgrid runoff parameterizations scheme for climate models by the use of high resolution data derived from satellite observations, Clim. Dyn., 21, 349–359, 2003.

Hagemann, S., Arpe, K., and E. Roeckner, .: Evaluation of the hydrological cycle in the ECHAM5 model, J. Climate, 19, 3810–3827, 2006.

Hahmann, A. N.: Representing Spatial Subgrid-Scale Precipitation Variability in a GCM, 4, 891900, 2003.

Held, I. and Soden, B.: Water vapor feedback and global warming, Annual review of energy and the environment, 25, 441–475, 2000.

Henderson-Sellers, A., Yang, Z., and Dickinson, R.: The Project for Intercomparison of Land-Surface Parameterization Schemes, B. Am. Meteorol. Soc., 74, 1335–1349, 1993.

Hormann, G., Branding, A., Clemen, T., Herbst, M., Hinrichs, A., and Thamm, F.: Calculation and simulation of wind controlled canopy interception of a beech forest in Northern Germany, Agricultural and Forest Meteorology, 79, 131–148(18), 1996.

Huntington, T.: Evidence for intensification of the global water cycle: Review and synthesis, J. Hydrology, 319, 83–95, 2006.

Iacono, M., Delamere, J., Mlawer, E., and Clough, S.: Evaluation of upper tropospheric water vapor in the NCAR Community Climate Model (CCM3) using modeled and observed HIRS radiances, J. Geophys. Res., 108, 5548–5581, 2003.

IPCC: Climate Change 2007: the Scientific Basis. Contribution of Working Group I to the Fourth Assessment Report of the IPCC, 2007a.

IPCC: Climate Change 2007: Impacts, Adaptation and Vulnerability. Contribution of Working Group II to the Fourth Assessment Report of the IPCC, 2007b.

Jacobson, M. Z.: Effects of Soil Moisture on Temperatures, Winds, and Pollutant Concentrations in Los Angeles, J. Appl. Meteor., 38, 607616, 1999.

Jöckel, P.: Technical note: Recursive rediscretisation of geo-scientific data in the Modular Earth Submodel System (MESSy), Atmos. Chem. Phys., 6, 3557–3562, 2006.

Jöckel, P., Sander, R., Kerkweg, A., Tost, H., and Lelieveld, J.: Technical Note: The Modular Earth Submodel System (MESSy) – a new approach towards Earth System Modeling, Atmos. Chem. Phys., 5, 433–444, 2005.

Jöckel, P., Tost, H., Pozzer, A., Brühl, C., Bucholz, J., L., G., Hoor, P., Kerkweg, A., Lawrence, M., Sander, R., Steil, B., Stiller, G., Tanarhte, M., Taraborrelli, D., van Aardenne, J., and Lelieveld, J.: Evaluation of the atmospheric chemistry GCM ECHAM5/MESSy: Consistent simulation of ozone in the stratosphere and troposphere, Atmos. Chem. Phys., 6, 5067–5104, 2006.

John, V. and Buehler, S.: Comparison of microwave satellite humidity data and radiosonde profiles: a survey of European stations, Atmos. Chem. Phys. Discuss., 5, 1529–1550, URL `http://www.atmos-chem-phys-discuss.net/5/1529/2005/`, 2005.

Kim, Y. J. and Wang, G. L.: Impact of initial soil moisture anomalies on subsequent precipitation over North America in the coupled land-atmosphere model CAM3-CLM3, 8, 513–533, 2007.

Kircher, C. C. and Sander, S. P.: Kinetics and mechanism of HO_2 and DO_2 disproportionations, J. Phys. Chem., 88, 2082–2091, 1984.

Koster, R. and Milly, P.: The Interplay between Transpiration and Runoff Formulations in Land Surface Schemes Used with Atmospheric Models, J. Climate, 10, 15781591, 1997.

Koster, R. D., Dirmeyer, P. A., Guo, Z., Bonan, G., Chan, E., Cox, P., Gordon, C. T., Kanae, S., Kowalczyk, E., Lawrence, D., Liu, P., Lu, C., Malyshev, S., McAvaney, B., Mitchell, K., Mocko, D., Oki, T., Oleson, K., Pitman, A., Sud, Y. C., Taylor, C. M., Verseghy, D., Vasic, R., Xue, Y., and Yamada, T.: Regions of Strong Coupling Between Soil Moisture and Precipitation, Science, 305, 1138–1140, 2004.

Landgraf, J. and Crutzen, P. J.: An Efficient Method for Online Calculations of Photolysis and Heating Rates, J. Atmos. Chem., 25, 863–878, 1998.

Lang, R. and Lawrence, M.: Evaluation of the hydrological cycle of MATCH driven by NCEP reanalysis data: Comparison with GOME water vapor field measurements,, Atmos. Chem. Phys., 5, 887–908, 2005a.

Lang, R. and Lawrence, M.: Improvement of the vertical humidity distribution in the chemistry-transport model MATCH through increased evaporation of convective precipitation, Geophys. Res. Lett., 32, doi:10.1029/2005GL023172, 2005b.

Lang, R., Williams, J. E., van der Zande, W. J., and Maurellis, A. N.: Application of the spectral structure parameterization technique: Retrieval of total water vapour columns from GOME, Atmos. Chem. Phys., 3, 145–160, 2003.

Lang, R., Casadio, S., Maurellis, A. N., and Lawrence, M. G.: Evaluation of the GOME Water Vapor Climatology 19952002, J. Geophys. Res., 112, doi:10.1029/2006JD008246, 2007.

Lau, W.-M., Sud, Y., and Kim, J.: Intercomparison of hydrologic processes in global climate models, Tech. Memo 104617, NASA, 1995.

Laurent, B., Marticorena, B., Bergametti, G., Lon, J., and Mahowald, N.: Modeling mineral dust emissions from the Sahara desert using new surface and soil developments, J. Geophys. Res., 113, D14 218, doi:1.0.1029/2007JD009484, 2008.

Lawrence, M. and Rasch, P.: Tracer transport in deep convective updrafts: plume ensemble versus bulk formulations, J. Atmos. Sci., 62, 2880–2894, 2005.

Lean, J. and Warrilow, D. A.: Simulation of the regional climatic impact of Amazon deforestation, Nature, 342, 411–413, 1989.

Levy, H.: Normal Atmosphere: Large radical and formaldehyde concentrations predicted, Science, 173, 141–143, 1971.

Li, H., Robock, A., and Wild, M.: Evaluation of Intergovernmental Panel on Climate Change Fourth Assessment soil moisture simulations for the secons half of the twentieth century, J. Geophys. Res., 112, 2007.

Lin, S. J. and Rood, R. B.: Multidimensional flux form semi-Lagrangian transport., Monthly Weather Review, 124, 2046–2068, 1996.

Lohmann, U. and Roeckner, E.: Design and performance of a new cloud microphysics scheme developed for the ECHAM general circulation model, Clim. Dyn., 12, 557–572, 1996.

Mahfouf, J. F.: Analysis of Soil Moisture from Near-Surface Parameters: A Feasibility Study, J. Appl. Meteor., 30, 15341547, 1991.

Marengo, J.: Characteristics and spatio-temporal variability of the Amazon River Basin Water Budget, Clim. Dyn., 24, 11–22, 2005.

McCabe, D. C., Gierczak, T., Talukdar, R. K., and Ravishankara, A. R.: Kinetics of the reaction OH + CO under atmospheric conditions, Geophys. Res. Lett., 28, 3135–3138, 2001.

Miloshevich, L.M., A. P. H. V. and Oltmans, S.: Development and Validation of a Time-Lag Correction for Vaisala Radiosonde Humidity Measurements, J. Atmos. Oceanic Technol., 21, 13051327, 2004.

Monson, R. K. and Holland, E. A.: Biospheric trace gas fluxes and their control over tropospheric chemistry, Annual Review Of ecology and systematics, 32, 547–572, 2001.

Müller, J.-F., Stavrakou, T., Wallens, S., De Smedt, I., Van Roozendael, M., Potosnak, M. J., Rinne, J., Munger, B., Goldstein, A., and Guenther, A. B.: Global isoprene emissions estimated using MEGAN, ECMWF analyses and a detailed canopy environment model, Atmos. Chem. Phys., 8, 1329–1341, 2008.

Namias, J.: Factors in the initiation, perpetuation and termination of drought, Int. Assoc. Sci. Hydrol. Publ., 51, 81–94, 1960.

Noel, S., Buchwitz, M., Bovensmann, H., Hoogen, R., and Burrows, J. P.: Atmospheric Water Vapor Amounts Retrieved from GOME Satellite Data, Geophys. Res. Lett., 26, 1841–1844, 1999.

Nordeng, T. E.: Extended versions of the convective parametrization scheme at ECMWF and their impact on the mean and transient activity of the model in the tropics, Tech. Rep. 206, ECWMF, 1994.

Oki, T.: Global Energy and Water Cycles, vol. The global water cycle, Cambridge Univ. Press, New York, 1999.

Oki, T. and Kanae, S.: Global hydrological cycles and world water resources, Science, 313, 1068–1072, 2006.

Olson, J.: World ecosystems (WE1.4): Digital raster data on a 10 min geographic 1080x2160 grid square, Global Ecosystem Database, Version 1.0: DISC A, edited by NOAA National Geophysical Data Center, 1992.

Onof, C. and Wheater, H. S.: Analysis of the spatial coverage of British rainfall fields, J. Hydrology, 176, 97–113, 1996.

Parton, W. J., Holland, E. A., del Grosso, S. J., Hartman, M. D., Martin, R. E., Mosier, A. R., Ojima, D. S., and Schimel, D. S.: Generalized model for NO_x and N_2O emissions from soils, J. Geophys. Res., 106, 17 403–17 419, 2001.

Peixoto, J. and Oort, A.: Physics of climate, Springer, ISBN 0883187124, 1992.

Pierce, D., Barnett, T., Fetzer, E., and Gleckler, P.: Three-dimensional tropospheric water vapor in coupled climate models compared with observations from the AIRS satellite system, Geophys. Res. Lett., 33, doi:10.1029/2006GL027060, 2006.

Pilegaard, K.: Factors controlling regional differences in forest soil emission of nitrogen oxides (NO and N_2O), Biogeosciences, 3, 651–661, 2006.

Pitman, A.: Sensitivity of regional climates to localized precipitation in global models, Nature, 346, 734–737, 1990.

Pitman, A. J.: The evolution of, and revolution in, land surface schemes designed for climate models, Int. J. of Climatology, 23, 479–510, 2003.

Porporato, A., D'Odorico, P., Laio, F., and Rodriguez-Iturbe, I.: Hydrologic controls on soil carbon and nitrogen cycles. I. Modeling scheme, Adv. Water Res., 26, 45–58, 2003a.

Pöschl, U., von Kuhlmann, R., Poisson, N., and Crutzen, P. J.: Development and intercomparison of condensed isoprene oxidation mechanisms for global atmospheric modeling, J. Atmos. Chem., 37, 29–52, 2000.

Potter, C. S., Matson, P. A., Vitousek, P. M., and Davidson, E. A.: Process modeling of controls on nitrogen trace gas emissions from soils worldwide, J. Geophys. Res., 101, 1361–1377, 1996.

Randel, D. L., Greenwald, T. J., Vonder Haar, T. H., Stephens, G. L., Ringerud, M. A., and Combs, C. L.: A New Global Water Vapor Dataset, B. Am. Meteorol. Soc., 77, 1233–1254, 1996.

Raval, A. and Ramanathan, V.: Observational determination of the greenhouse effect, Nature, 342, 758–761, 1989.

Robock, A., Schlosser, C., Vinnikov, K., Speranskaya, N., and Entin, J.: Evaluation of AMIP soil moisture simulations, Global and Planetary Change, 19, 181–208, 1998.

Rodell, M., Houser, P., Berg, A., , and Famiglietti, J.: Evaluation of 10 Methods for Initializing a Land Surface Model, 6, 146155, 2005.

Rodriguez-Iturbe, I. and Eagleson, P.: Mathematical models in rainstorm events in space and time, Water Resources Research, 23, 181–190, 1987.

Roeckner, E., Bäuml, G., Bonaventura, L., Brokopf, R., Esch, M., Giorgetta, M., Hagemann, S., Kirchner, I., Kornblueh, L., Manzini, E., Rhodin, A., Schlese, U., Schulzweida, U., and Tompkins, A.: The atmospheric general circulation model ECHAM5. PART I: Model description, Technical report, Max Planck Institute for Meteorology, 2003.

Roeckner, E., Brokopf, R., Esch, M., Giorgetta, M., Hagemann, S., Kornblueh, L., Manzini, E., Schlese, U., and Schulzweida, U.: Sensitivity of simulated climate to horizontal and vertical resolution in the ECHAM5 atmosphere model, J. Climate, 19, 3771–3791, 2006.

Rosen, R. D.: The global energy cycle, vol. Global Energy and Water Cycles, Cambridge University Press, 1999.

Rowntree, P. R. and Bolton, J. A.: Simulation of the atmospheric response to soil moisture anomalies over Europe, Quat. J. Roy. Meteorol. Soc., 109, 501–526, 1983.

Rutter, A. J., Kershaw, K. A., Robins, P. C., and Morton, A. J.: A predictive model of rainfall interception in forests I. Derivation of the model from observations in a plantation of Corsican pine, Agricultural Meteorology, 9, 367384, 1971.

Sander, R., Jöckel, P., Kerkweg, A., and Lelieveld, J.: Technical Note: The new comprehensive atmospheric chemistry module MECCA, Atmos. Chem. Phys., 5, 445–450, 2005.

Sander, S. P., Finlayson-Pitts, B. J., Friedl, R. R., Golden, D. M., Huie, R. E., Kolb, C. E., Kurylo, M. J., Molina, M. J., Moortgat, G. K., Orkin, V. L., and Ravishankara, A. R.: Chemical Kinetics and Photochemical Data for Use in Atmospheric Studies, Evaluation Number 14, JPL Publication 02-25, Jet Propulsion Laboratory, Pasadena, CA, 2003.

Sandu, A. and Sander, R.: Technical Note: Simulating chemical systems in Fortran90 and Matlab with the kinetic preprocessor KPP-2.1, Atmos. Chem. Phys., 6, 187–195, 2006.

Schär, C., D. Lüthi, U. B., and Heise, E.: The Soil-Precipitation Feedback: A Process Study with a Regional Climate Model, J. Climate, 12, 722–741, 1999.

Schmitt, A. and Brunner, B.: Emissions from aviation and their development over time, in: Pollutants from air traffic - results of atmospheric research 1992-1997. Final Report on the BMBF Verbundprogramm "Schadstoffe in der Luftfahrt", Tech. report, DLR-Mitteilung 97-04, 1-301, 1997.

Scholes, M., Matrai, P., Andreae, M., Smith, K., and Manning, M.: Atmospheric Chemistry in a Changing World. An Integration and Synthesis of a Decade of Tropospheric Chemistry Research, chap. Biosphere-Atmosphere Interactions, pp. 19–71, Springer-Verlag, 2003.

Seinfeld, J. H.: Reactive Hydrocarbons in the Atmosphere, chap. Global Atmospheric Chemistry of Reactive Hydrocarbons, pp. 293–319, Academic Press, San Diego, 1999.

Sellers, P., Mintz, Y., Sud, Y. C., and Dalcher, A.: A simple biopshere model (SiB) for use within general circulation models, J. Atmos. Sci., 43, 505–531, 1986.

Sellers, P. J., Dickinson, R. E., Randall, D. A., Betts, A. K., Hall, F. G., Berry, J. A., Collatz, G. J., Denning, A. S., Mooney, H. A., Nobre, C. A., Sato, N., Field, C. B., and Henderson-Sellers, A.: Modeling the Exchanges of Energy, Water, and Carbon Between Continents and the Atmosphere, Science, 275, 502–509, 1997.

Seneviratne, S. I., Lüthi, D., Litschi, M., and Schär, C.: Land-atmosphere coupling and climate change in Europe, Nature, 443, 205209, 2006.

Shao, Y. and Henderson-Sellers, A.: Modeling soil moisture : a project for intercomparison of land surface parameterization schemes Phase 2(b), J. Geophys. Res., 101, 7227–7250, 1996.

Shukla, J. and Mintz, Y.: Influence of Land-Surface Evapotranspiration on the Earth's Climate, Science, 215, 1498–1501, 1982.

Shuttleworth, W.: Evaporation from amazonian rainforest, Proceedings of the Royal Society B: Biological Sciences, 233, 321–346, 1988.

Shuttleworth, W. J. and Dickinson, R. E.: Comments on "Modelling tropical deforestation: A study of land surface parameterisations" by R. E. Dickinson and A. Henderson-Sellers, Quat. J. Roy. Meteorol. Soc., 115, 11771179, 1989.

Sivakumaran, V., Hölscher, D., Dillon, T. J., and Crowley, J. N.: Reaction between OH and HCHO: temperature dependent rate coefficients (202-399 K) and product pathways (298 K), Phys. Chem. Chem. Phys., 5, 4821–4827, 2003.

Soden, B. and Bretherton, F.: Evaluation of water vapor districution in general circulation models using satellite observations, J. Geophys. Res., 99, 1187–1210, 1994.

Steil, B., Dameris, M., Brühl, C., Crutzen, P. J., Grewe, V., Ponater, M., and Sausen, R.: Development of a chemistry module for GCMs: First results of a multiannual integration, Ann. Geophys., 16, 205–228, 1998.

Stocker, T.: Greenhouse gases during the last glacial and the deglaciation, Nova acta Leopoldina, pp. 79–88, 2001.

Sudradjat, A., Ferraro, R., and Fiorino, M.: A Comparison of Total Precipitable Water between Reanalyses and NVAP, J. Climate, 18, 1790–1807, 2005.

Taha, H.: Modeling impacts of increased urban vegetation on ozone air quality in the South Coast Air Basin, Atmos. Environ., 30, 34233430, 1996.

Taha, H.: Modeling the Impacts of Large-Scale Albedo Changes on Ozone Air Quality in the South Coast Air Basin, Atmos. Environ., 31, 1667–1676, 1997.

Tanre, D., Geleyn, J.-F., and Slingo, J. M.: First results of the introduction of an advanced aerosol-radiation interaction in the ECMWF low resolution global model, in: Aerosols and their climatic e effects, edited by Gerber, H. and Deepak, A., pp. 133–177, A. Deepak and V: A. Hampton, 1984.

Taylor, K. E.: Summarizing multiple aspects of model preformance in a single diagram, J. Geophys. Res., 106, 71837192, 2001.

Tiedtke, M.: A Comprehensive Mass Flux Scheme for Cumulus Parametrization in Large-Scale Models, Monthly Weather Review, 117, 1779–1800, 1989.

Tompkins, A. M.: A prognostic parameterization for the subgrid-scale variability of water vapor and clouds in large-scale models and its use to diagnose cloud cover, J. Atmos. Sci., 59, 1917–1942, 2002.

Tost, H.: Global Modelling of Cloud, Convection and Precipitation Influences on Trace Gases and Aerosols, Ph.D. thesis, Rheinische Friedrich-Wilhelms-University, Bonn/Germany, 2006.

Tost, H., Jöckel, P., Kerkweg, A., Sander, R., and Lelieveld, J.: Technical note: A new comprehensive SCAVenging submodel for global atmospheric chemistry modelling, Atmos. Chem. Phys., 6, 565–574, 2006a.

Tost, H., Jöckel, P., and Lelieveld, J.: Influence of different convection parameterisations in a GCM, Atmos. Chem. Phys., 6, 5475–5493, 2006b.

Trenberth, K.: Atmospheric moisture recycling: Role of advection and local evaporation, J. Climate, 12, 1368–1381, 1999.

Trenberth, K. and Guillemot, C.: Evaluation of the atmospheric moisture and hydrological cycle in the NCEP/NCAR reanalyses, Clim. Dyn., 14, 213–231, 1998.

Trenberth, K., Smith, L., Qian, T., Dai, A., and Fasullo, J.: Estimates of the global water budget and its annual cycle using observational and model data, J. Hydrometeorol., in press, 2007.

Vidale, P. L., Lüthi, D., Wegmann, R., and Schär, C.: European summer climate variability in a heterogeneous multi-model ensemble., Climatic Change, 81, 209232, 2007.

von Glasow, R., Sander, R., Bott, A., and Crutzen, P. J.: Modeling halogen chemistry in the marine boundary layer 2. Interactions with sulfur and the cloud-covered MBL, J. Geophys. Res., 107, 4324, doi:10.1029/2001JD000 943, 2002.

von Kuhlmann, R.: Tropospheric photochemistry of ozone, its precursors and the hydroxyl radical: A 3D-modeling study considering non-methane hydrocarbons, Ph.D. thesis, Johannes Gutenberg-Universität, Mainz, Germany, 2001.

von Kuhlmann, R., Lawrence, M. G., Crutzen, P. J., and Rasch, P. J.: A model for studies of tropospheric ozone and nonmethane hydrocarbons: Model description and ozone results, J. Geophys. Res., 108, 4294, doi:10.1029/2002JD002 893, 2003.

Wagner, T., Beirle, S., Grzegorski, M., and Platt, U.: Global trends (1996-2003) of total column precipitable water observed by Global Ozone Monitoring Experiment (GOME) on ERS-2 and their relation to near-surface temperature,, J. Geophys. Res., 111, 2006.

Waliser, D., Seo, K.-W., Schubert, S., and Njoku, E.: Global water cycle agreement in the climate models assessed in the IPCC AR4, Geophys. Res. Lett., 34, 2007.

Wang, D. G.: Impact of sub-grid variability of precipitation and canopy water storage on land and atmospheric hydrological processes, Phd thesis, University of Connecticut, 2007.

Wang, D. G., Wang, G. L., and Anagnostou, E. N.: Use of satellite-based precipitation observation in improving the parameterization of canopy hydrological processes in land surface models, J. Hydrometeorol., 6, 745–763, 2005.

Wang, G. and Eltahir, E. A. B.: Modeling the biosphere-atmosphere system: The impact of the subgrid variability in rainfall interception, J. Climate, 13, 2887–2899, 2000.

Weare, B. C. and Mokhov, I. I.: Evaluation of Total Cloudiness and Its Variability in the Atmospheric Model Intercomparison Project., J. Climate, 8, 2224–2238, 1995.

Wesely, M. L. and Hicks, B.: A review of the current status of knowledge on dry deposition, Atmos. Environ., 34, 2261–2282, 2000a.

Wesely, M. L. and Hicks, B. B.: A review of the current status of knowledge on dry deposition, Atmos. Environ., 34, 2261–2282, 2000b.

Wesely, M. L., Song, J., Mcmillen, R. T., and Meyers, T. P.: Effects of Soil Moisture Variations on Deposition Velocities Above Vegetation, Water, Air, & Soil Pollution: Focus, 1, 5–15, 2001.

Wild, M. and Roeckner, E.: Radiative fluxes in the ECHAM5 general circulation model, J. Climate, 19, 3792–3809, 2006.

Xie, P. and Arkin, P.: Global precipitation: a 17-year monthly analysis based on gauge observations, satellite estimates, and numerical model outputs, B. Am. Meteorol. Soc., 78, 2539–2558, 1997.

Yeh, T.-C., Wetherald, R. T., and Manabe, S.: The effect of soil moisture on the short-term climate and hydrology changeA numerical experiment, Monthly Weather Review, 112, 474490, 1984.

Yienger, J. and Levy, H.: Empirical-model of global soil NO_x emissions, J. Geophys. Res., 100, 11 447–11 464, 1995.

Yin, X., Gruber, A., and Arkin, P.: Comparison of the GPCP and CMAP Merged Gauge-Satellite Monthly Precipitation Products for the Period 19792001, J. Hydrometeorol., 5, 1207–1222, 2004.

Yin, X., Gruber, A., and Arkin, P.: Comparison of the GPCP and CMAP merged gauge-satellite monthly precipitation products for the period 1979-2001, J. Hydrometeorol., 5, 1207–1222, 2005.